Final Report

FDOT Contract No.: BED31- 977-27
UF Contract No.:

Drilled Shaft Imaging With 2D Ultrasonic Waveform Tomography

Principal Investigator:
Khiem Tran, Ph.D.

Researcher:
Bingkun Yang

Department of Civil and Coastal Engineering
Engineering School of Sustainable Infrastructure and Environment
University of Florida
P.O. Box 116580
Gainesville, Florida 32611-6580

Developed for the

FDOT

Kelly Shishlova, P.E., Project Manager

August 2026

DISCLAIMER

The opinions, findings, and conclusions expressed in this publication are those of the authors and not necessarily those of the Florida Department of Transportation or the U.S. Department of Transportation.

Prepared in cooperation with the State of Florida Department of Transportation and the U.S. Department of Transportation.

SI (MODERN METRIC) CONVERSION FACTORS (from FHWA)

APPROXIMATE CONVERSIONS TO SI UNITS

SYMBOL	WHEN YOU KNOW	MULTIPLY BY	TO FIND	SYMBOL
		LENGTH		
in	inches	25.4	millimeters	mm
ft	feet	0.305	meters	m
yd	yards	0.914	meters	m
mi	miles	1.61	kilometers	km

SYMBOL	WHEN YOU KNOW	MULTIPLY BY	TO FIND	SYMBOL
		AREA		
in^2	square inches	645.2	square millimeters	mm^2
ft^2	square feet	0.093	square meters	m^2
yd^2	square yard	0.836	square meters	m^2
ac	acres	0.405	hectares	ha
mi^2	square miles	2.59	square kilometers	km^2

SYMBOL	WHEN YOU KNOW	MULTIPLY BY	TO FIND	SYMBOL
		VOLUME		
fl oz	fluid ounces	29.57	milliliters	mL
gal	gallons	3.785	liters	L
ft^3	cubic feet	0.028	cubic meters	m^3
yd^3	cubic yards	0.765	cubic meters	m^3
NOTE: volumes greater than 1000 L shall be shown in m^3				

SYMBOL	WHEN YOU KNOW	MULTIPLY BY	TO FIND	SYMBOL
		MASS		
oz	ounces	28.35	grams	g
lb	pounds	0.454	kilograms	kg
T	short tons (2000 lb)	0.907	megagrams (or "metric ton")	Mg (or "t")

SYMBOL	WHEN YOU KNOW	MULTIPLY BY	TO FIND	SYMBOL
		TEMPERATURE (exact degrees)		
°F	Fahrenheit	5 (F-32)/9 or (F-32)/1.8	Celsius	°C

SYMBOL	WHEN YOU KNOW	MULTIPLY BY	TO FIND	SYMBOL
		ILLUMINATION		
fc	foot-candles	10.76	lux	lx
fl	foot-Lamberts	3.426	candela/m^2	cd/m^2

SYMBOL	WHEN YOU KNOW	MULTIPLY BY	TO FIND	SYMBOL
		FORCE and PRESSURE or STRESS		
Lbf*	poundforce	4.45	newtons	N
kip	kip force	1000	pounds	lbf
lbf/in^2	poundforce per square inch	6.89	kilopascals	kPa

APPROXIMATE CONVERSIONS TO SI UNITS

SYMBOL	WHEN YOU KNOW	MULTIPLY BY	TO FIND	SYMBOL
LENGTH				
mm	millimeters	0.039	inches	in
m	meters	3.28	feet	ft
m	meters	1.09	yards	yd
km	kilometers	0.621	miles	mi

SYMBOL	WHEN YOU KNOW	MULTIPLY BY	TO FIND	SYMBOL
AREA				
mm^2	square millimeters	0.0016	square inches	in^2
m^2	square meters	10.764	square feet	ft^2
m^2	square meters	1.195	square yards	yd^2
ha	hectares	2.47	acres	ac
km^2	square kilometers	0.386	square miles	mi^2

SYMBOL	WHEN YOU KNOW	MULTIPLY BY	TO FIND	SYMBOL
VOLUME				
mL	milliliters	0.034	fluid ounces	fl oz
L	liters	0.264	gallons	gal
m^3	cubic meters	35.314	cubic feet	ft^3
m^3	cubic meters	1.307	cubic yards	yd^3

SYMBOL	WHEN YOU KNOW	MULTIPLY BY	TO FIND	SYMBOL
MASS				
g	grams	0.035	ounces	oz
kg	kilograms	2.202	pounds	lb
Mg (or "t")	megagrams (or "metric ton")	1.103	short tons (2000 lb)	T

SYMBOL	WHEN YOU KNOW	MULTIPLY BY	TO FIND	SYMBOL
TEMPERATURE (exact degrees)				
°C	Celsius	1.8C+32	Fahrenheit	°F

SYMBOL	WHEN YOU KNOW	MULTIPLY BY	TO FIND	SYMBOL
ILLUMINATION				
lx	lux	0.0929	foot-candles	fc
cd/m^2	candela/m^2	0.2919	foot-Lamberts	fl

SYMBOL	WHEN YOU KNOW	MULTIPLY BY	TO FIND	SYMBOL
FORCE and PRESSURE or STRESS				
N	newtons	0.225	poundforce	lbf
kPa	kilopascals	0.145	poundforce per square inch	lbf/in^2

*SI is the symbol for International System of Units. Appropriate rounding should be made to comply with Section 4 of ASTM E380.
(Revised March 2003)

TECHNICAL REPORT DOCUMENTATION PAGE

1. Report No.	2. Government Accession No.	3. Recipient's Catalog No.
4. Title and Subtitle Drilled Shaft Imaging With 2D Ultrasonic Waveform Tomography		5. Report Date August 2026 6. Performing Organization Code
7. Authors Khiem Tran and Bingkun Yang		8. Performing Organization Report No.
9. Performing Organization Name and Address University of Florida – Dept. of Civil and Coastal Engineering Engineering School of Sustainable Infrastructure and Environment 365 Weil Hall – P.O. Box 116580 Gainesville, FL 32611-6580		10. Work Unit No. (TRAIS) 11. Contract or Grant No. BED31- 977-27
12. Sponsoring Agency Name and Address Florida Department of Transportation 605 Suwannee Street, MS 30 Tallahassee, FL 32399		13. Type of Report and Period Covered Final Report 03/01/2024 – 08/31/2026 14. Sponsoring Agency Code
15. Supplementary Notes		

16. Abstract

Drilled shafts are widely used as deep foundations for transportation infrastructure; however, construction defects such as soil intrusion, concrete segregation, slurry inclusions, necking, and soft-bottom conditions can compromise structural integrity and long-term performance. Conventional crosshole sonic logging (CSL) provides valuable quality-control information but offers limited capability for imaging shaft geometry and defect extent. This study developed, optimized, and field-validated a two-dimensional ultrasonic full waveform Inversion (UFWI) framework for high-resolution drilled shaft imaging using CSL waveform data. The method combines acoustic wavefield modeling, adjoint-state inversion, and regularized model updating to reconstruct cross-sectional P-wave velocity distributions without prior knowledge of shaft boundaries or defect locations. Synthetic studies demonstrated that UFWI can accurately image shaft geometry and detect internal and boundary defects. Parametric analyses further showed that at least five CSL access tubes are required for reliable imaging, while approximately one tube per foot of shaft diameter is recommended for shafts 6 ft in diameter or larger.

Field validation was conducted on a full-scale 6-ft-diameter, 40-ft-long drilled shaft constructed at the Florida Department of Transportation (FDOT) Hawthorne test facility with intentionally embedded defects, including concrete segregation, necking with soil intrusion, slurry inclusions, and a soft-bottom condition. UFWI successfully reconstructed shaft boundaries; identified major defect horizons; and localized anomalies consistent with documented as-built conditions. Compared with conventional CSL, UFWI provided higher spatial resolution and more detailed characterization of defect geometry, demonstrating its potential as a quantitative nondestructive evaluation tool for drilled shaft quality assurance and integrity assessment.

17. Key Words Drilled shaft imaging, crosshole sonic logging, P wave velocity, full-waveform inversion, acoustic wave	18. Distribution Statement No restrictions.		
19. Security Classif. (of this report) Unclassified	20. Security Classif. (of this page) Unclassified	21. No. of Pages 79	22. Price

Form DOT F 1700.7 (8-72) Reproduction of completed page authorized

ACKNOWLEDGMENTS

The researchers would like to thank the Florida Department of Transportation (FDOT) for the financial support to carry out this research, the State Materials Office in Gainesville for providing access and assisting with many of the field tests.

EXECUTIVE SUMMARY

Drilled shafts are among the most widely used deep foundation systems for bridges and other critical transportation infrastructure because of their high load-carrying capacity and adaptability to varying subsurface conditions. However, defects can develop during excavation, reinforcement placement, and concrete casting, including soil intrusion, concrete segregation, slurry or debris inclusions, necking, voids, and soft-bottom conditions. These anomalies can compromise structural integrity, reduce foundation capacity, increase settlement, and adversely affect long-term durability and service life. crosshole sonic logging (CSL) is currently the most common nondestructive testing method used for drilled shaft quality assurance, providing valuable information on concrete quality between access tubes installed within the reinforcement cage. However, conventional CSL interpretation relies primarily on first-arrival times and signal energy measurements along individual tube pairs, offering only indirect and localized assessments of shaft conditions. Consequently, it has limited capability to directly image the full shaft cross-section, accurately delineate shaft boundaries, or quantify the size, shape, and extent of defects.

This study developed, optimized, and field-validated a two-dimensional ultrasonic full waveform inversion (2D UFWI) framework for drilled shaft imaging using CSL waveform data. The proposed method uses full ultrasonic waveforms, rather than only first-arrival information, to reconstruct two-dimensional P-wave velocity distributions. The inversion framework combines acoustic wavefield simulation, adjoint-state gradient calculation, regularized model updating, tube-pair velocity constraints, Hessian-based gradient scaling, and total variation denoising. The method does not require prior knowledge of the shaft boundary, concrete volume, or defect geometry.

Synthetic studies were first performed on drilled shafts without defects, with internal defects, and with external boundary defects. The results showed that the proposed UFWI method can reconstruct shaft boundaries and identify localized velocity anomalies associated with defective concrete or soil-related inclusions. Additional parametric studies evaluated CSL tube configurations for 4-ft, 6-ft, and 8-ft diameter shafts. The results indicated that at least five access tubes are required for reliable defect detection, while one tube per foot of shaft diameter is recommended for shafts 6 ft in diameter or larger to improve boundary reconstruction and defect characterization.

Field validation was conducted with a full-scale 6-ft-diameter, 40-ft-long drilled shaft constructed at the Florida Department of Transportation (FDOT) Hawthorne test pit. The shaft included six CSL tubes, fiber-optic temperature-sensing cable, and intentionally embedded anomalies representing concrete segregation/aggregate-rich material, necking/soil inclusion, slurry inclusion, and a soft-bottom condition. Field CSL data were collected at 2-cm depth intervals over approximately 11.5 m and processed using frequency filtering, energy-based channel screening, and time windowing before inversion. The reconstructed 2D velocity slices were stacked to form a three-dimensional representation of the shaft condition.

The field results showed that UFWI successfully reconstructed the shaft boundary and detected the embedded defects. The aggregate-rich, necking/soil-inclusion, slurry-inclusion, and soft-bottom anomalies were recovered at depths and locations generally consistent with the documented as-built conditions. Although the reconstructed anomalies were smoother and more diffuse than the true physical defect shapes, the results demonstrate the capability of UFWI to detect and localize multiple defect types under realistic field conditions. Thermal profiling provided complementary evidence for several anomaly depths but showed lower spatial resolution and did not resolve all defects.

Overall, this project demonstrates that 2D UFWI is an effective nondestructive imaging tool for drilled shaft integrity assessment. Compared with conventional CSL interpretation, UFWI provides more direct information on shaft geometry, boundary condition, cover-thickness variation, and defect location. The results support the practical use of UFWI as an advanced imaging approach for drilled shaft quality assurance in transportation infrastructure.

TABLE OF CONTENTS

Page

LIST OF FIGURES

Figure page

Chapter 1 - INTRODUCTION

1.1 Background

Drilled shafts are widely used as deep foundation elements for bridges and other transportation infrastructure because of their high axial and lateral load capacity, adaptability to variable subsurface conditions, and ability to transfer structural loads to competent bearing strata (Salgado, 2022). However, the integrity of drilled shafts is strongly influenced by field construction conditions. Defects may develop during drilling, reinforcement placement, or tremie concreting due to borehole instability, soil intrusion, poor concrete flow, slurry contamination, aggregate segregation, necking, or inadequate base cleaning (Iskander et al., 2003; Mullins, 2010). These anomalies are embedded within the shaft and cannot be directly inspected after construction. If not properly identified, these defects may reduce load-transfer capacity, compromise durability, and impair long-term foundation performance (Petek et al., 2012).

Crosshole sonic logging (CSL) is commonly used for drilled shaft integrity evaluation and is standardized for ultrasonic testing of concrete deep foundation elements (Camp Iii et al., 2007). CSL measurements provide useful information on first-arrival time, apparent wave velocity, signal energy, and waveform quality between access tubes. However, conventional CSL interpretation is primarily based on one-dimensional tube-pair measurements. As a result, it has limited capability to directly image the full shaft cross-section, delineate the shaft boundary, or characterize the geometry of defects located outside the reinforcement cage or near the concrete–soil interface (Hong et al., 2019). Thermal profiling (TP), including embedded fiber-optic temperature measurements, can provide complementary information on hydration-related temperature anomalies in drilled shafts (Mullins, 2010). However, TP generally provides lower spatial resolution and is more effective for identifying approximate anomaly depths than for resolving detailed cross-sectional defect geometry (Mullins & Winters, 2011).

These limitations motivate the development of advanced inversion-based imaging methods that use the full ultrasonic waveform information rather than only first-arrival time or signal amplitude. Ultrasonic full waveform inversion (UFWI) is a physics-based imaging approach that reconstructs material property distributions by minimizing the difference between measured and simulated waveforms. The method is based on acoustic wave propagation theory (Aki & Richards, 2002; S. Yang et al., 2019), inverse problem theory (Tarantola, 2005), adjoint-state gradient calculation (Plessix, 2006), and iterative optimization of the model parameters (Nocedal & Wright, 2000). Compared with conventional CSL analysis, UFWI can use waveform phase, amplitude, and scattering information to reconstruct two-dimensional P-wave velocity distributions, providing a more direct image of shaft geometry and internal or boundary-related anomalies (Kordjazi et al., 2021). However, its application to drilled shaft integrity assessment remains challenging because the inverse problem is highly nonlinear, ill-posed, and sensitive to limited acquisition geometry, measurement noise, uncertain source characteristics, and modeling errors.

To address these limitations, this study presents a 2D ultrasonic FWI framework for drilled-shaft defect imaging that combines adjoint-state waveform inversion, Tikhonov regularization, measured tube-pair velocity constraints, and approximate Hessian-based gradient scaling, followed by TV denoising using the split Bregman method. The proposed framework is designed to improve inversion stability, reduce artifacts caused by limited CSL acquisition geometry, preserve sharp velocity contrasts associated with defects and shaft boundaries, and enhance the interpretability of reconstructed velocity images. Unlike conventional CSL interpretation, the method does not require prior knowledge of the shaft boundary, concrete volume, or defect geometry. Instead, the shaft condition is inferred directly from the measured ultrasonic waveforms through iterative updating of the P-wave velocity model.

In the earlier stages of this project, the 2D ultrasonic FWI algorithm was developed and evaluated using synthetic drilled shaft models with defect-free, internal-defect, and external-defect conditions. Additional parametric studies were conducted to assess the effects of shaft diameter, defect type, and CSL tube configuration, providing guidance for the full-scale field validation program. The final stage focuses on field implementation using a full-scale drilled shaft constructed at the FDOT Hawthorne test pit with controlled embedded anomalies, including concrete segregation/aggregate-rich material, necking/soil inclusion, slurry inclusion, and a simulated soft-bottom condition.

This method enables high-resolution imaging of drilled shaft conditions by reconstructing two-dimensional P-wave velocity distributions from CSL waveform data and stacking the depth-wise slices to form a three-dimensional representation of the shaft. It supports detection of construction defects, characterization of shaft boundaries and cover-thickness variations, and quality assurance for transportation foundation construction.

1.2 Motivation and outline of the study

The motivation for this study is to advance drilled shaft integrity assessment from conventional tube-pair interpretation toward high-resolution cross-sectional and volumetric imaging. Although conventional CSL testing is effective for identifying potential anomalies along individual tube paths, it does not directly provide a complete image of the shaft boundary, defect geometry, or the spatial relationship between defects and the reinforcement cage. This limitation is particularly important for defects located near the shaft perimeter, outside the rebar cage, or close to the shaft base, where one-dimensional measurements may not fully characterize the extent or severity of the anomaly.

The proposed UFWI approach addresses this need by using the complete waveform information recorded from CSL measurements, including arrival time, phase, amplitude, and early scattered-wave content. By reconstructing two-dimensional P-wave velocity distributions at closely spaced depth intervals and stacking these slices into a three-dimensional representation, the method provides a more direct visualization of shaft condition. This capability is intended to improve the detection and localization of construction-related defects such as soil intrusion, necking, concrete segregation, slurry inclusion, and soft-bottom conditions. It also provides information on shaft boundary geometry and potential cover-thickness variations, which are important for evaluating construction quality and long-term durability.

This final report documents the development, optimization, and field validation of the UFWI-based drilled shaft imaging framework. The 2D UFWI method was initially developed and validated using synthetic data for defect-free shafts and shafts with internal and external defects (Chapter 2). Test configurations and acquisition geometries were subsequently analyzed to optimize field testing and data-processing strategies, including the effects of shaft diameter, defect type, and CSL tube configuration (Chapter 3). The method was then applied to full-scale field experiments using a 6-ft-diameter, 40-ft-long drilled shaft constructed at the FDOT Hawthorne test pit with intentionally embedded anomalies at 10-ft (3.0-m) depth intervals (Chapter 4). Field CSL data were preprocessed and inverted at 2-cm (0.8-in.) depth intervals to generate two-dimensional P-wave velocity slices, which were stacked to form a three-dimensional representation of shaft condition. The UFWI results were compared with documented as-built defect locations and thermal profiling measurements to evaluate the method's capability for detecting, localizing, and characterizing drilled shaft defects under realistic field conditions.

Chapter 2 - DEVELOPMENT OF 2D ULTRASONIC FULL WAVEFORM INVERSION (UFWI) ALGORITHM (TASK 1)

2.1 Introduction

This chapter presents the development of the two-dimensional UFWI algorithm used for drilled shaft imaging. The objective of the algorithm is to reconstruct cross-sectional P-wave velocity distributions from CSL waveform data, thereby providing spatially continuous images of shaft conditions. The reconstructed velocity models serve as the basis for identifying shaft boundaries, evaluating material uniformity, and detecting anomalous zones associated with construction defects.

Drilled shaft imaging with FWI presents several technical challenges. Unlike conventional geophysical or medical imaging applications, drilled shafts are characterized by limited access geometry, where ultrasonic sources and receivers are restricted to a small number of access tubes embedded within the reinforcement cage. In addition, strong velocity contrasts between concrete, surrounding soil, and potential defects produce complex wave phenomena, including reflections, refractions, diffractions, and boundary scattering. These effects result in highly nonlinear inverse problems that are sensitive to acquisition geometry, model parameterization, and measurement noises.

To address these challenges, a physics-based inversion framework was developed using acoustic wave propagation modeling, adjoint-state gradient computation, iterative model updating, and regularization techniques. The algorithm incorporates measured tube-pair velocity constraints, approximate Hessian-based gradient scaling, and total variation (TV) denoising to improve inversion stability and image quality. The following sections describe the theoretical formulation of the forward and inverse problems, numerical implementation of the UFWI algorithm, regularization strategies, and validation using synthetic drilled shaft models.

2.2 2D Ultrasonic FWI algorithm

2.2.1 Forward simulation in time domain

Measured waveform data from the standard CSL are mostly pressure waves, as shear waves cannot propagate through water-filled tubes. Given that the P-wave wavelength in concrete at 20–80 kHz (5–20 cm) is several times larger than typical aggregate or rebar sizes, the resulting bulk anisotropy is negligible (By et al., 2017; Kordjazi et al., 2021). Thus, CSL data can be modeled as acoustic waves in isotropic medium. The wave propagation is simulated using the second-order acoustic wave equations (Aki & Richards, 2002):

$$\frac{\partial^2 p(x,y,t)}{\partial t^2} = V^2(x,y)\left(\frac{\partial^2 p(x,y,t)}{\partial x^2} + \frac{\partial^2 p(x,y,t)}{\partial y^2}\right) + f(x_S, y_S, t) \qquad (2\text{-}1)$$

where x and y represent the lateral distances in x-y -plane; t denotes time; $p(x,y,t)$ is the pressure field, $V(x,y)$ is the P-wave velocity, and $f(x_S, y_S, t)$ denotes the source term acting on the pressure field, where (x_S, y_S) specifies the source location (e.g., access tube location).

To numerically solve Eq. ((2-1), we employ the central finite-difference scheme to approximate the spatial and temporal derivatives. The second partial derivative operator is defined as

$$\frac{\partial^2 p}{\partial x^2} \approx \frac{p(x+h,z,t) - 2p(x,z,t) + p(x-h,z,t)}{h^2} \qquad (2\text{-}2)$$

where h is the grid points spacing (dt is used for the time step).

Equation (**Error! Reference source not found.**) in the index notation is

$$\frac{\partial^2 p}{\partial x^2} \approx \frac{p_{i+1,j}^n - 2p_{i,j}^n + p_{i-1,j}^n}{h^2} \qquad 2\text{-}3$$

where the subscript i for offset in x direction, subscript j for offset in y direction, and superscript n for time (t). Then discretized form of Equation (2-1 is given by

$$\frac{p_{i,j}^{n+1} - 2p_{i,j}^n + p_{i,j}^{n-1}}{dt^2} \approx V_{i,j}^2 \frac{p_{i+1,j}^n + p_{i,j+1}^n - 4p_{i,j}^n + p_{i-1,j}^n + p_{i,j-1}^n}{h^2} + f \qquad 2\text{-}4$$

where we can solve for $p_{i,j}^{n+1}$ as

$$p_{i,j}^{n+1} \approx V_{i,j}^2 \frac{p_{i+1,j}^n + p_{i,j+1}^n - 4p_{i,j}^n + p_{i-1,j}^n + p_{i,j-1}^n}{h^2} dt^2 + f dt^2 + 2p_{i,j}^n - p_{i,j}^{n-1} \qquad 2\text{-}5$$

To manage the computational boundaries effectively, Perfectly Matched Layers (PML) are implemented along all four boundaries (Komatitsch & Martin, 2007). This technique helps absorb outgoing waves, thereby minimizing reflections and truncation errors at the boundaries. Regarding the initial conditions, both pressures are set to zero at the commencement of the simulation (time zero).

2.2.2Full waveform inversion

For clarity in the following discussion, the vector is defined as $\mathbf{x} = (x, y)$ to represent the spatial coordinates of a point in 2D space. The pressure field is denoted by $\mathbf{p}(\mathbf{x_r}, \mathbf{x_s}, \mathbf{v}, t)$, where $\mathbf{x_r}$ and $\mathbf{x_s}$ are the receiver and source locations, and $\mathbf{v}$ represents the 2D P-wave velocity model, and t is time. Since the observed field data remain fixed during inversion and are independent of the iterative model updates, the pressure field for the observed data is denoted as $\mathbf{p}(\mathbf{x_r}, \mathbf{x_s}, \mathbf{v_m}, t)$. To update the model, the adjoint-state method is employed to minimize an objective function consisting of a waveform misfit term and two regularization terms:

$$E(\mathbf{v}) = E_{data}(\mathbf{v}) + \lambda_{Tik} E_{Tik}(\mathbf{v}) + \lambda_{pair} E_{pair}(\mathbf{v}) \qquad 2\text{-}6$$

where $E_{data}(\mathbf{v})$, $E_{Tik}(\mathbf{v})$, and $E_{pair}(\mathbf{v})$ denote the waveform data misfit, the Tikhonov regularization term, and the tube-pair velocity constraint term, respectively, and λ_{Tik}, and λ_{pair}

are their corresponding weighting parameters controlling the relative contribution of each term. Here, the objective function $E(\mathbf{v})$ is a scalar quantity that represents the total inversion cost.

The waveform data-misfit term is defined as the least-squares difference between observed and simulated waveforms over all source-receiver pairs and time samples:

$$E_{data}(\mathbf{v}) = \frac{1}{2}\sum_{i=1}^{N_s}\sum_{j=1}^{N_r}\left\|\mathbf{p}_{\text{cal}}(\mathbf{x_j}, \mathbf{x_i}, \mathbf{v}, t) - \mathbf{p}_{\text{obs}}(\mathbf{x_j}, \mathbf{x_i}, \mathbf{v}_{\boldsymbol{m}}, t)\right\|_2^2 \qquad \text{2-7}$$

where N_s and N_r are the number of sources and receivers, $\mathbf{p}_{\text{cal}}$ is the simulated pressure field obtained from forward modeling by solving Eq. ((2-1), $\mathbf{p}_{\text{obs}}$ is the experimentally measured pressure field.

To minimize the objective function, the gradient without regularization is computed by cross-correlating the forward and back-propagated wavefields as follows (Plessix, 2006):

$$g(\mathbf{v}) = -\frac{2}{v^3(\mathbf{x})}\sum_{s=1}^{N_s}\int_0^T \frac{\partial \mathbf{p}(\mathbf{x}, \mathbf{x_s}, \mathbf{v}, t)}{\partial \mathrm{t}} \frac{\partial \mathbf{p}_{\text{res}}(\mathbf{x}, \mathbf{x_r}, \mathbf{v}, T - t)}{\partial \mathrm{t}} dt \qquad \text{2-8}$$

where $g(\mathbf{v}) = \frac{\partial E(\mathbf{v})}{\partial \mathbf{v}}$; N_s is the number of sources; T is the maximum recording time; and $\mathbf{p}_{\text{res}}$ denotes the back-propagated residual wavefield obtained by injecting the time-reversed data residuals at all receiver locations $\mathbf{x_r}$. Because the residual sources are applied simultaneously at all receiver positions, their contributions are superposed in $\mathbf{p}_{\text{res}}$. This adjoint-state formulation avoids the explicit construction of the large sensitivity (Jacobian) matrix required by direct differentiation, making it much more efficient in both computational cost and memory usage.

As ultrasonic FWI is a highly nonlinear and ill-posed inverse problem, regularization is essential for ensuring stability in the optimization process, especially in cases with sharp material property contrasts. The same matrix-free regularization scheme as in (B. Yang & Tran, 2026) is adopted, which improves computational efficiency while maintaining robust constraint enforcement. The total gradient for Eq (**Error! Reference source not found.**) become

$$g_t^r(\mathbf{v}) = g(\mathbf{v}) + \lambda_{Tik} L_{2D}^2 v_{i,j} + \lambda_{pair}\, g_{\text{pair}}^{\text{2D}}(\mathbf{v}), \qquad \text{2-9}$$

where $g^r(\mathbf{v})$ denotes the total regularized gradient; $L_{2D}^2 v$ denotes the Laplacian term given by (A - 6); and $g_{\text{pair}}^{\text{2D}}(\mathbf{v})$ is the gradient of the pair-velocity regularization term given by (B - 5). The details for $L_{2D}^2 v$ and $g_{\text{pair}}^{\text{2D}}(\mathbf{v})$are given in Appendix A, B. Coefficients λ_{Tik} and λ_{pair} are nonnegative regularization parameters, given by:

$$\lambda_{Tik} = \alpha \frac{\|g(\mathbf{v})\|}{\|L^2 v\|} \qquad \text{2-10}$$

$$\lambda_{pair} = \gamma \frac{\|g(\mathbf{v})\|}{\|g_{pair}(\mathbf{v})\|}, \quad 2\text{-}11$$

where $\|\cdot\|$ denotes the Euclidean norm. The parameter α is a regularization factor that controls the model's smoothness; higher values yield to a smoother model. Values of α in the range 0.3 to 0.8, and γ was gradually decreased from 1.0 to 0.0 during the inversion to progressively reduce its influence.

In addition, to balance the gradient, improve inversion quality outside the rebar cage, and suppress artifacts, a scaling matrix is applied as a preconditioner. This matrix represents model sensitivity by integrating the pointwise product of the forward-wavefield energy and the adjoint (time-reversed residual) wavefield energy over time and across all sources as follows (Yang et al., 2025; Yang & Tran, 2026):

$$\mathbf{H} = \epsilon + \mathbf{w}, \quad 2\text{-}12$$

where $\mathbf{w} = \int_{s=1}^{N_s} \int_{t=0}^{T} \mathbf{p}^2(\mathbf{x}, \mathbf{x_s}, \mathbf{v}, t) \cdot \mathbf{p}_{\text{res}}^2(\mathbf{x}, \mathbf{x}_{\boldsymbol{r}}, \mathbf{v}, T - t) dt ds$, and $\epsilon = \gamma' \max(\mathbf{w})$, which is a small positive number introduced to prevent the inversion of infinitesimally small values; and $\gamma' = 10^{-3}$ to 2×10^{-3} was found to be suitable for tests described in this paper.

The scaling matrix can then be used as a preconditioning matrix for the gradient:

$$G^r((\mathbf{v}) = \mathbf{H}^{-1} g_t^r((\mathbf{v}). \quad 2\text{-}13$$

The medium model is then iteratively updated by:

$$v_{n+\mathbf{1}}(\mathbf{x}) = v_n(\mathbf{x}) - \alpha_n G_n^{\mathrm{r}}(\mathbf{v}), \quad 2\text{-}14$$

where n is the iteration index and α_n is the step length. After obtaining the preliminary inverted model $v_{n+1}(x)$, we treat it as an image contaminated by aliasing-like artifacts and apply TV denoising using the split Bregman method to refine the result:

$$v_{n+\mathbf{1}}(\mathbf{x}) \leftarrow \Gamma(v_{n+\mathbf{1}}(\mathbf{x})), \quad 2\text{-}15$$

where Γ is the TV denoising operator. Additional details of this operation are provided in Appendix C. The optimal step length is estimated using the parabolic fitting method. To summarize the proposed inversion procedure, the algorithmic workflow is presented in **Figure 2.1**.

The inversion is terminated when one of the following criteria is satisfied: the maximum number of 400 iterations is reached, the relative change in the least-squares error E between successive iterations remains below 0.1% for 50 consecutive iterations, or the error function increases for more than 10 consecutive iterations after exceeding the minimum error achieved during the inversion, indicating that no further improvement can be obtained. In trial runs, the misfit typically leveled off after approximately 300-400 iterations for both synthetic and field data; thus, the 400-iteration limit was adopted to ensure convergence under varying noise conditions without unnecessary additional computation.

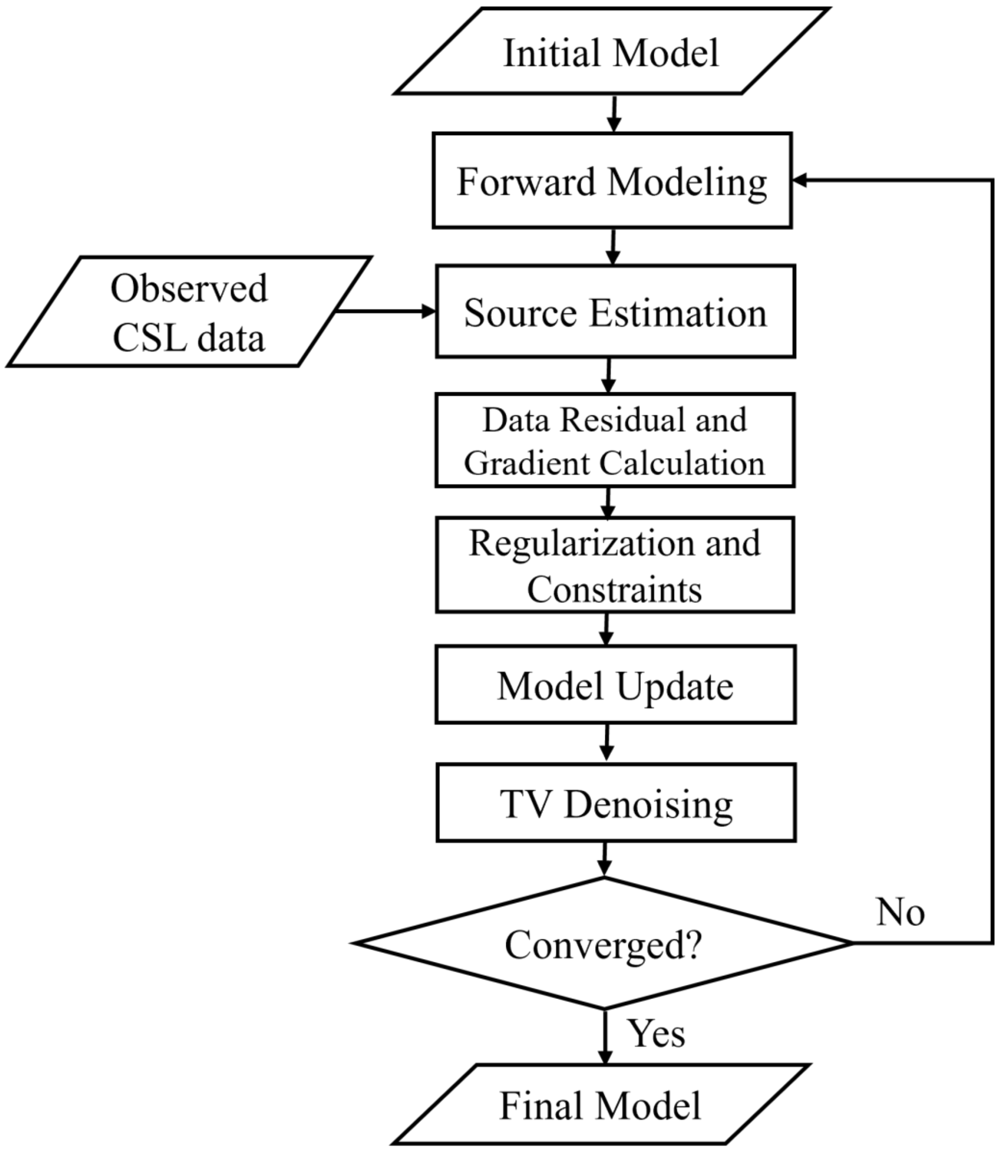

Figure 2.1 Workflow of the presented ultrasonic FWI for drilled shaft imaging.

2.3 Results

The 2D UFWI algorithm was first tested on a synthetic experiment with known Vp model to evaluate its accuracy, before applying to field experiments (Task 3). The implementation of synthetic experiments plays a pivotal role in validating the algorithm. These experiments are designed to simulate various defect scenarios, specifically targeting models with common foundation defects, thereby enabling assessment and refinement of the algorithm. Shaft without defect

2.3.1Shaft without defect

This experiment begins with a predefined synthetic model designed to replicate a potential field condition, referred to as the true model. This model serves as the basis for forward simulations, generating synthetic data by capturing the model's response at receiver locations. These data are treated as surrogate field measurements and processed using the 2D UFWI algorithm. The results are then compared to the true model to evaluate the algorithm's accuracy.

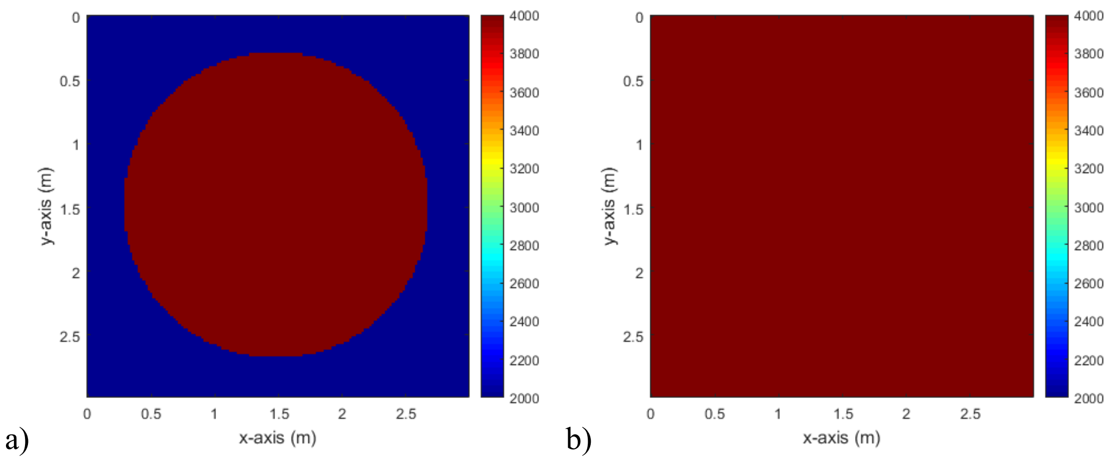

Figure 2.2 Synthetic model: a) true model used for generating synthetic data, b) initial model in the beginning of iteration.

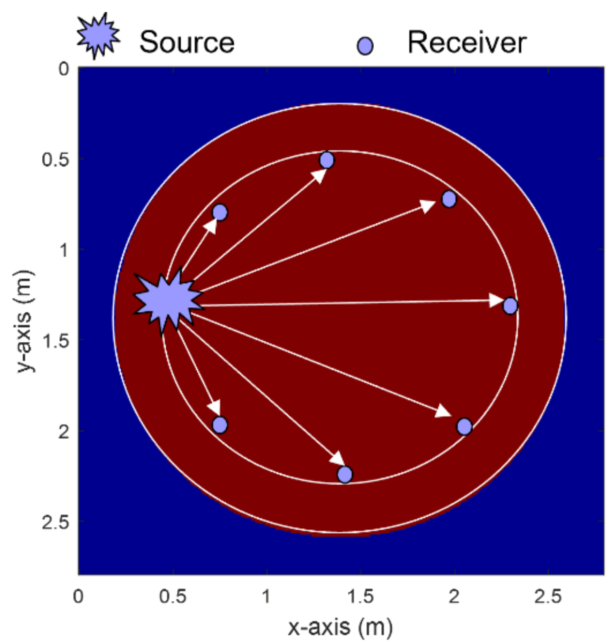

Figure 2.3 Acquisition geometry used for synthetic experiments.

The synthetic model (**Figure 2.2**a) depicts a shaft without defects, representing a well-cast structure. The shaft, with a diameter of 2.4 meters (8.0 ft), is embedded within a soil matrix (blue zone). The material properties are defined as follows: a P-wave velocity of 4,000 m/s for the concrete shaft and 2,000 m/s for the surrounding soil.

The data acquisition geometry was configured following ASTM specifications with 8 access tubes (1 tube/foot of diameter), uniformly spaced and positioned approximately one foot from the boundary as detailed in **Figure 2.3**. The first source is in tube 1, and the remaining 7 tubes (tubes 2 to 8) are for receivers. Then the source is moved to the next tube and so on, for a total of 8 sources with 7 receivers for each source.

The analyzed medium of 3 × 3 m (10 × 10 ft) was divided into a grid of 150 × 150 cells, each cell of 2 × 2 cm (0.8”). For the generation of synthetic waveform data, a Ricker source wavelet was employed. These synthetic data sets were subsequently used for 2D UFWI analysis, as if they were acquired from an actual drilled shaft.

The initial velocity model (**Figure 2.2**b) was chosen as a uniform (homogeneous) distribution of Vp, derived from the average travel time calculated following standard CSL analysis. The frequency content of the inversion data primarily spans from 4 to 15 kHz. For accurate wavefield modeling, a 2 cm grid spacing was implemented during both forward wave simulation and model updates.

The inversion procedure was terminated under any of the following conditions: (1) reaching a maximum of 400 iterations, (2) failing to determine an optimal step length, or (3) attaining less than 0.1% improvement in the least-squares misfit over 20 consecutive iterations. The typical computational time for each inversion run was about 30 minutes, performed on a Dell Precision 5820 Tower (Intel Xeon CPU W-2145, 3.70 GHz, 8 cores, 64 GB RAM).

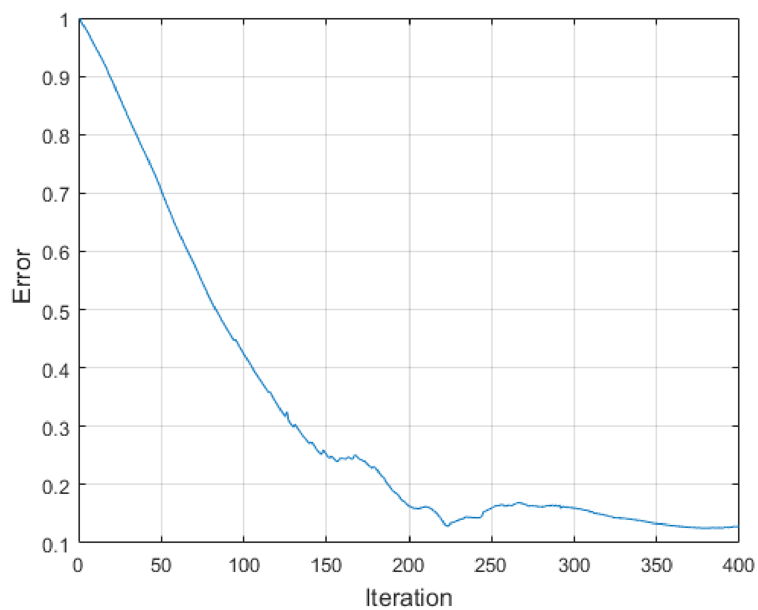

Figure 2.4 Normalized least squares error versus the inversion iteration number.

Figure 2.4 shows the iterative evolution of the error (misfit) function, dropping significantly from an initial value of approximately 1.0 to 0.1289 at the final iteration. This substantial reduction in misfit reflects the effectiveness of the waveform tomography approach in refining the subsurface velocity model.

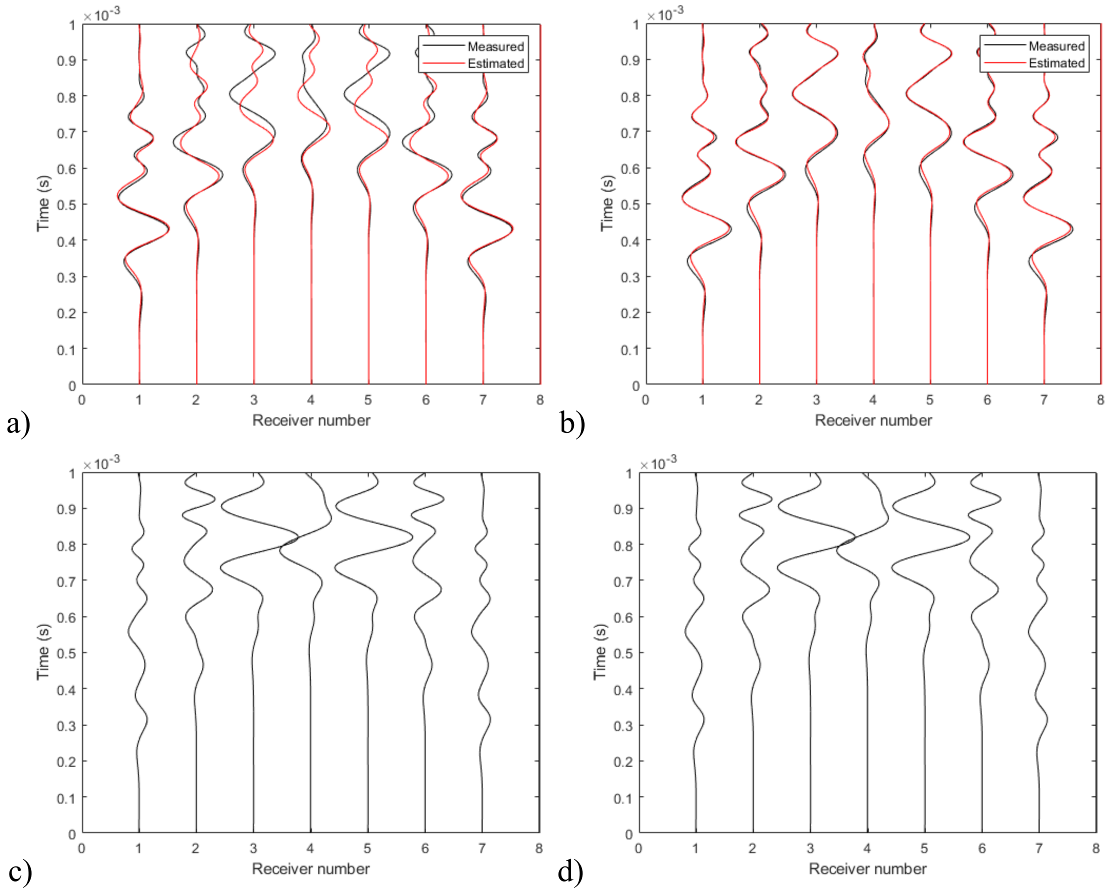

Figure 2.5 Synthetic model with interior defect: waveform comparison: a) observed data and estimated data associated with the initial model, b) observed data and estimated data associated with the final inverted model, c) residual associated with the initial model, and d) residual associated with final inverted model. Both residuals in figures c and d are scaled by a factor of 10 for better visualization.

Figure 2.5 compares observed and modeled waveforms at two key stages of the inversion. In **Figure 2.5**a, the mismatch between observed and computed data is evident because the initial model (**Figure 2.2**b) does not accurately represent the drilled shaft. By contrast, **Figure 2.5**b demonstrates excellent agreement after the model has been iteratively updated, with final residuals across all receivers approaching zero. This near-perfect alignment of observed and modeled data strongly indicates that the inversion algorithm is converging toward the global minimum. To enhance clarity, the residuals are magnified tenfold in **Figure 2.5**c and d.

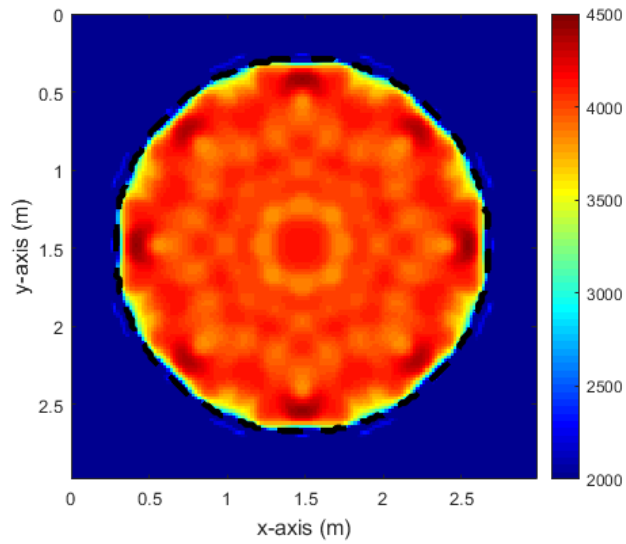

Figure 2.6 . Inverted results for shaft without defect. Blue dashed line: actual boundary; Black line: inferred boundary.

The inverted P-wave velocity (Vp) results are presented in **Figure 2.6**, where the blue dashed line represents the actual boundary, and the black line denotes the inverted boundary. Notably, the method accurately images the shaft boundary without requiring prior information, such as the estimated or design diameter, highlighting its novelty. However, ring-like patterns are observed outside the boundary, which can be attributed to regularization effects. Regularization is applied in the inversion to suppress noise and stabilize the solution. However, it can also spatially smooth or redistribute energy, leading to artifacts like rings outside the boundary. Specifically, the regularization term in Eq. (2-9) enforces connectivity by tying each cell to its four adjacent cells (top, bottom, left, right), resulting in smooth inverted models even in regions without physical boundaries.

2.3.2 Shaft with inner defect

The synthetic model (**Figure 2.7**) comprises a shaft with an inner defect, which mimics a field condition of concrete weakening (e.g. aggregate segregation). The shaft of 2.4-meter diameter (8.0 ft) is constructed in soil (blue zone), and the defect is 0.72 m (2.4 ft) in diameter. Material velocities are assumed as follows: 4,000 m/s for concrete, 2,000 m/s for soil, and 3,000 m/s for the defect.

The data acquisition geometry follows the same configuration as described in Section 0 and illustrated in **Figure 2.3**. The analyzed medium, measuring 3.0 × 3.0 m (9.8 × 9.8 ft), was discretized into a grid consisting of 150 × 150 cells, with each cell measuring 2 × 2 cm (0.8 in). A Ricker wavelet was used as the source for generating synthetic waveform data. These synthetic datasets were then processed using the 2D UFWI algorithm, treating them as though they were collected from an actual drilled shaft.

The initial Vp model (**Figure 2.2**b) was selected as a uniform distribution based on average travel times from standard CSL analysis. The frequency content of the inversion data primarily ranges from 4 to 15 kHz. In this case, the same termination criteria described in

Section 0 were applied, and each inversion run required approximately 30 minutes of computation on a Dell Precision 5820 Tower (Intel Xeon CPU W-2145, 3.70 GHz, 8 cores, 64 GB RAM).

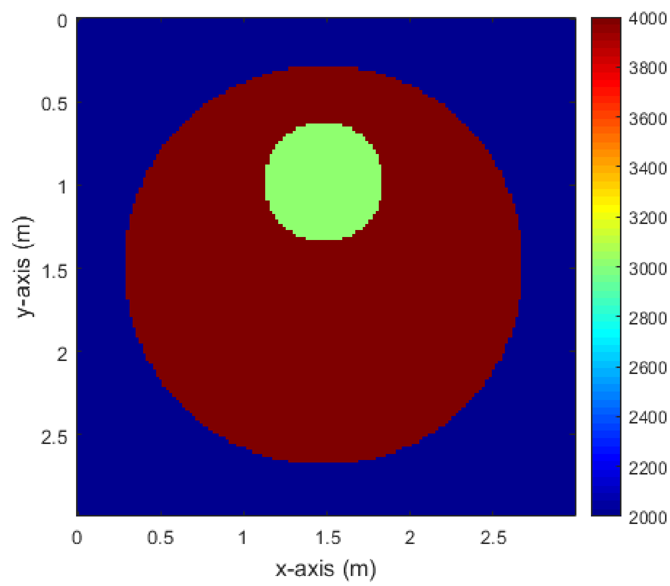

Figure 2.7 True model used for generating synthetic data.

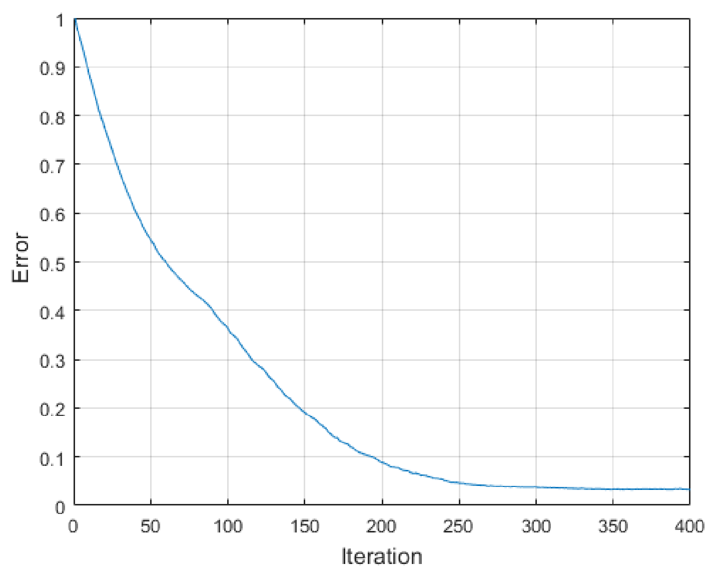

Figure 2.8 Normalized least squares error versus the inversion iteration number.

Figure 2.8 illustrates the normalized least-squares error reduction, showing a significant decrease from 1.0 at the initial iteration to 0.03 at the final iteration. **Figure 2.9** compares the observed waveforms with those modeled using both the initial and the final inverted models. Substantial improvements in waveform matching are evident, culminating in a near-perfect alignment between the observed and final modeled data, and residuals approaching zero across all receivers. For clearer visualization, all residuals in **Figure 2.9**have been scaled by a factor of 10.

The inverted P-wave velocity models are presented in **Figure 2.10**, effectively capturing the shaft's overall geometry, clearly delineating its boundaries, and identifying structural anomalies through localized variations in P-wave velocity. These anomalies are resolved without relying on prior information, demonstrating the robustness and innovation of the proposed approach. However, artifacts outside the boundary arise from the regularization in Eq. 2-9, which ties each cell to its four adjacent cells, leading to smooth but slightly overextended models.

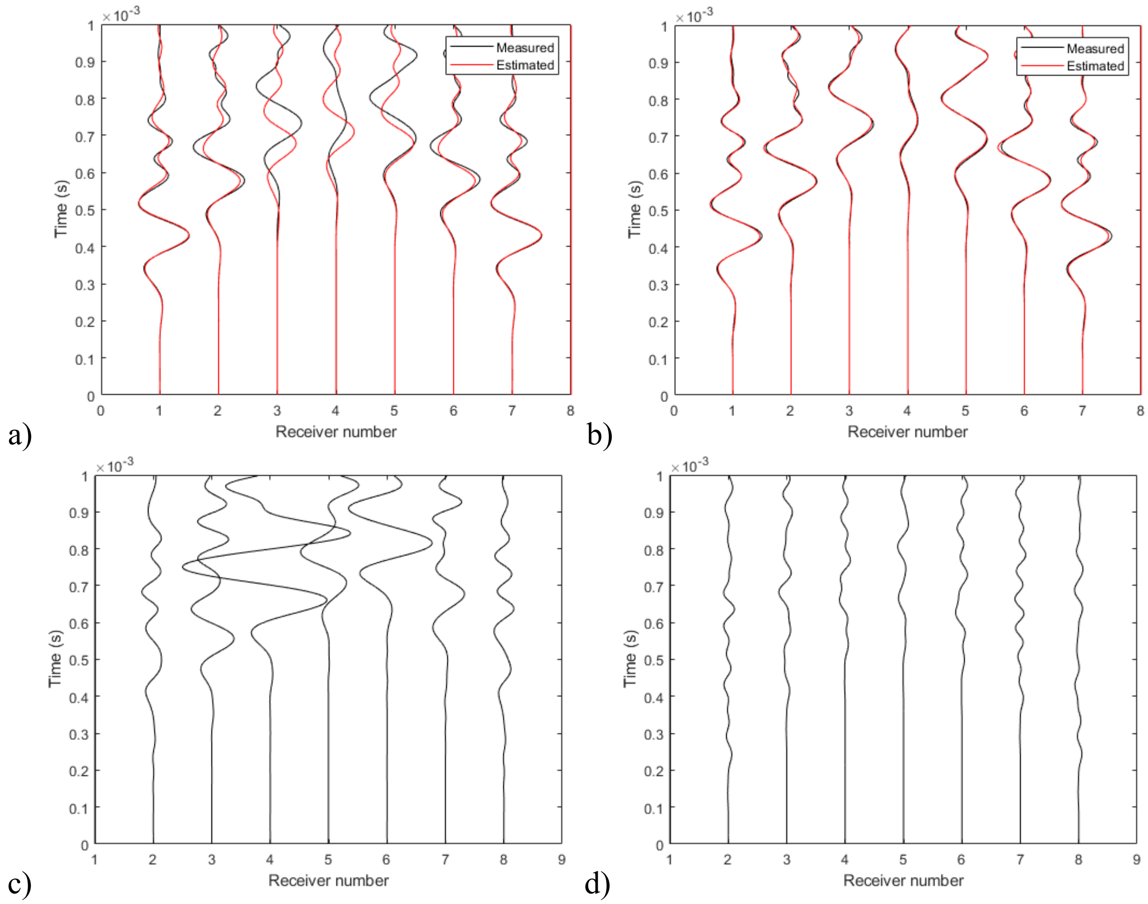

Figure 2.9 Synthetic model with interior defect: waveform comparison: a) observed data and estimated data associated with the initial model, b) observed data and estimated data associated with the final inverted model, c) residual associated with the initial model, and d) residual associated with final inverted model. Both residuals in figures c and d are scaled by a factor of 10 for better visualization.

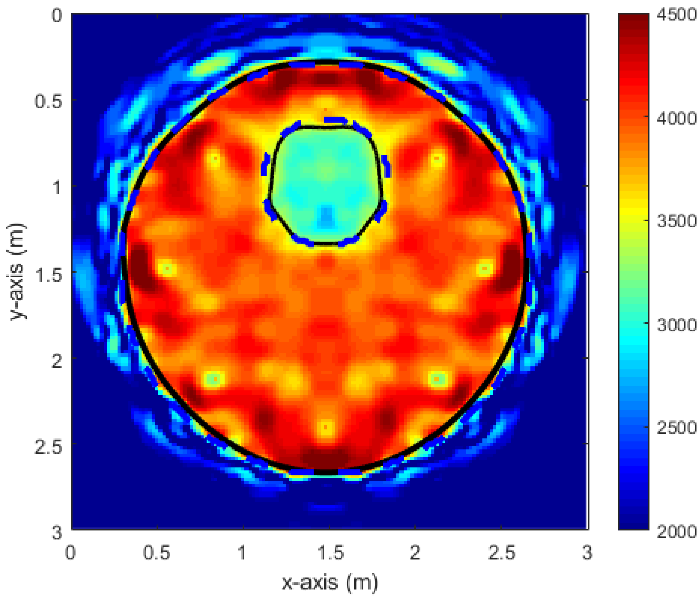

Figure 2.10 Inverted results for shaft with inner defect. Blue dashed line: actual shaft boundary and defect boundary; Black line: inferred boundary.

2.3.3 Shaft with outer defect

The algorithm was subsequently tested on a drilled shaft containing an outer defect. **Figure 2.11**represents a drilled shaft of 2.4 m diameter (8 ft) with an outer defect that mimics a soil inclusion. Such external defects are commonly observed in shaft construction due to soil caving in boreholes or improper concrete flow through the rebar cage. The P-wave velocities are set as 4,000 m/s for concrete and 2,000 m/s for soil. Data generation is the same as that of the previous experiment (section 0) with the test configuration of 8 access tubes (**Figure 2.3**). The initial model assumed a homogeneous medium with the P-wave velocity of concrete.

For inversion, the same termination criteria were applied and the analysis stopped at 362 iterations. **Figure 2.12**shows the progression of the error function over iterations. The error significantly decreases from 1.0 at the initial iteration to 0.058 at the final iteration. The observed and modeled waveforms are also compared in **Figure 2.13**. **Figure 2.13**a and b depict the initial and final waveform alignments for the first run, showcasing a notable improvement in data fit. **Figure 2.13**c and d illustrate the initial and final waveform residuals, respectively, with residuals magnified tenfold for improved clarity.

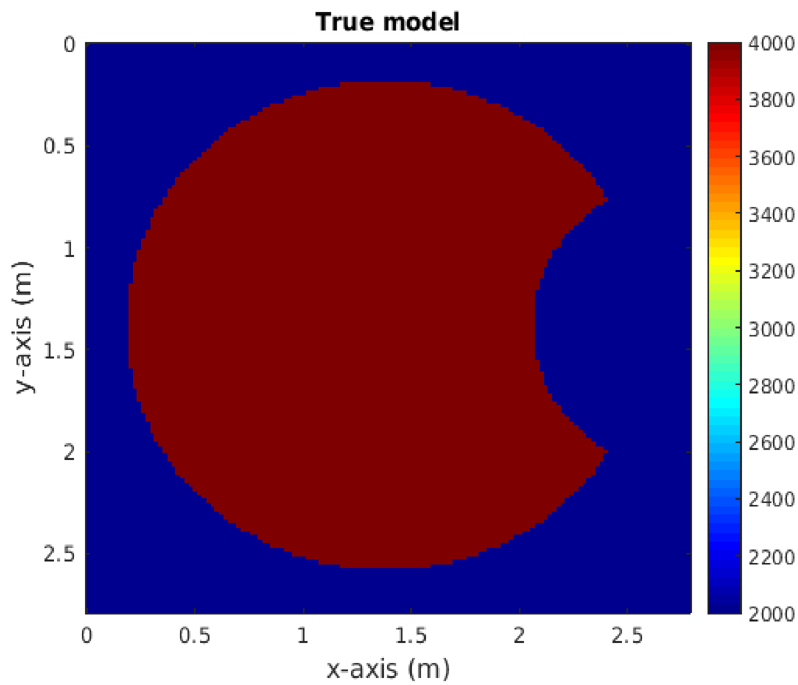

Figure 2.11 Synthetic model with outer defect.

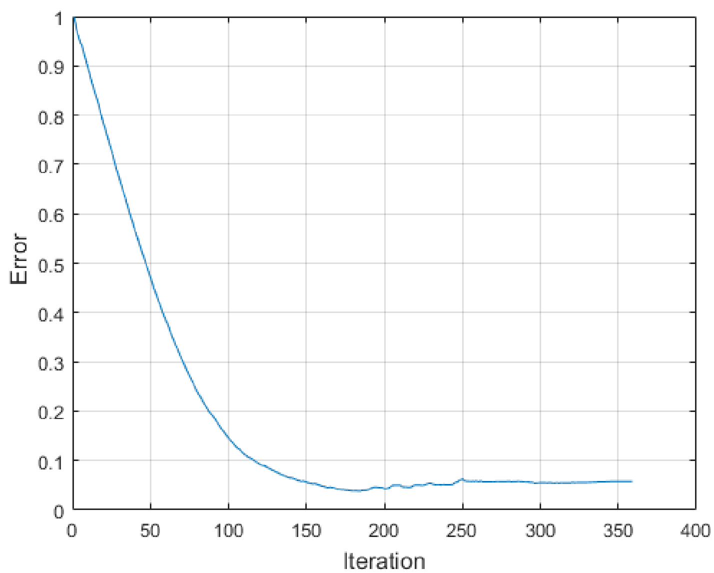

Figure 2.12 Normalized least-squares error versus the inversion iteration number.

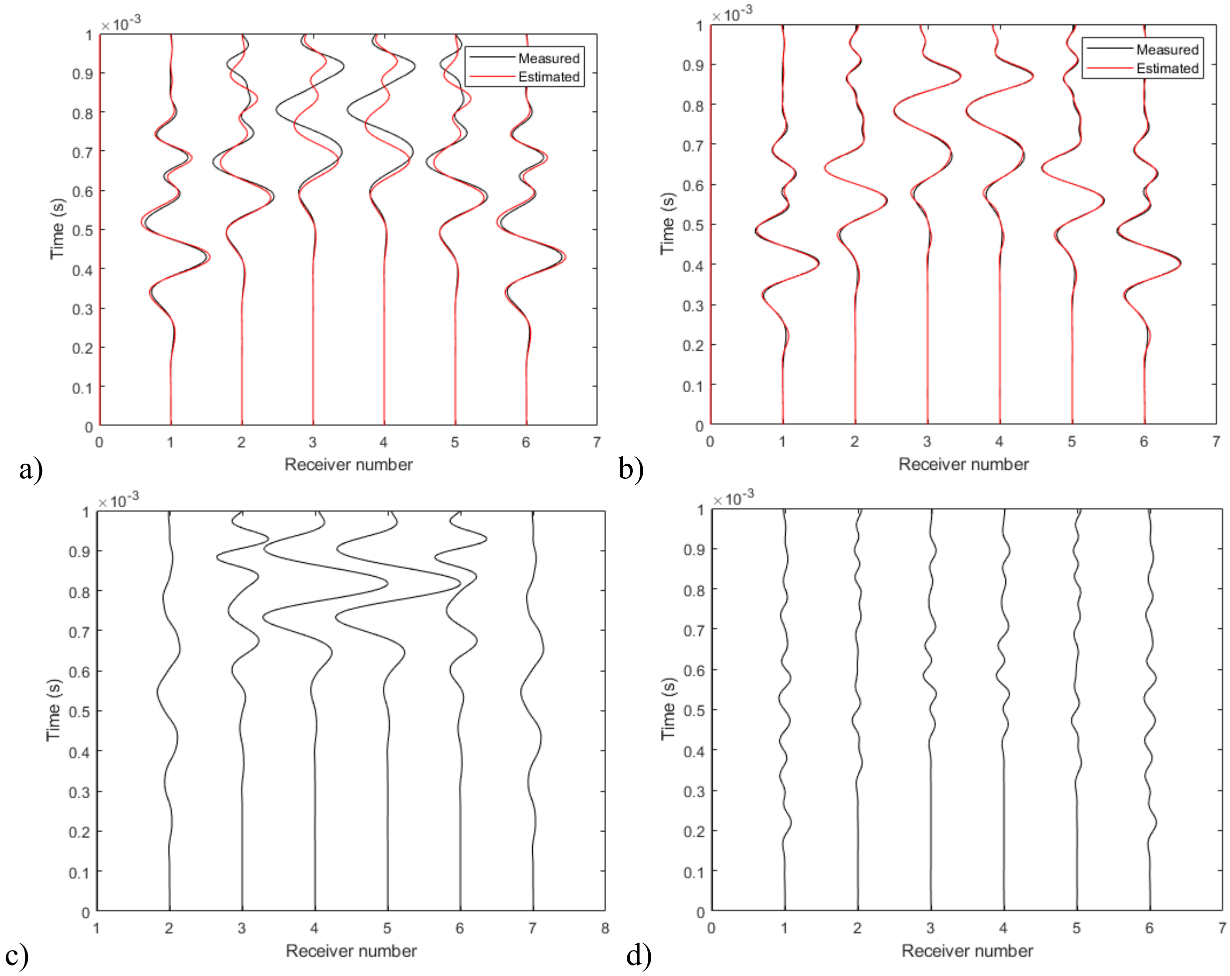

Figure 2.13 Synthetic model with interior defect: waveform comparison: a) observed data and estimated data associated with the initial model, b) observed data and estimated data associated with the final inverted model, c) residual associated with the initial model, and d) residual associated with final inverted model. Both residuals in figures c and d are scaled by a factor of 10 for better visualization.

The inverted P-wave velocity models are displayed in **Figure 2.14**. The results accurately reconstruct the shaft's overall geometry, delineate its boundaries, and reveal structural anomalies as localized deviations in P-wave velocities. These features are resolved without requiring prior information, demonstrating the robustness and innovation of the method. However, artifacts outside the shaft boundary are observed, resulting from the back-projection of residual wavefields and the regularization term in Equation 2-9. This regularization links each cell to its four adjacent neighbors, producing smooth but slightly overextended models. This reflects the inherent trade-off between model fidelity and numerical stability in the inversion process.

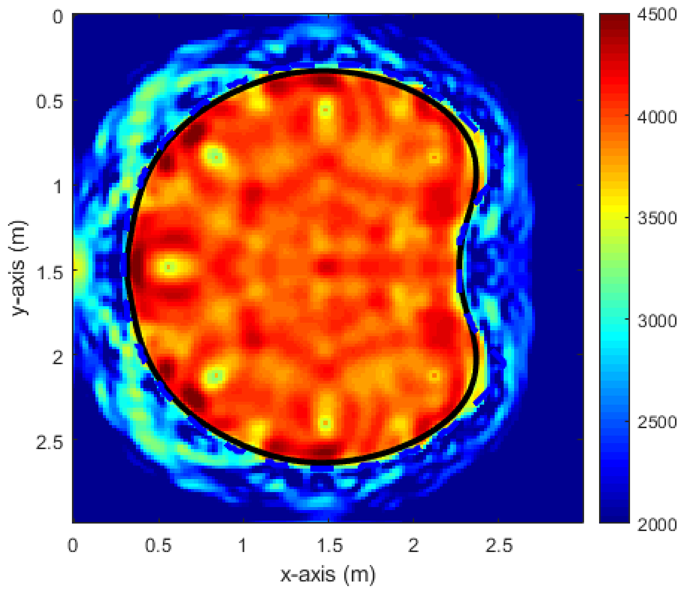

Figure 2.14 Inverted results for shaft with inner defect. Blue dashed line: actual shaft boundary and defect boundary; Black line: inferred boundary

Overall, these numerical examples highlight the method's capability to detect and delineate structural anomalies in drilled shafts. The accurate identification of defects and shaft boundaries, even under challenging conditions, underscores the potential of this approach for defect detection and resolution.

Chapter 3 - OPTIMIZATION OF FIELD TEST CONFIGURATIONS (TASK 2)

3.1 Introduction

An advanced 2D UFWI method and its computational algorithm were developed for imaging drilled shafts (Chapter 2). This chapter presents the optimization of the algorithm through parametric studies aimed at identifying optimal test configurations, specifically the minimum number of CSL tubes required to reliably detect foundation defects. Two defect types are considered: internal flaws within the concrete cross-section and external flaws near the concrete–soil interface. Simulations were conducted for 4-ft, 6-ft, and 8-ft diameter shafts using models that reflect representative field conditions. The UFWI algorithm was applied to synthetic ultrasonic data to reconstruct P-wave velocity (Vp) profiles, enabling direct comparison between the inferred and true shaft boundaries.

The primary goal is to establish the minimum CSL tube count needed to accurately detect foundation defects across various shaft diameters. While CSL tubes are typically installed at a density of one tube per foot of shaft diameter, simulations explored configurations ranging from 4 to 8 tubes to determine the threshold at which inversion results become reliable. By accounting for defect type, shaft size, and CSL layout, this task aims to develop practical guidelines for implementing FWI-based imaging in drilled shaft inspections. The results will guide the design of field validation experiments in Task 3 using a shaft with embedded defects.

3.2 Synthetic experiments on shafts with internal defects

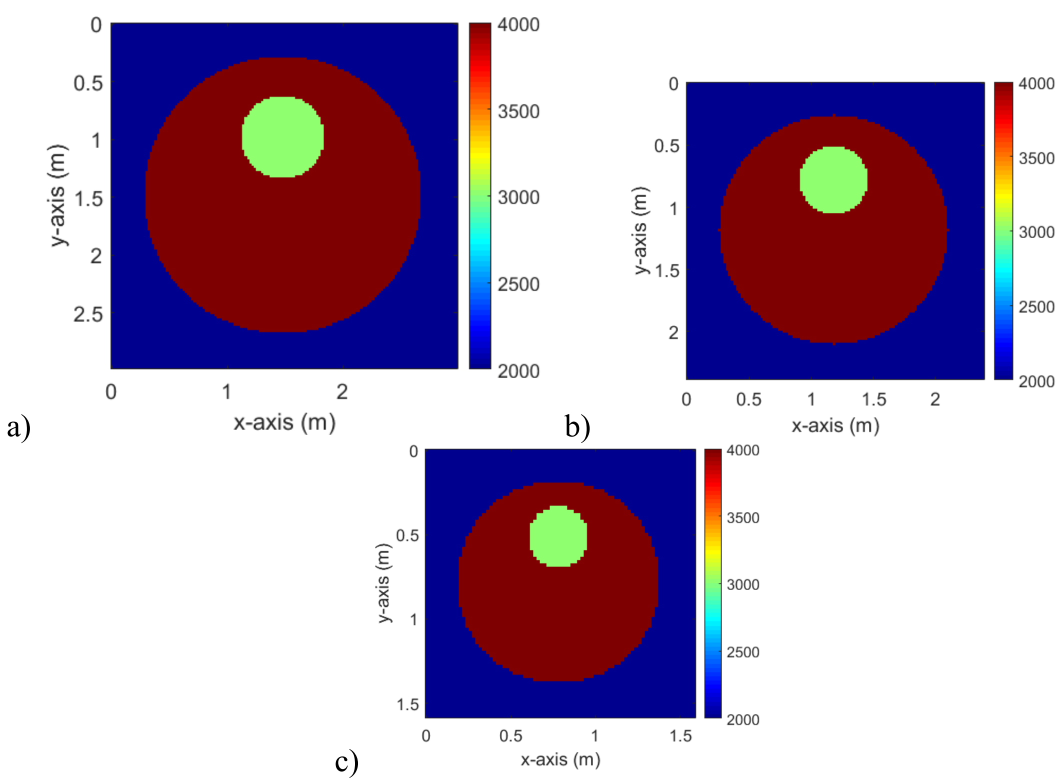

Figure 3.1 True model used for generating synthetic data: a) 8-ft diameter shaft, b) 6-ft diameter shaft, c) 4-ft diameter shaft.

To systematically evaluate the effects of defect type, shaft size, and sensor configuration, a series of synthetic models of drilled shafts with internal defects was created (**Figure 3.1**). Each model represents a circular concrete shaft embedded in homogeneous soil, with shaft diameters of 8 ft, 6 ft, and 4 ft, as illustrated in **Figure 3.1**a, b, and c, respectively. Material P-wave velocities (Vp) were assigned based on typical field conditions: 4,000 m/s for concrete and 2,000 m/s for the surrounding soil. The velocity contrast at the shaft-soil interface allows wave reflections that the UFWI algorithm can exploit to accurately delineate boundaries. Defects were modeled with a reduced Vp of 3,000 m/s to represent anomalies such as segregated zones, or weak concrete commonly observed in field conditions.

3.2.1Test configuration and analyses

The data acquisition geometry follows standard CSL specifications, employing 4 to 8 access tubes, uniformly positioned about one foot inside the shaft boundary. For example, in the 8-tube configuration illustrated in **Figure 3.2**, the first source is placed in tube 1, while the remaining tubes serve as receivers. The source is then sequentially moved to each subsequent tube, yielding a total of 8 source positions, each with 7 corresponding receivers for a given source.

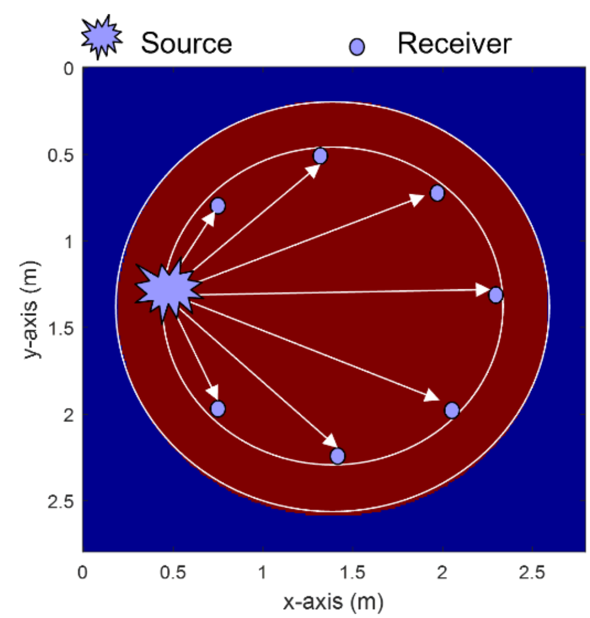

Figure 3.2 Acquisition geometry for synthetic experiments involving an 8-ft diameter drilled shaft.

To simulate wave propagation, each shaft diameter was modeled within a surrounding computational domain sized to ensure simulation accuracy and minimize boundary effects. For the 8-ft diameter shaft, a domain of 3.0 × 3.0 m (10 × 10 ft) was discretized into a 150 × 150 grid using 2 × 2 cm (0.8 in.) cells. The 6-ft diameter shaft used a 2.4 × 2.4 m (8 × 8 ft) domain with a 120 × 120 grid, while the 4-ft diameter shaft was modeled within a 1.6 × 1.6 m (5.3 × 5.3 ft) domain using an 80 × 80 grid—maintaining consistent cell resolution across all cases. Synthetic waveform data were generated using a Ricker wavelet source and served as input for the 2D UFWI, simulating realistic CSL datasets as if acquired under actual field conditions.

3.2.2Results of 8-ft diameter drilled shaft

The initial Vp model for inversion was defined as a homogeneous medium based on average travel times from a standard CSL analysis. For the 8-ft diameter shaft, a uniform Vp of 4000 m/s was assumed throughout a 3.0 × 3.0 m (10 × 10 ft) domain (**Figure 3.3**). The same initial velocity was used for the 6-ft and 4-ft diameter shafts, with domains of 2.4 × 2.4 m (8 × 8 ft) and 1.6 × 1.6 m (5.3 × 5.3 ft), respectively. The inversion used waveform data with frequency content primarily in the 4–15 kHz range. The inversion procedure was terminated under any of the following criteria: (1) reaching a maximum of 400 iterations, (2) failing to determine an optimal step length (no better model), or (3) attaining less than 0.1% improvement in the least-squares misfit over 20 consecutive iterations. The computational time for each inversion run was 15 to 30 minutes depending on shaft diameters, on a desktop computer (3.70 GHz, 8 cores, 64 GB RAM).

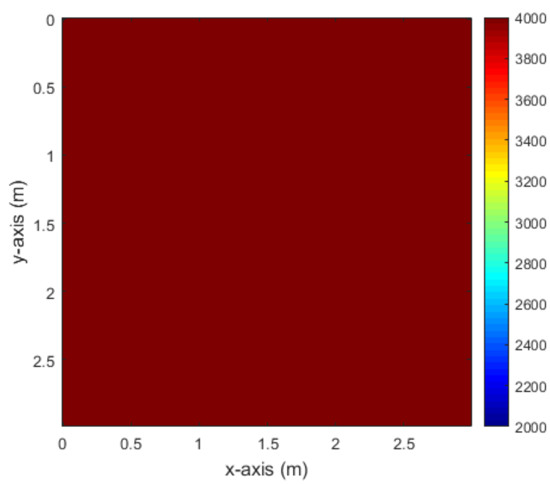

Figure 3.3 Initial Vp model for 8-ft diameter drilled shaft

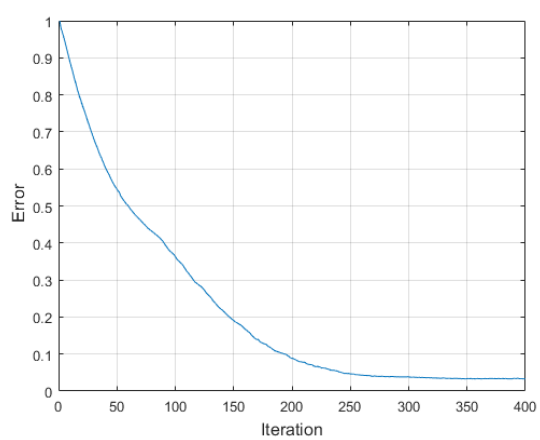

Figure 3.4 Normalized least-squares error as a function of inversion iteration number.

For the 8-ft diameter shaft with 8 access tubes, **Figure 3.4**illustrates the normalized least-squares error decreasing significantly from 1.0 at the initial iteration to approximately 0.03 at the final iteration. **Figure 3.5**compares the observed waveforms with those modeled using both the initial and final inverted velocity models. The results show substantial improvement in waveform alignment, culminating in near-perfect agreement between the observed and final modeled data. The final residuals approach zero across all receiver pairs (**Figure 3.5**d). For clarity, residual traces in **Figure 3.5**c, d are amplified by a factor of 10 for better view.

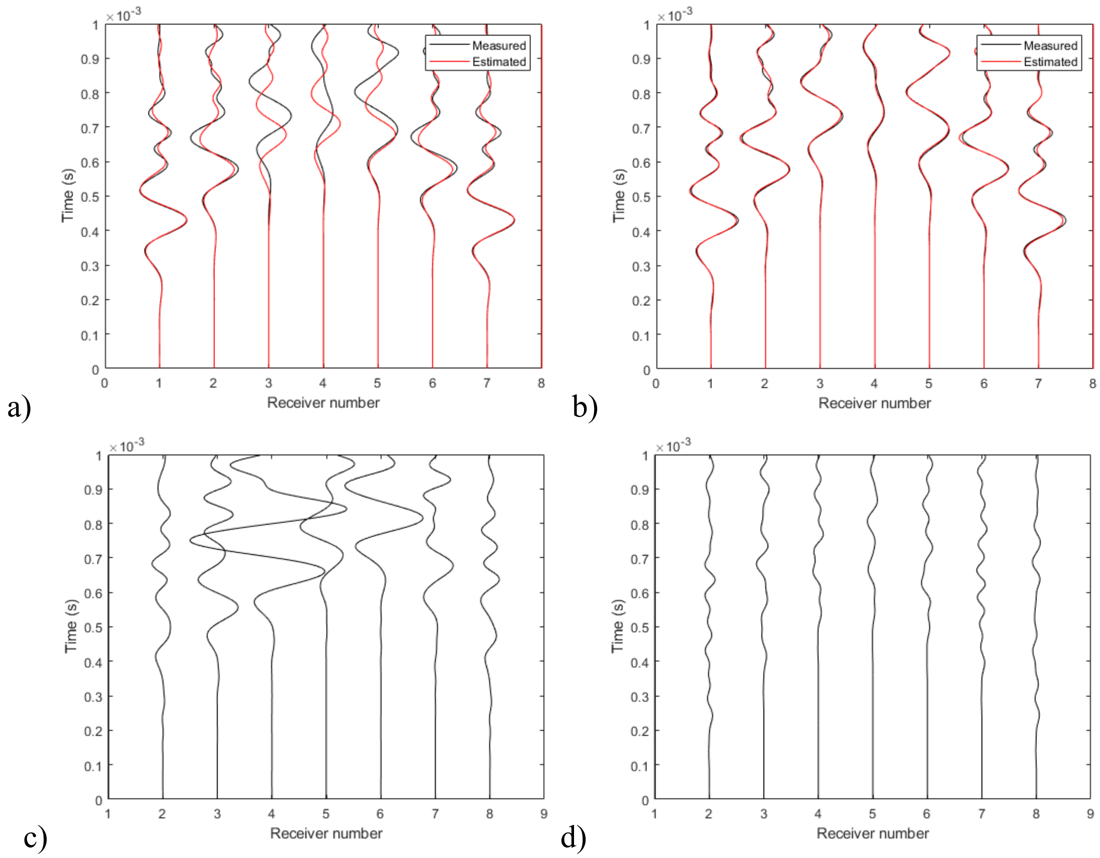

Figure 3.5 The 8-ft diameter shaft with internal defect: waveform comparison using 8 access tubes: (a) observed vs. initial model, (b) observed vs. final model, (c) residual (initial model), (d) residual (final model). Residuals in (c) and (d) are scaled ×10 for visualization.

Figure 3.6 shows the final inverted P-wave velocity (Vp) model for the 8-ft diameter shaft containing an internal defect. The inversion successfully reconstructs the overall shaft geometry, clearly delineating its boundaries and identifying the internal defect as a distinct low-velocity zone. Vp values decrease markedly from the initial 4,000 m/s within the shaft to approximately 2,000 m/s in the surrounding soil. The inverted boundary (solid black line), defined by a sharp velocity gradient, closely matches the true shaft boundary (dashed blue line).

Some ring-like artifacts appear beyond the shaft boundary because of regularization. While regularization helps suppress noise and stabilize the inversion, its formulation enforces spatial continuity by linking each cell to its four immediate neighbors (top, bottom, left, and right), resulting in smoother velocity transitions. Despite this, the UFWI method accurately reconstructs the entire shaft cross-section without requiring prior information such as estimated or design diameter, highlighting its novelty and robustness for defect imaging in drilled shafts.

Figure 3.7 presents the inverted P-wave velocity distributions for the 8-ft diameter drilled shaft with an internal defect, using configurations with 7, 6, 5, and 4 access tubes. In each subfigure, blue dashed lines denote the true shaft boundary and defect contour, while the black solid line indicates the boundary estimated through the FWI procedure. With seven tubes (**Figure 3.7**a), the inversion closely matches both the true shaft perimeter and defect geometry, accurately capturing the defect's size and location. Using six tubes (**Figure 3.7**b), the defect remains detectable, though it appears smoother and wider the ground truth. Reduced ray coverage slightly overestimates the defect's extent and introduces minor artifacts, especially along the shaft perimeter opposite the defect. With five tubes (**Figure 3.7**c), the defect is still identifiable but becomes distorted and underestimated by roughly 30%. The inferred shaft boundary shows irregularities, including localized flattening and inward offsets, and peripheral artifacts become more pronounced, suggesting that five tubes provide only marginal reliability. In the four-tube configuration (**Figure 3.7**d), the inversion fails to resolve the defect meaningfully. The inclusion appears only as a faint velocity anomaly, while the outer boundary is distorted and misaligned, effectively obscuring the defect. This result demonstrates that four tubes do not provide sufficient angular coverage to reliably image internal defects of this scale.

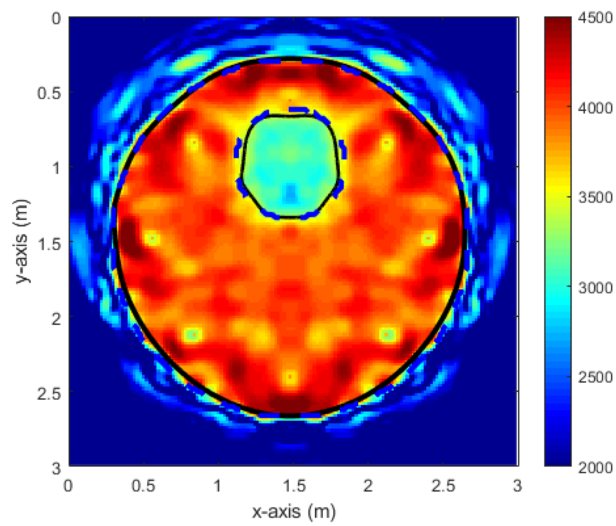

Figure 3.6 The 8-ft diameter shaft with internal defect: inversion result with 8 access tubes. The blue dashed line indicates the true shaft and defect boundaries, while the black line represents the inferred boundary from inversion.

Overall, the results demonstrate that increasing the access tube density enhances the algorithm's ability to resolve both shaft geometry and internal defects. For the 8-ft diameter shaft, a minimum of five access tubes is required to detect defects and delineate external boundaries. However, using more tubes (up to eight) is recommended for accurate and reliable defect characterization.

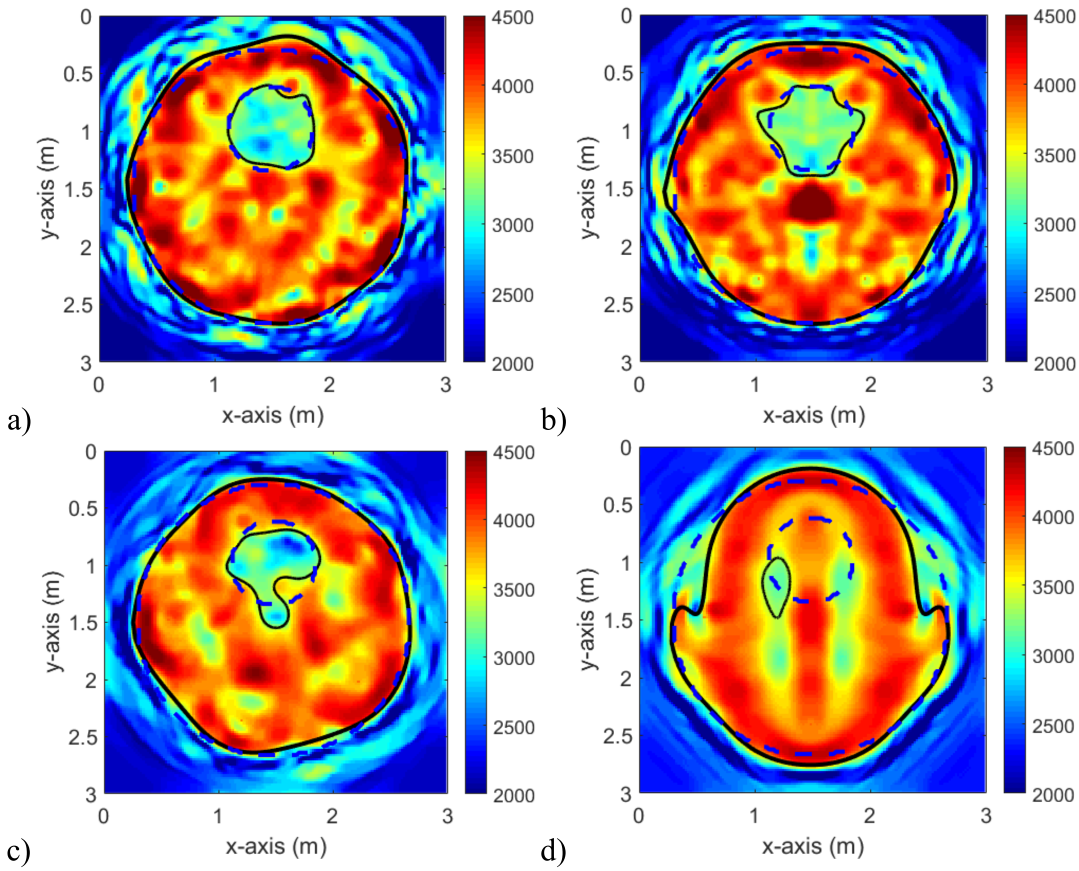

Figure 3.7 The 8-ft diameter shaft with internal defect: inversion results using varying numbers of access tubes: (a) 7 tubes, (b) 6 tubes, (c) 5 tubes, and (d) 4 tubes. The blue dashed line denotes the true shaft and defect boundaries; the black line indicates the inferred boundary from inversion.

3.2.3Results of 6-ft diameter drilled shaft

For the 6-ft diameter shaft with an internal defect, the same inversion procedure was applied using configurations with 8 to 4 access tubes. With 8 access tubes, **Figure 3.8** shows a significant reduction in the normalized least-squares error, from 1.0 at the initial iteration to approximately 0.03 at the final iteration. **Figure 3.9**compares the observed waveforms with those modeled using both the initial and final velocity models. The inversion process substantially improved waveform alignment, resulting in near-perfect agreement between the observed and final synthetic data, with residuals approaching zero across all channels.

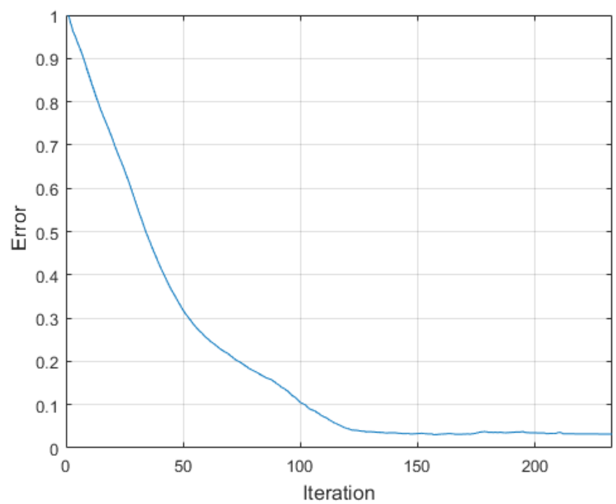

Figure 3.8 Normalized least-squares error versus inversion iteration number.

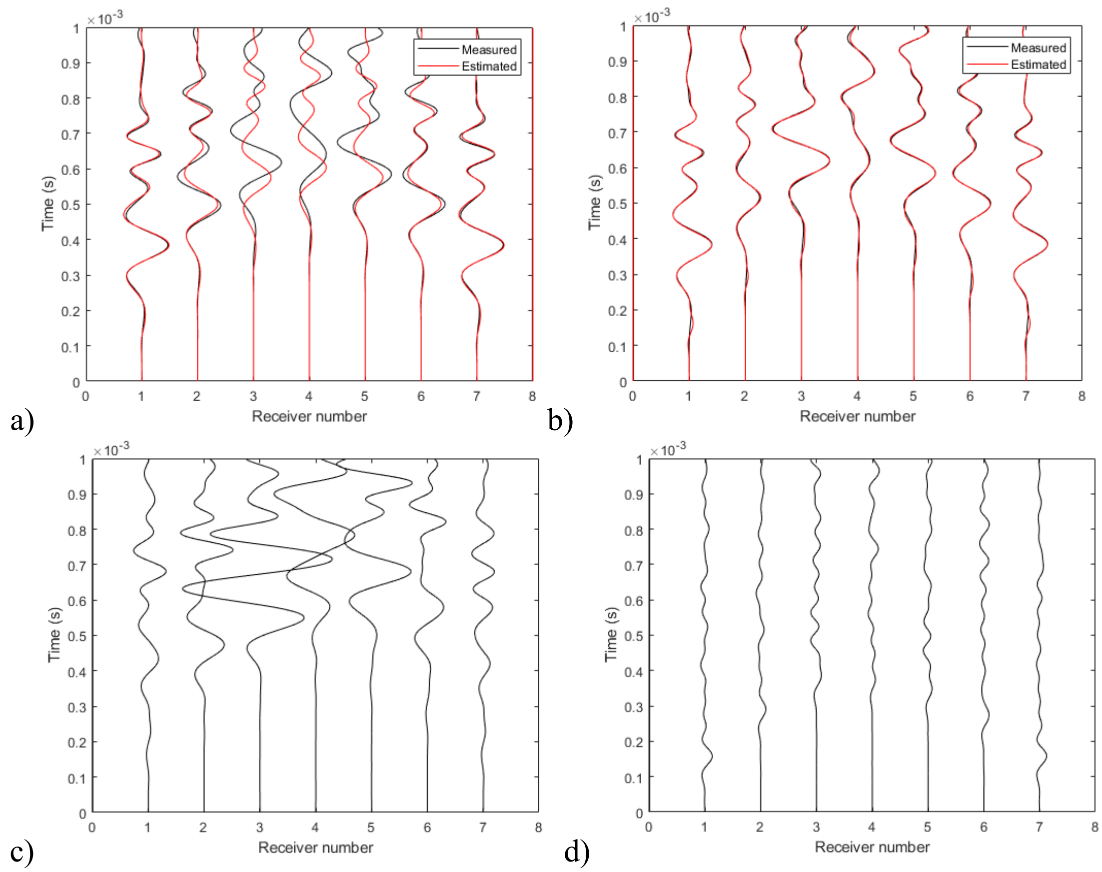

Figure 3.9 The 6-ft diameter shaft with internal defect: waveform comparison with 8 access tubes: (a) observed vs. initial model, (b) observed vs. final model, (c) residual (initial model), (d) residual (final model). Residuals in (c) and (d) are scaled 10 times for visualization.

Figure 3.10 presents the inverted P-wave velocity model for the 6-ft diameter shaft using 8 access tubes. As expected, the inversion accurately reconstructs the overall shaft geometry, clearly delineates the boundaries, and identifies the internal defect as a localized low-velocity zone. Again, both the defect and shaft boundary were resolved without relying on any prior geometric information, highlighting the robustness and effectiveness of the UFWI approach.

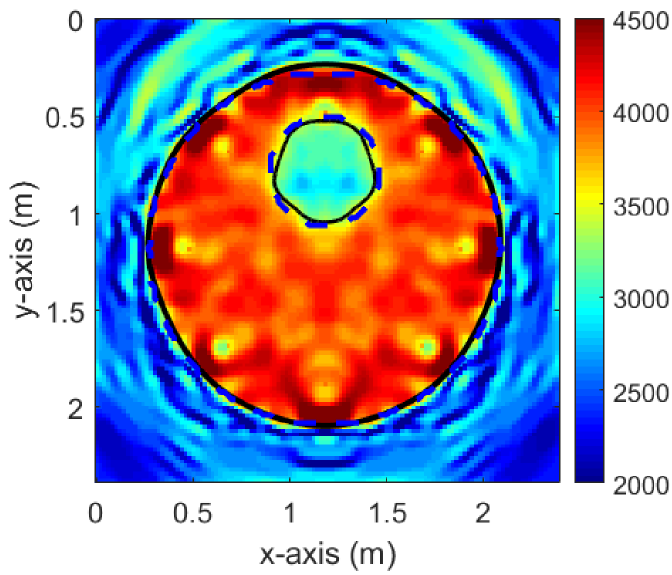

Figure 3.10 The 6-ft diameter shaft with internal defect: inversion result with 8 access tubes. Blue dashed line is the actual shaft and defect boundaries, and black line is inferred boundaries.

Figure 3.11 compares the inversion results for the 6-ft diameter shaft using four different access tube configurations: 7, 6, 5, and 4 tubes (panels a–d, respectively). In each panel, blue dashed curves indicate the true shaft perimeter and defect outline, while the black curve shows the boundary estimated by the inversion. With seven tubes (**Figure 3.11**a), the coverage is sufficient for excellent reconstruction of both the shaft boundary and the internal defect. The inferred perimeter closely matches the true boundary, and the defect is sharply resolved in both size and location. With six tubes (Figure 3.11b), the inversion remains effective. The defect is still clearly identified, though its edges appear slightly smoother, and minor artifacts emerge on the side opposite the anomaly. While the reconstructed indentation is less sharply defined than with seven tubes, the defect's presence and approximate size are accurately captured. With five tubes (Figure 3.11c), resolution noticeably decreases. The defect remains detectable but is underestimated in size, and the shaft boundary becomes less precise. In the four-tube configuration (Figure 3.11d), the inversion fails to meaningfully resolve the internal defect. The result is overly smoothed, and the anomaly appears only as a faint velocity perturbation without a distinct outline. This confirms that four tubes do not provide adequate angular coverage for reliable integrity assessment.

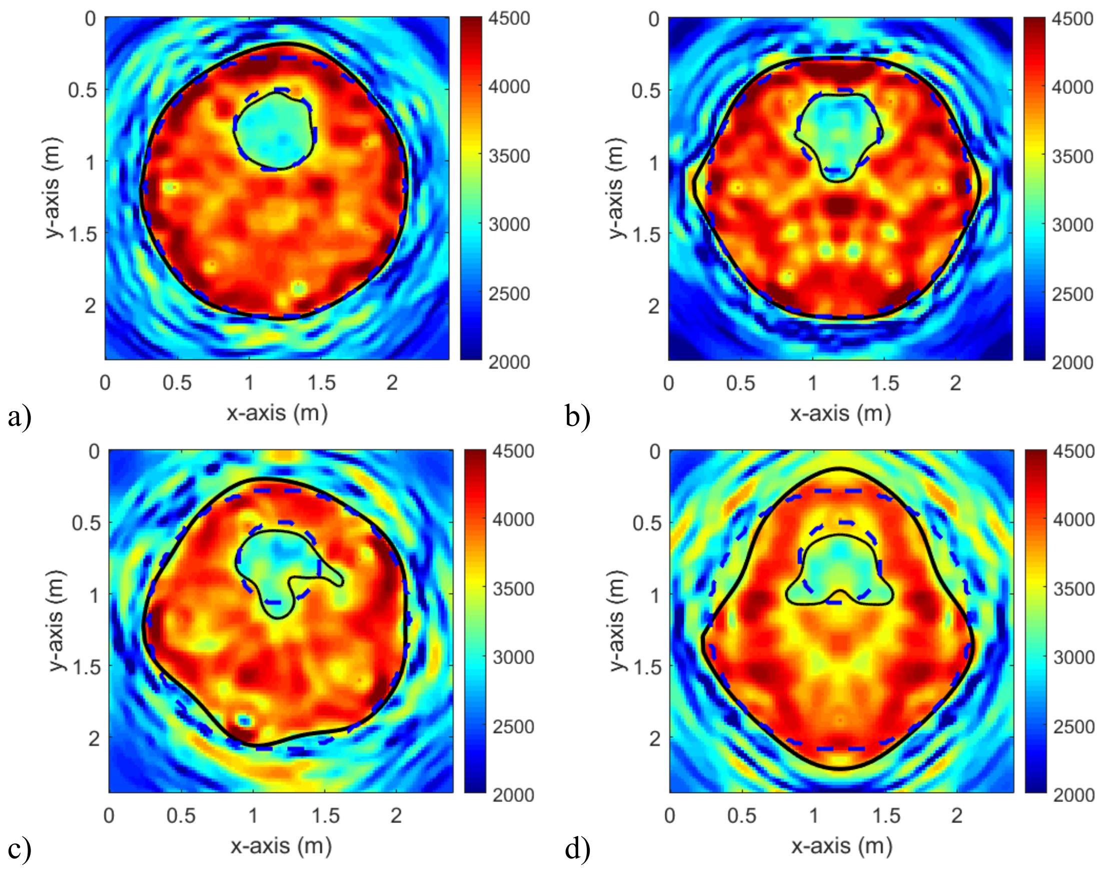

Figure 3.11 The 6-ft diameter shaft with internal defect: inversion results with various numbers of access tubes**:** (a) 7 tubes, (b) 6 tubes, (c) 5 tubes, and (d) 4 tubes. The blue dashed line denotes the true shaft and defect boundaries, while the black line indicates the inferred boundary from inversion.

Overall, the results indicate that a minimum of five tubes is necessary for imaging 6-ft diameter shafts. However, to ensure accurate and consistent defect characterization, the use of six tubes is recommended.

3.2.4 **Results of 4-ft diameter drilled shaft**

For the 4-ft diameter shaft with an internal defect, the UFWI algorithm was tested across configurations with a decreasing number of access tubes, from 8 down to 4. With 8 access tubes, Figure 3.12 shows the normalized least-squares error decreasing from 1.0 at the initial iteration to approximately 0.08 at the final iteration. Figure 3.13 compares observed and modeled waveforms for the initial and final velocity models. Waveform fits improve dramatically throughout the inversion process, with the final synthetic waveforms closely aligning with the observed data. The final residuals (Figure 3.13d) are much smaller than the initial residuals (Figure 3.13c).

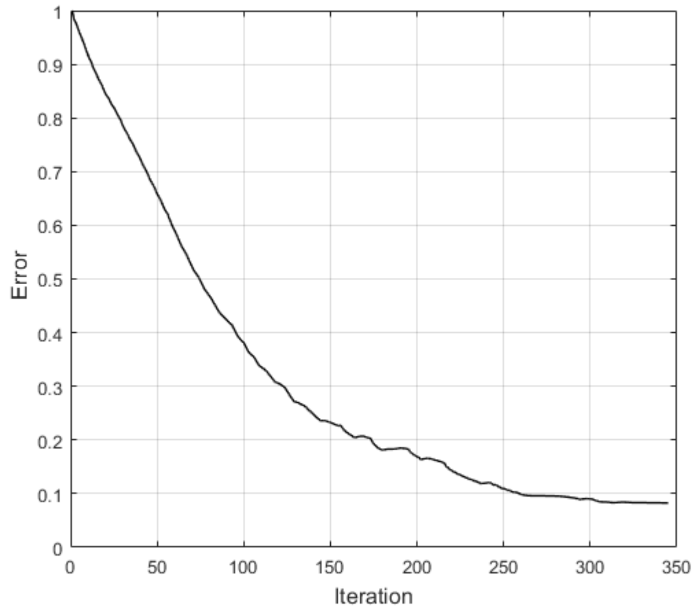

Figure 3.12 Normalized least-squares error versus the inversion iteration number.

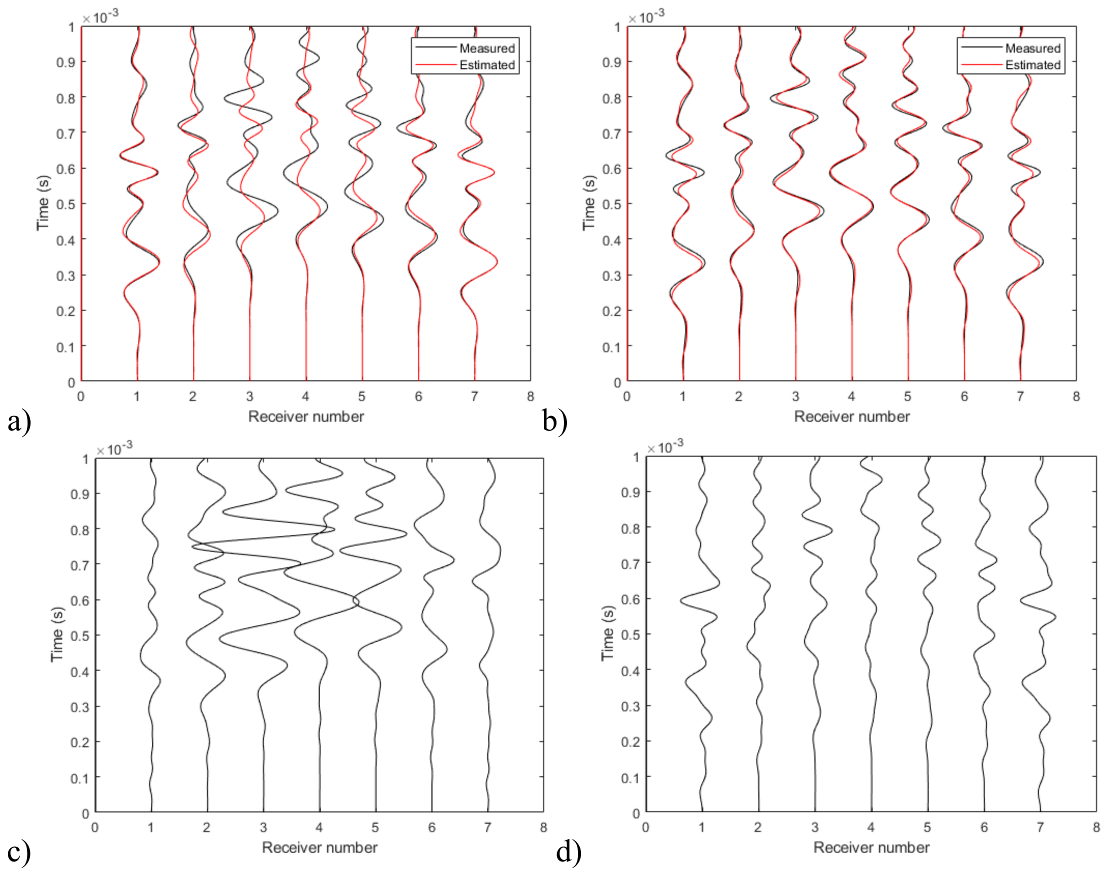

Figure 3.13 The 4-ft diameter shaft with internal defect: waveform comparison using 8 access tubes: (a) observed vs. initial model, (b) observed vs. final model, (c) residual (initial model), (d) residual (final model). Residuals in (c) and (d) are scaled 10 times for visualization.

The inverted P-wave velocity model for the 4-ft diameter shaft is shown in Figure 3.14. As expected, the inversion successfully recovers both the shaft boundary and the internal defect with high fidelity. The inferred boundary (black contour) closely aligns with the true shaft perimeter, demonstrating precise delineation of the shaft geometry. The internal defect is clearly characterized, with its location and size accurately captured.

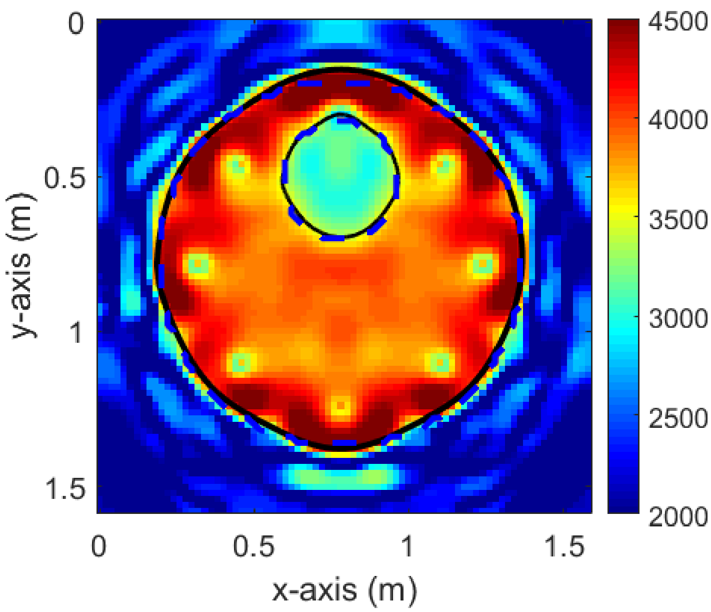

Figure 3.14 The 4-ft diameter shaft with internal defect: inversion result with 8 access tubes. The blue dashed line denotes the true shaft and defect boundaries, while the black line indicates the inferred boundary from inversion.

Similarly, **Figure 3.15** presents the inversion results for the 4-ft diameter shaft with an internal defect using configurations of 7, 6, 5, and 4 access tubes. In each panel, blue dashed curves indicate the true shaft and defect boundaries, while the black curves show the boundaries recovered by the inversion. With seven (**Figure 3.15**a), six (**Figure 3.15**b), and five (**Figure 3.15**c) tubes, the algorithm accurately characterizes both the defect and the shaft boundary, demonstrating robust performance across these configurations. However, with only four tubes (Figure 3.15d), the inversion fails to adequately resolve the internal defect and the shaft boundary, resulting in significant loss of detail and accuracy. Based on these findings, a minimum of five access tubes is recommended for reliable imaging of 4-ft diameter shafts.

In summary, the inversion algorithm demonstrated strong performance when adequate tube coverage was provided, effectively identifying internal defects and delineating shaft boundaries. Based on the analysis, it is recommended that a minimum of five access tubes be installed to enable reliable imaging of drilled shafts, regardless of shaft diameter. For shafts with diameters of 6 feet or greater, one tube per foot of shaft diameter is recommended. This enhanced coverage significantly improves the accuracy of defect detection and boundary resolution.

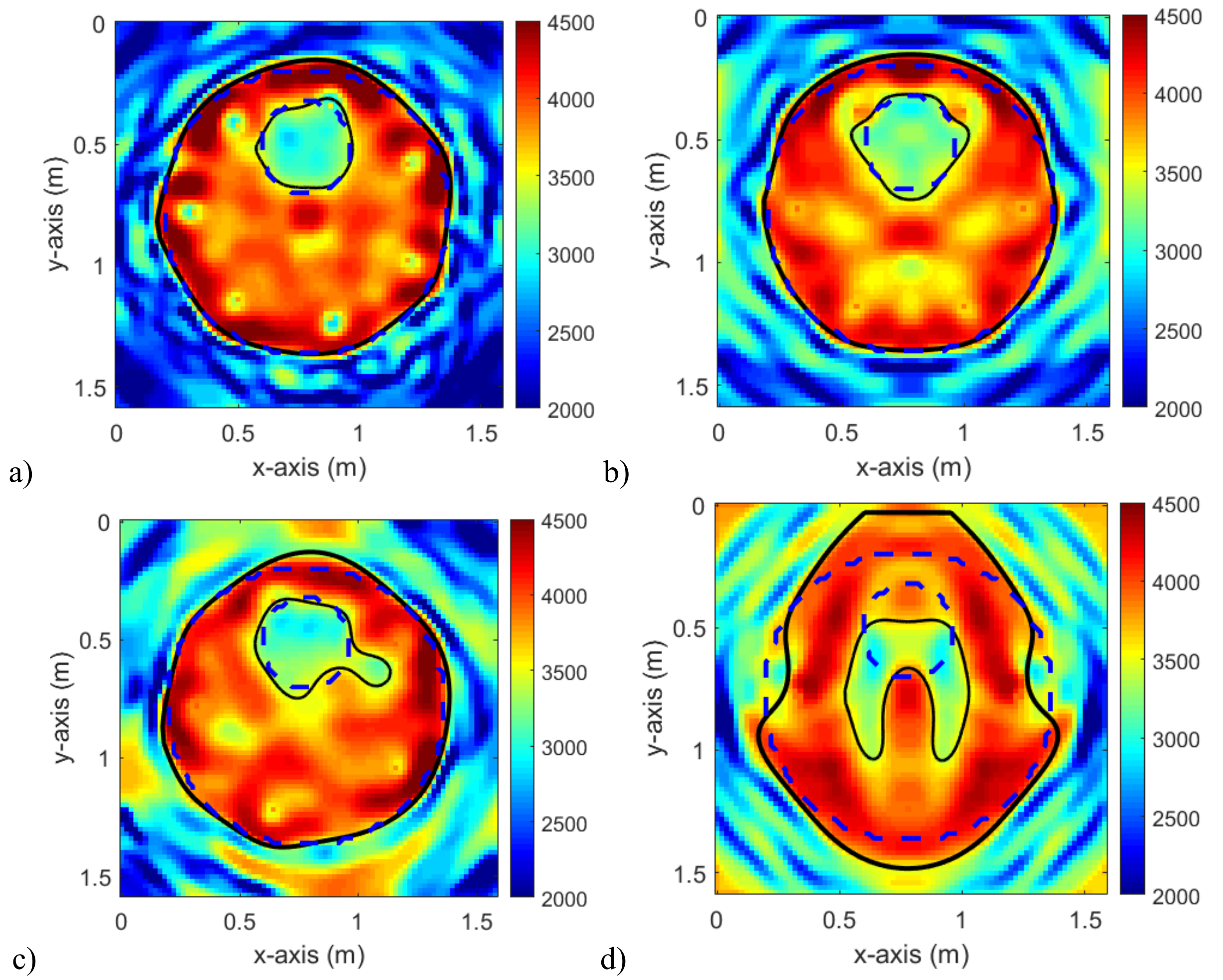

Figure 3.15 Inversion results for the 4-ft diameter drilled shaft with an internal defect using varying numbers of access tubes**:** (a) 7 access tubes, (b) 6 access tubes, (c) 5 access tubes, (d) 4 access tubes. Blue dashed line: actual shaft boundary and defect boundary; Black line: inferred boundary

3.3 **Synthetic experiments on shafts with external defects**

The algorithm was subsequently tested on drilled shafts containing external defects, which commonly occur in shaft construction due to soil caving within boreholes or incomplete concrete flow through the rebar cage. To evaluate this scenario, three synthetic models were created, representing shafts with external defects and diameters of 8 ft (2.4 m), 6 ft (1.8 m), and 4 ft (1.2 m) (Figure 3.16a–c). Each model incorporates a boundary flaw simulating a soil inclusion adjacent to the shaft perimeter. P-wave velocities were assigned as 4,000 m/s for intact concrete and 2,000 m/s for the surrounding soil.

3.3.1 **Test configuration and setup**

The test configuration and data simulation followed the same procedure described in Section 0. Access tube layouts varied from 8 down to 4 tubes, arranged uniformly around the shaft circumference to ensure consistent angular coverage, as illustrated previously in Figure 3.2.

Synthetic ultrasonic waveforms were generated for each configuration to simulate realistic field data under controlled conditions. These datasets served as inputs for the UFWI analysis detailed in the following sections, enabling systematic evaluation of the algorithm's performance across different sensor densities and shaft sizes.

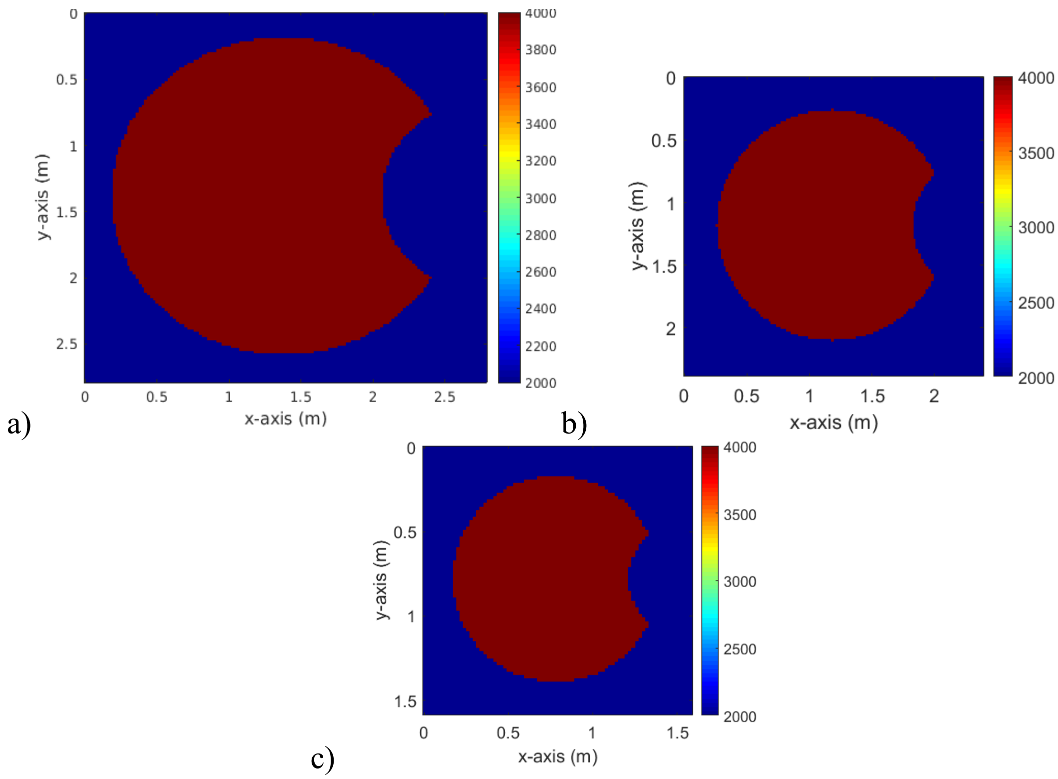

Figure 3.16 True model used for generating synthetic data: a) 8-ft diameter shaft, b) 6-ft diameter shaft, c) 4-ft diameter shaft.

3.3.2 **Results of 8-ft diameter drilled shaft**

The UFWI analyses were conducted following the same approach as in the previous cases, starting from homogeneous initial models with a uniform P-wave velocity (Vp) of 4,000 m/s across the entire domain. The inversion employed identical stopping criteria to ensure consistency. Waveform data within the frequency range of 4–15 kHz was used, capturing the essential frequency components for accurate velocity reconstruction. Depending on the shaft diameter and model complexity, each inversion run required between 15 and 30 minutes of computational time on a desktop computer equipped with a 3.70 GHz processor, 8 cores, and 64 GB of RAM. This computational efficiency demonstrates the method's practical feasibility for field applications.

Figure 3.17 illustrates the progression of the error function over the course of the inversion iterations. The normalized error decreases significantly from 1.0 at the initial iteration to 0.06 at the final iteration, indicating strong convergence.

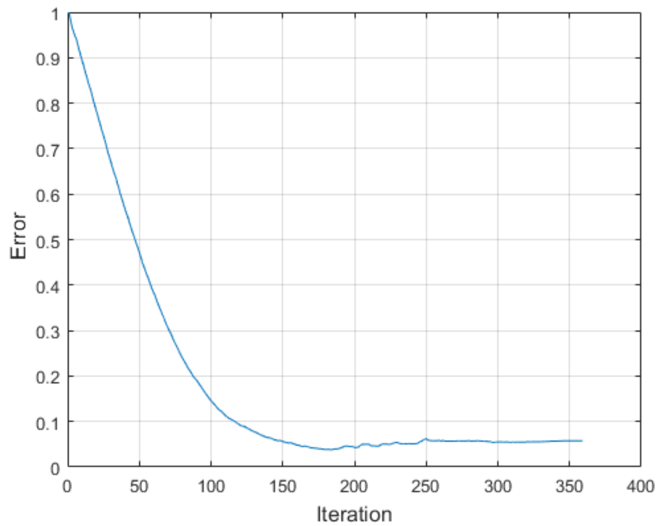

Figure 3.17 Normalized least-squares error versus the inversion iteration number.

Figure 3.18 compares the observed (measured) and modeled waveforms, highlighting substantial improvement in data fitting from the initial model (Figure 3.18a) to the final inverted model (Figure 3.18b). Correspondingly, the residuals shown in Figure 3.18c and 18d are greatly reduced, demonstrating the inversion's effectiveness in accurately reproducing the measured waveforms.

The inverted P-wave velocity model is shown in Figure 3.19. The analysis successfully reconstructs the overall geometry of the shaft, clearly delineates its boundaries, and accurately identifies the external defect. The inferred boundary, indicated by the black line, closely matches the true boundary outlined by the blue dashed line, including the location and extent of the defect. Notably, these features are resolved without relying on any prior information about shaft dimensions or defective location, underscoring the robustness and novelty of the UFWI method.

Similarly, Figure 3.20 presents the inverted P-wave velocity distributions for the 8-ft diameter shaft with an external defect, using configurations with 7 to 4 access tubes. With seven tubes (Figure 3.20a), the inversion result is highly accurate—the inferred boundary closely matches the true necked shape, successfully capturing the defect. Using six tubes (Figure 3.20b) and five tubes (Figure 3.20c), the results remain acceptable; however, some details of the defect are lost. The necked region is oversimplified, appearing as a straight boundary segment rather than a localized constriction. With only four tubes (Figure 3.20d), the inversion fails to resolve the external defect. The inferred boundary appears nearly circular, completely masking the necked region and misrepresenting the shaft geometry.

In summary, for 8-ft diameter shafts with external defects, a minimum of five access tubes is necessary to capture the general boundary shape. However, for accurate and detailed imaging of the shaft and defect geometry, the use of seven or eight tubes is strongly recommended.

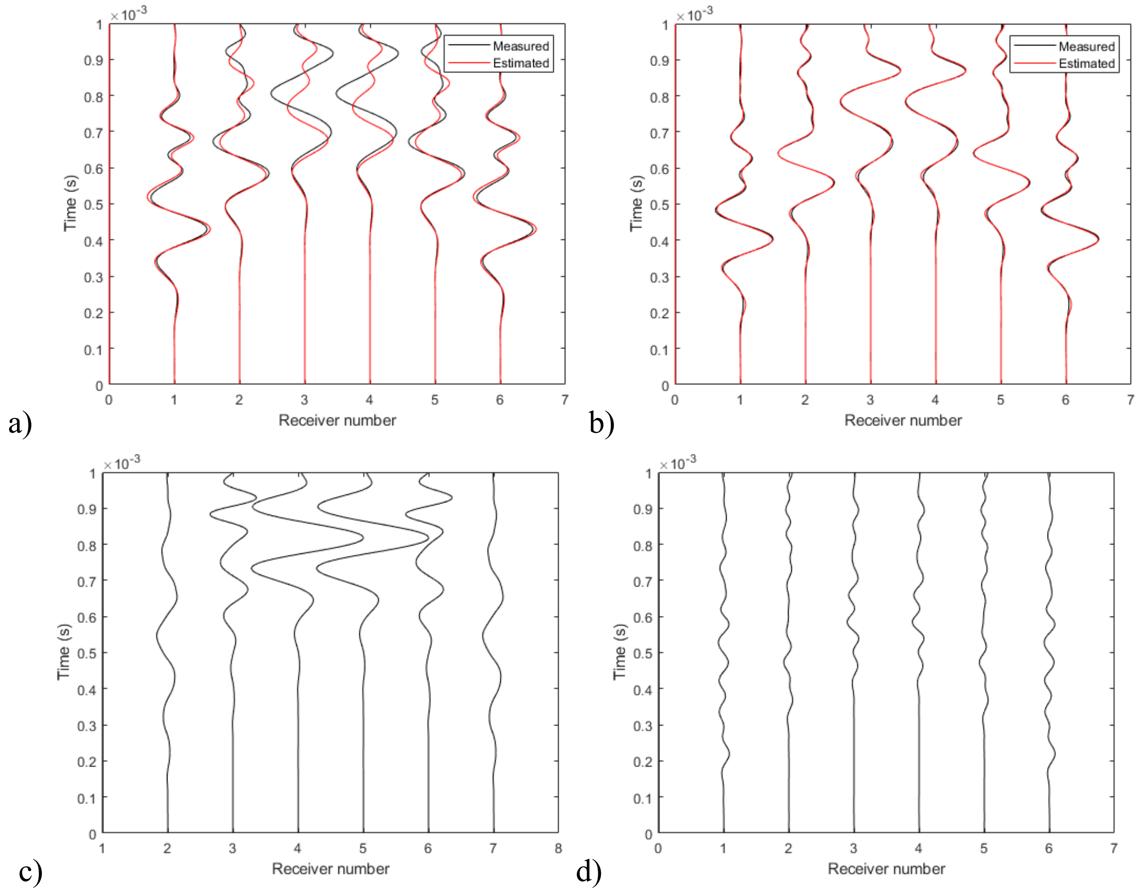

Figure 3.18 The 8-ft diameter shaft with external defect: waveform comparison using 8 access tubes**:** a) observed data and estimated data associated with the initial model, b) observed data and estimated data associated with the final inverted model, c) residual associated with the initial model, and d) residual associated with final inverted model. Both residuals in figures c and d are scaled by a factor of 10 for better visualization.

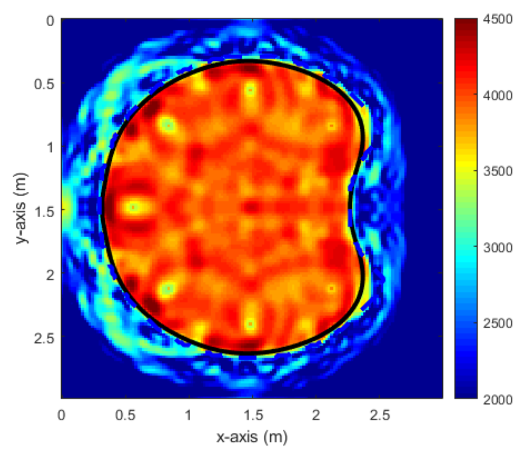

Figure 3.19 The 8-ft diameter shaft with external defect: inversion result with 8 access tubes. The blue dashed line denotes the true shaft and defect boundaries, while the black line indicates the inferred boundary from inversion.

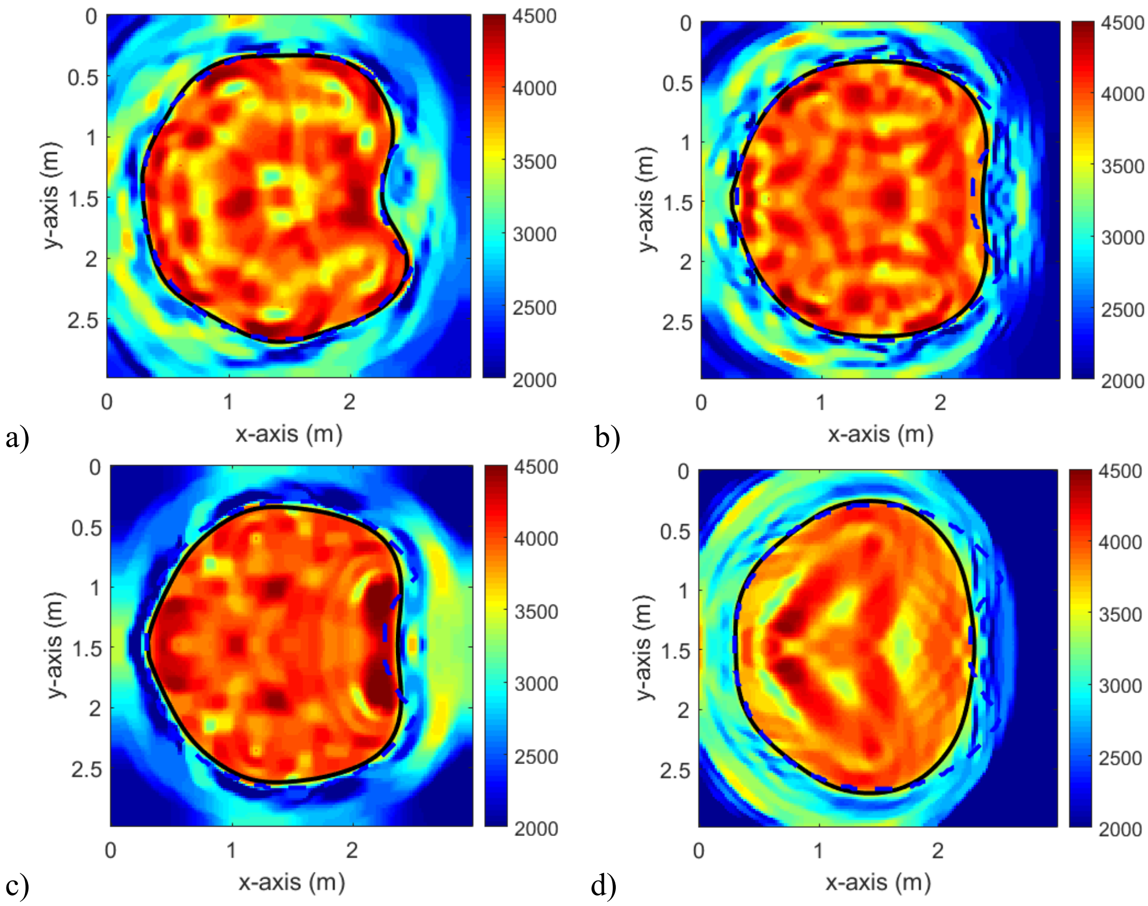

Figure 3.20 The 8-ft diameter shaft with external defect: inversion results with different numbers of access tubes**:** (a) 7 tubes, (b) 6 tubes, (c) 5 tubes, and (d) 4 tubes. The blue dashed line represents the true shaft boundary, while the black line indicates the inferred boundary from inversion.

3.3.3 **Results of 6-ft diameter drilled shaft**

As with the previous case, the UFWI algorithm was tested on a 6-ft diameter drilled shaft containing an external defect (Figure 3.21a), using multiple test configurations with varying numbers of access tubes. The inversion results are presented in Figure 3.21b through Figure 3.21f, corresponding to configurations with 8 to 4 tubes, respectively.

With 8 tubes (Figure 3.21b) and 7 tubes (Figure 3.21c), the inversion accurately reconstructs the shaft geometry and clearly delineates the external defect. The inferred boundaries closely match the true shaft perimeter, including the localized necking associated with the defect. With 6 tubes (Figure 3.21d) and 5 tubes (Figure 3.21e), the results remain acceptable. While minor smoothing and simplification of the defect shape occurs, the general location and boundary deformation are still resolved with reasonable fidelity. However, with only 4 tubes (Figure 3.21f), the inversion fails to capture the external defect. The recovered boundary appears overly smoothed and nearly circular, concealing the presence of the necked region.

In summary, for 6-ft diameter shafts with external defects, a minimum of five access tubes is necessary to capture the general boundary shape and identify defect zones. For more accurate imaging and precise defect characterization, configurations with six or more tubes are recommended.

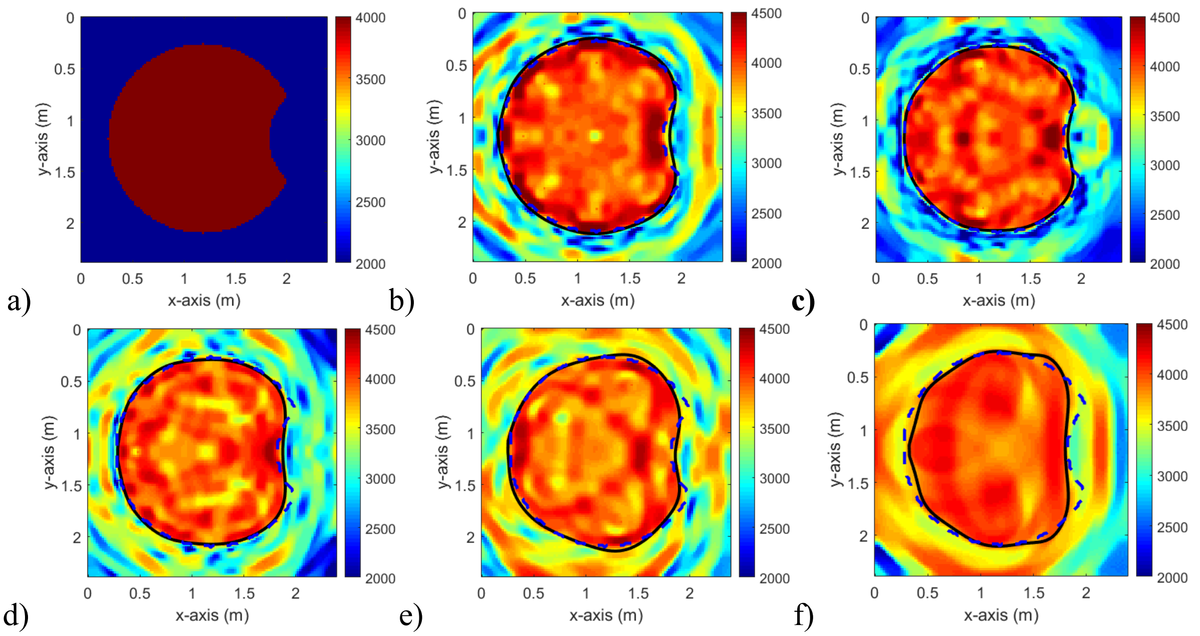

Figure 3.21 The 6-ft diameter drilled shaft with an external defect**:** a) true model, and inversion results using different numbers of access tubes: (b) 8 tubes, (c) 7 tubes, (d) 6 tubes, (e) 5 tubes, and (f) 4 tubes. The blue dashed line represents the true shaft boundary, while the black line indicates the inferred boundary from inversion.

3.3.4**Results of 4-ft diameter drilled shaft**

Lastly, the UFWI algorithm was applied to a 4-ft diameter drilled shaft containing an external defect (Figure 3.22a), using various test configurations to evaluate the impact of access tube count. The inversion results are presented in Figure 3.22b through Figure 3.22f, corresponding to configurations with 8 to 4 access tubes, respectively.

The results for configurations with 8 tubes (Figure 3.22b), 7 tubes (Figure 3.22c), 6 tubes (Figure 3.22d), and 5 tubes (Figure 3.22e) all show successful recovery of the shaft boundary and identification of the external defect. In these cases, the inversion accurately captures the necking region and preserves the overall shaft geometry, demonstrating the algorithm's robustness with adequate angular coverage.

However, with only 4 tubes (Figure 3.22f), the inversion fails to detect the external defect. The resulting velocity model presents a nearly idealized circular shaft boundary, with no clear indication of the necked region. The limited data coverage provided by four tubes is insufficient to resolve localized boundary anomalies, leading to an oversimplified and inaccurate reconstruction.

In summary, for 4-ft diameter drilled shafts with external defects, a minimum of five access tubes is required to achieve reliable imaging of the shaft boundary and detect defect features. To ensure accurate and detailed characterization, it is recommended that configurations include five or more tubes.

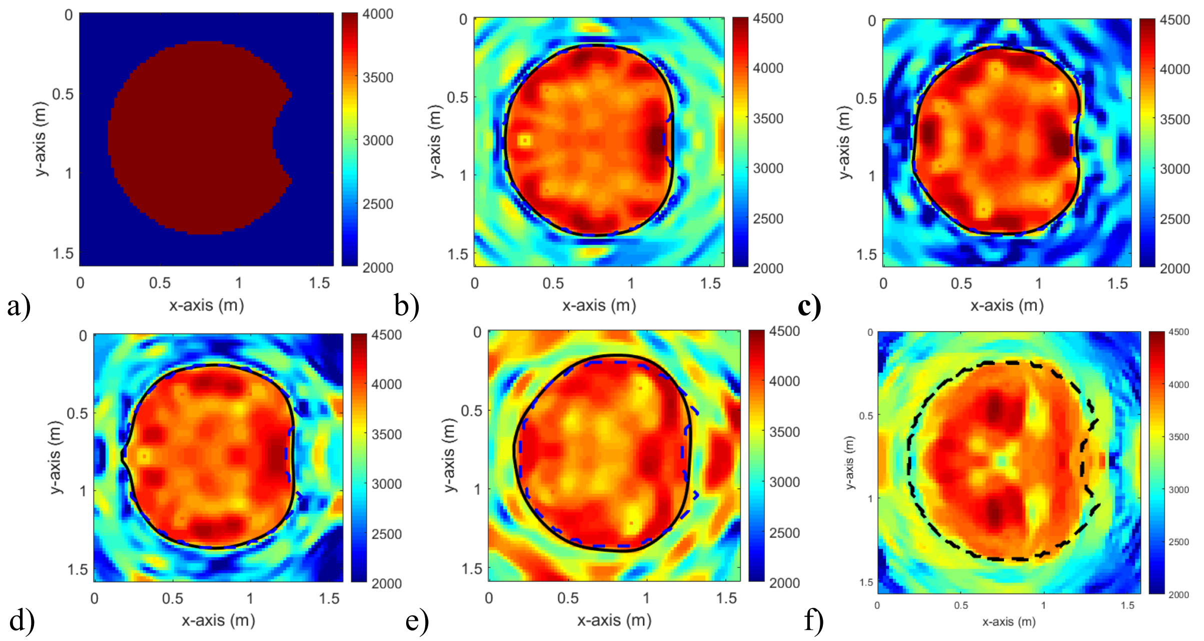

Figure 3.22 The 4-ft diameter drilled shaft with an external defect: a) true model, and inversion results using different numbers of access tubes: (b) 8 tubes, (c) 7 tubes, (d) 6 tubes, (e) 5 tubes, and (e) 4 tubes. The blue dashed line represents the true boundary, while the black line indicates the inferred boundary.

Chapter 4 - VERIFICATION OF 2D ULTRASONIC FWI ALGORITHM ON A DEFECTIVE DRILLED SHAFT (TASK 3)

4.1 Introduction

This chapter (Task 3) presents the field implementation and validation of the UFWI methodology developed in Tasks 1 and 2. The primary objective is to transition UFWI from synthetic and numerical studies to application under realistic field conditions, and to evaluate its capability for drilled shaft integrity imaging using full-scale test data. To achieve this, the work includes site characterization at the Hawthorne FDOT test pit, construction of a full-scale instrumented drilled shaft with intentionally embedded defects, acquisition of field measurements, and subsequent data processing and inversion.

As documented in previous chapters, Tasks 1 and 2 focused on the development and numerical evaluation of the UFWI algorithm for drilled shaft integrity assessment. These tasks systematically investigated imaging resolution and defect detectability across representative shaft geometries and controlled anomaly scenarios, including both internal defects (within or near the reinforcement cage) and external defects (outside the cage). The results established the expected sensitivity of UFWI to defect size, type, and location, and informed the design of the field test program, including shaft geometry, instrumentation layout, defect configuration, and data acquisition strategy.

The test shaft was constructed by Reliable Constructors, Inc. generally in accordance with standard FDOT drilled shaft construction practices, with controlled modifications introduced to simulate representative construction anomalies. Intentionally embedded defects include soil inclusion and necking, slurry inclusion, concrete segregation, and a soft-bottom condition. Detailed documentation of site stratigraphy, shaft construction, reinforcement placement, concreting operations, and defect implementation is provided to establish a ground-truth basis for evaluating UFWI results.

The shaft was instrumented to support both conventional nondestructive testing and supplementary monitoring during curing. Instrumentation included six CSL tubes, consistent with ASTM guidance of approximately one tube per foot of shaft diameter, and approximately 1,000 ft of fiber-optic cable installed in a continuous up-and-down loop along 24 vertical reinforcing bars for distributed temperature sensing. The fiber-optic installation is consistent with the general intent of ASTM D7949-25, Method C, which covers embedded fiber-optic cables attached to the reinforcing cage for thermal integrity testing of concrete deep foundations. In this project, the fiber-optic cable was attached to the reinforcement cage before placement and used primarily to obtain distributed temperature profiles during curing for research comparison with UFWI; therefore, the installation should be interpreted as a project-specific implementation of Method C rather than a stand-alone production thermal integrity test. These measurements provide complementary datasets for assessing shaft integrity and thermal behavior during curing, while also offering independent reference information for interpreting UFWI results.

A major effort is the processing and inversion of the acquired field data. The CSL measurements were reviewed, quality-controlled, and processed prior to inversion, and subsequently used within the UFWI workflow to reconstruct velocity images of the shaft cross-section. These results are used to evaluate the method’s ability to detect and localize known embedded defects under field conditions. This represents the first application of UFWI to full-scale measured data on shaft with defects and provides assessment of its practical applicability for drilled shaft integrity evaluation.

Overall, this chapter establishes the field validation framework for UFWI by integrating site characterization, test shaft construction, controlled defect implementation, instrumentation, data acquisition, processing, and inversion-based interpretation. The results enable direct comparison between reconstructed images and known as-built conditions and provide insight into the strengths and current limitations of UFWI for practical drilled shaft integrity assessment.

4.2 **Site investigation**

The construction site was at Hawthorne FDOT test pit. A soil boring was done to 50 ft depth as shown in **Figure 4.1**. The boring log shows a layered soil profile dominated by sands and silty sands in the upper 35 ft, underlain by highly plastic silt to the end of boring at 50 ft depth. Near the ground surface (about 0–2 ft), the soil consists of loose to medium dense dark gray fine sand with organics (SP–SM / A-3), suggesting surficial materials with some organic influence. From roughly 2 to 7 ft, the soil transitions to medium dense gray fine sand (SP–SM / A-3), indicating relatively clean granular material with moderate strength.

Between about 7 and 12 ft, the profile changes to medium dense gray clayey fine sand (SC / A-2-6), reflecting an increase in fines and some cohesive behavior. From approximately 12 to 20 ft, the material becomes loose to medium dense gray silty fine sand (SM / A-2-4), followed by medium dense dark gray silty fine sand between about 20 and 25 ft. These layers indicate variable density granular soils with moderate compressibility and strength, typical of alluvial or coastal deposits.

From about 25 to 30 ft, the soil remains loose to medium dense gray silty fine sand (SM), and from roughly 30 to 35 ft the sand becomes very loose to loose dark gray silty fine sand (SM / A-2-4). This interval represents the weakest granular zone in the profile and could be more susceptible to disturbance during drilling, as well as to settlement under load. Below this, from about 35 to 40 ft, the soil changes abruptly to soft gray highly plastic silt (MH / A-7-5), indicating a compressible, low-strength fine-grained layer.

In the continuation boring from about 40 to 50 ft, the highly plastic silt becomes very stiff to hard (MH / A-7-5), providing a much stronger bearing stratum compared to the softer silt above. Overall, the profile reflects alternating sandy and silty deposits overlying a deep, highly plastic silt layer, with strength increasing significantly below about 40 ft.

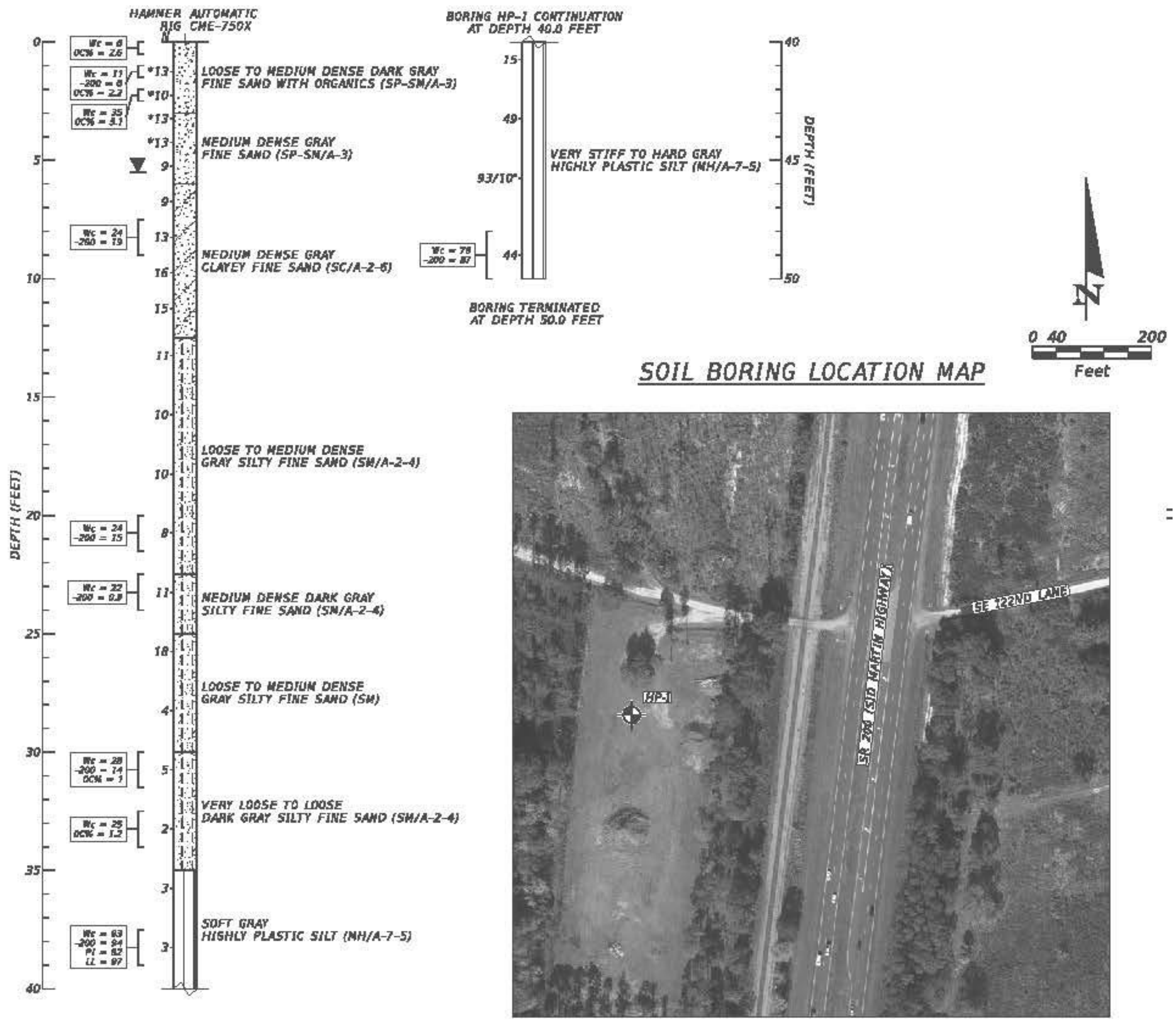

Figure 4.1 SPT boring near the shaft location.

4.3 **Construction of drilled shaft**

A new drilled shaft with a nominal diameter of 6 ft (72 inch) and a length of 40 ft was constructed to verify the effectiveness of the UFWI method and associated algorithms. Six access tubes were installed in accordance with the ASTM standard for CSL testing with one tube/foot of shaft diameter. Multiple representative defects were intentionally embedded both inside and outside the rebar cage to provide controlled "ground truth" for method validation. The targeted defect types include soil inclusions/necking, slurry inclusions, concrete segregation, and a soft-bottom condition. **Figure 4.2** presents a schematic overview of the defect layout and reinforcement/tube configuration; additional details are provided below.

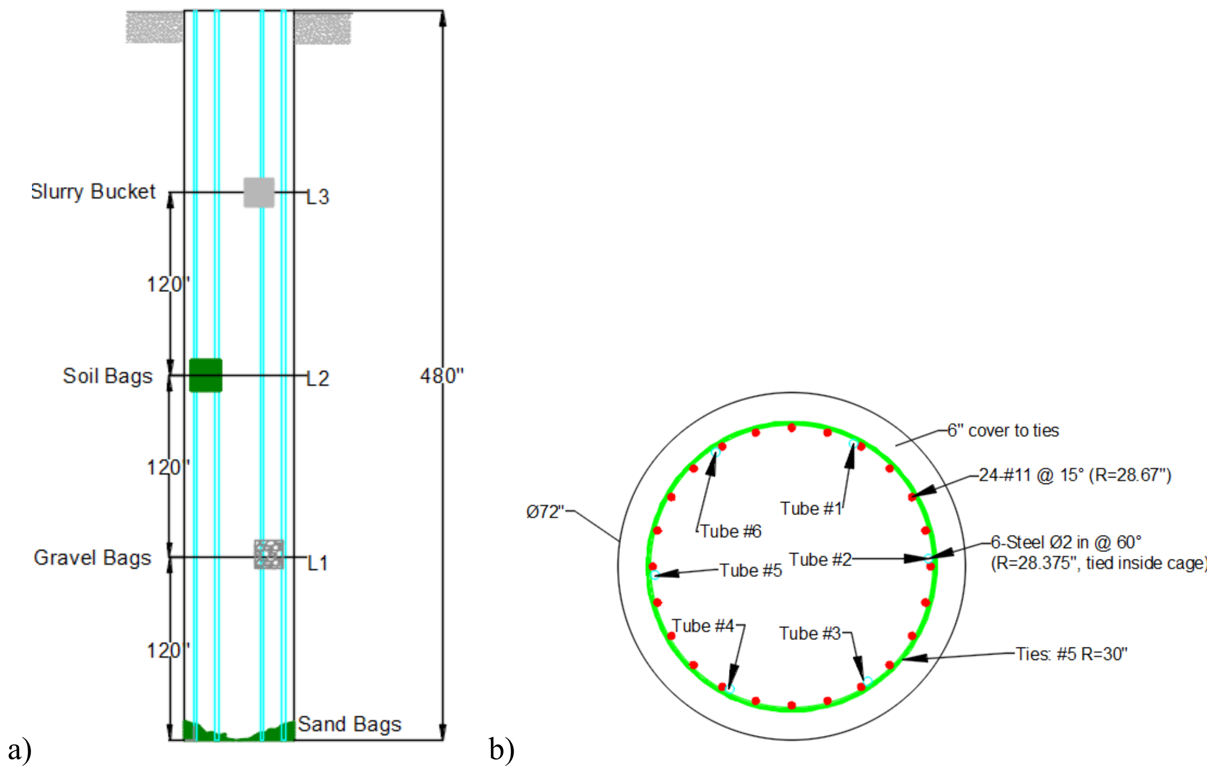

Figure 4.2 Test-shaft design and planned defect configuration for UFWI field validation**:** (a) elevation schematic of the Ø72-in., 40-ft drilled shaft showing defect levels L1–L3 at 10-ft spacing (gravel bags/segregation at L1, soil bags/necking at L2, slurry bucket at L3) and sandbags at the base to simulate a soft-bottom condition; (b) plan view (no defects shown) illustrating the reinforcement and CSL tube layout

4.3.1 **Fabrication of rebar cage and CSL tube assembly**

The reinforcement cage was fabricated in accordance with the draft design shown in **Figure 4.2**. **Figure 4.3** documents the completed reinforcement cage and CSL tube assembly prepared for the test shaft. The cage was prefabricated and transported to the site as a single unit (**Figure 4.3**a). An end view of the cage (**Figure 4.3**b) illustrates the reinforcement layout, including twenty-four #11 longitudinal bars restrained by #5 ties to maintain the required cage geometry and cover, as well as six CSL access tubes uniformly distributed around the perimeter and securely tied to the cage to maintain alignment during lifting and concreting. For consistency in documentation and subsequent UFWI/CSL interpretation, the tubes were labeled Tube #1 through Tube #6 and numbered clockwise (**Figure 4.3**b). The overall assembly provides the instrumentation and reinforcement framework required for CSL data collection and UFWI-based imaging while maintaining dimensional stability during handling and placement.

In addition, approximately 1,000 ft of fiber-optic cable was installed in a continuous up-and-down loop along 24 vertical reinforcing bars to enable distributed temperature sensing during concrete curing (**Figure 4.3**c). This installation is generally consistent with the embedded fiber optic cable concept described in ASTM D7949-25 Method C, although the continuous 24-

bar loop configuration was selected for research-level spatial coverage and comparison with UFWI results.

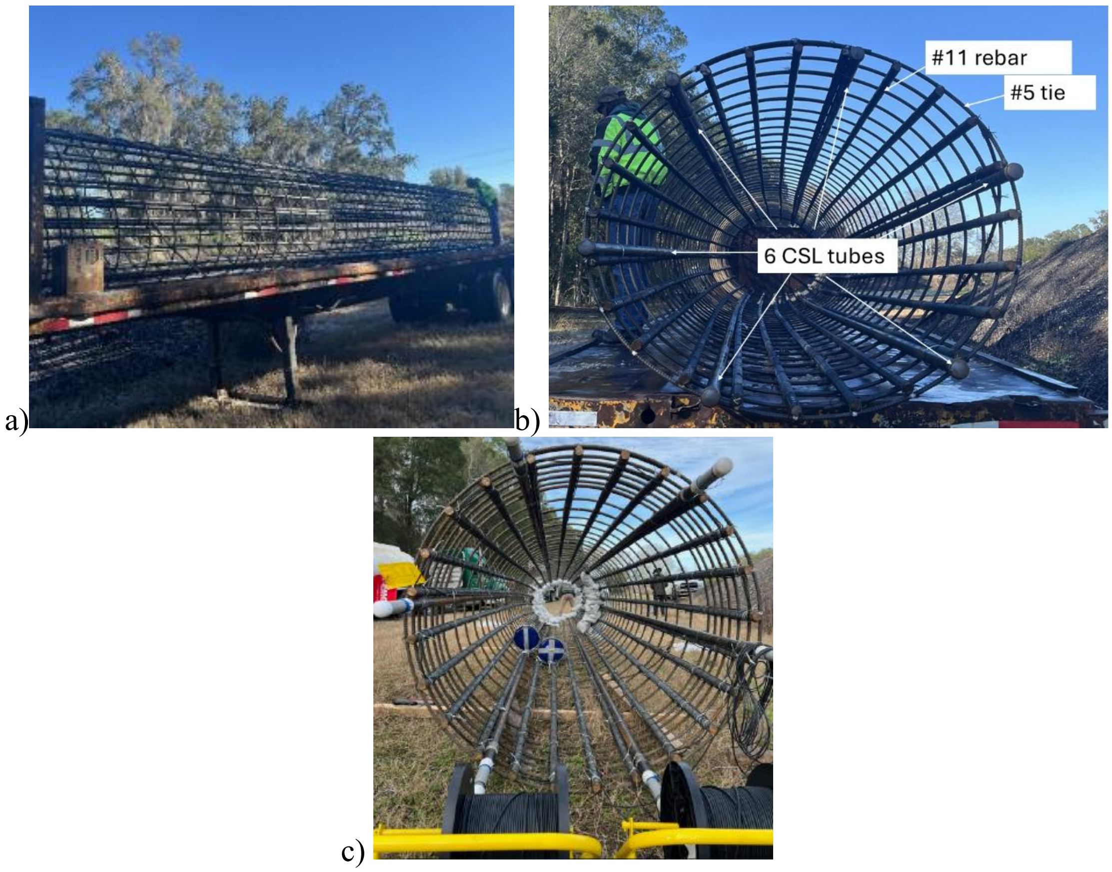

Figure 4.3 Reinforcement cage and CSL tube assembly for the test shaft**:** (a) completed rebar cage prior to installation, (b) end view identifying 24 longitudinal bars of #11 size and #5 ties, and six CSL tubes, and (c) end view showing fiber optic cables and instrumentation.

4.3.2**Fabrication of foundation defects**

The test shaft included three primary defect levels (L1–L3) spaced at 10-ft intervals along the shaft length, together with a soft bottom. The defect layouts were selected to challenge UFWI performance across a range of depths and azimuths and to represent conditions expected in practice, including anomalies located inside the cage, adjacent to the cage, and outside the cage near the shaft boundary, where boundary scattering and limited ray coverage may influence imaging resolution.

At level L1 (10 ft from the shaft bottom), a concrete segregation/aggregate-rich zone was simulated using gravel bags (same aggregate used in shaft concrete) placed adjacent to the reinforcement cage and centered between CSL Tube #1 and CSL Tube #6 (**Figure 4.4Error! Reference source not found.Error! Reference source not found.Error! Reference source not found.Error! Reference source not found.Error! Reference source not found.Error! Reference source not found.Error! Reference source not found.**). The plan-view schematic indicates an affected sector with an inner circumferential extent of ~45 in. and an outer circumferential extent of ~60 in., and the installed gravel-bag stack has an approximate longitudinal (vertical) extent of 1.4 ft (≈ 16.8 in.) along the cage. The maximum total gravel-bag radial thickness (from the shaft perimeter inward) is approximately 15 in.; the radial distance from the shaft outer perimeter to the tie line in this region is approximately 6 in. (same as cover thickness), indicating that the gravel-bag zone extends through the cover region and continues inward past the tie line by approximately 9 in. Using these dimensions and a trapezoidal approximation in plan-view, the corresponding defect envelope volume is about 13, 000 in^3, i.e., approximately 7.52 ft^3 (about 56.3 gal). This volume provides a repeatable target size for validation; the effective material contrast is governed by the as-installed gravel packing, bag deformation, and local concrete interaction during placement.

a) 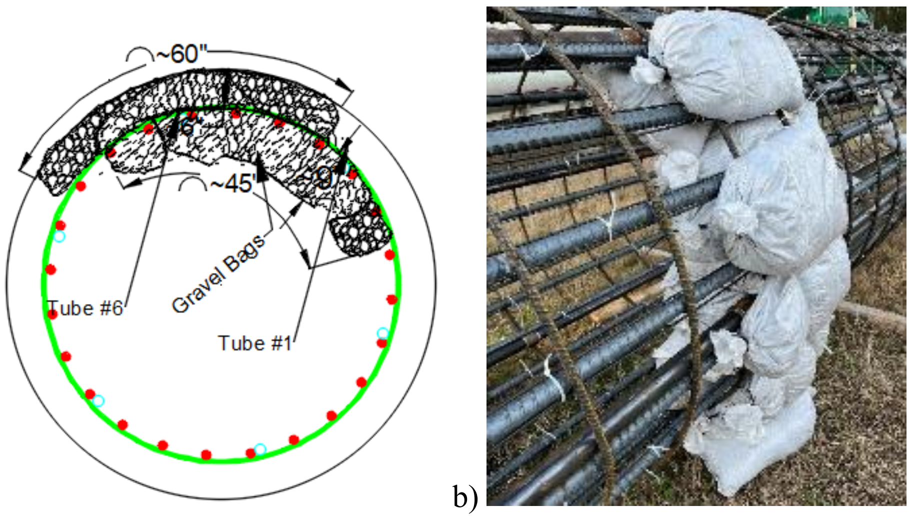 b)

Figure 4.4 Concrete segregation / aggregate-rich defect simulation using gravel bags: (a) plan-view schematic showing gravel-bag placement and approximate defect dimensions/extent, and (b) field photograph of gravel bags attached to the rebar cage prior to installation.

a) 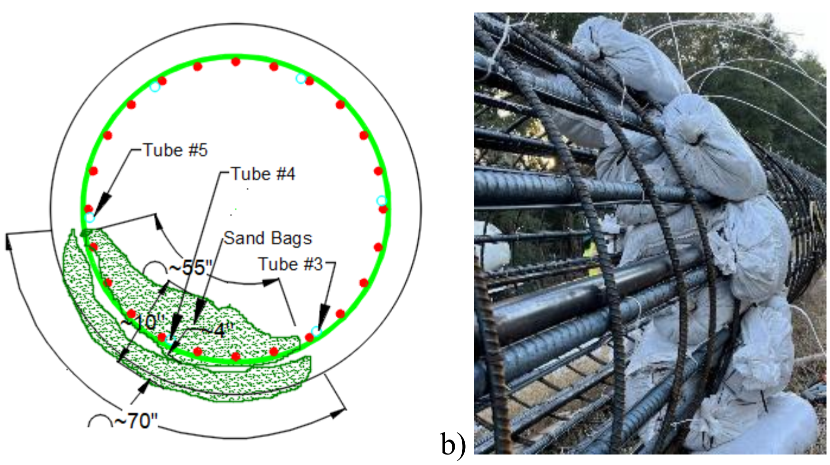 b)

Figure 4.5 Necking/soil-inclusion defect simulation using sandbags: (a) plan-view schematic showing the sandbag placement and approximate affected arc length/extent, and (b) field photograph of sandbags attached to the rebar cage prior to installation.

At L2 level (20 ft from the shaft bottom), an outside-cage necking/soil-intrusion condition, simulated using sandbags, was positioned near Tubes #3 to #5 (Figure 4.5**Error! Reference source not found.**) and attached along the longitudinal reinforcement with an approximate longitudinal (vertical) extent of 1.0 ft. The sandbag sector spans approximately with an inner circumferential extent of ~55 in. and an outer circumferential extent of ~70 in., and a representative radial thickness of ~10 in. across the sector. Using these dimensions and a 1-ft (12-in.) vertical extent, the corresponding approximate defect envelope volume is $(55+70)/2 \times 10 \text{ in} \times 12 \text{ in} \approx 7500 \text{ in}^3$, i.e., approximately 4.34 ft³ (about 32.5 gal), recognizing that the final value depends on the as-installed packing and contact against the cage/shaft wall.

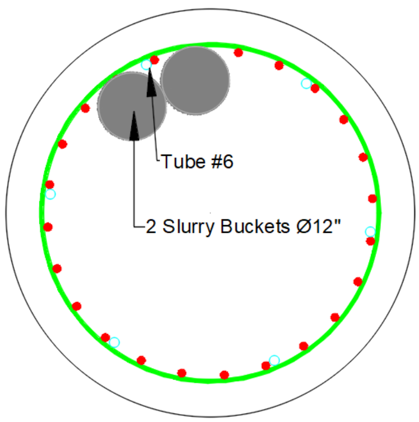

a)

b)

Figure 4.6 Slurry-inclusion defect simulation using buckets: (a) plan-view schematic of the Ø72-in. drilled shaft showing the placement of two Ø12-in. slurry buckets inside the reinforcement cage relative to the CSL tube layout, and (b) field photograph of the two buckets secured to the rebar cage prior to installation to represent entrapped slurry/low-quality concrete.

At L3 level (30 ft from the shaft bottom), a slurry-inclusion defect, simulated using two cylindrical slurry buckets, was installed inside the reinforcement cage adjacent to Tube #6 (Figure 4.6). Each bucket has a nominal diameter of 12 in. and a height of approximately 15.5 in., and a volume of 5 gal, for a total inclusion volume 10 gal for two buckets.

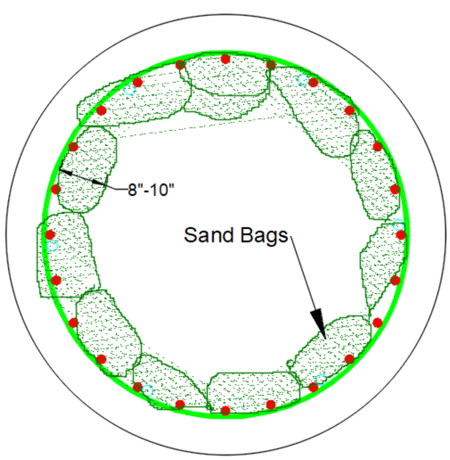

a)

b)

Figure 4.7 Soft-bottom defect simulation using sandbags: (a) plan-view schematic of the Ø72-in. drilled shaft showing the sandbag placement around the shaft perimeter (typical bag length approximately 8–10 in.), and (b) field photograph of sandbags secured around the base region of the rebar cage prior to installation to represent a soft-bottom condition.

Finally, a soft-bottom condition was simulated near the shaft base using sandbags arranged around the lower portion of the cage (Figure 4.7). The plan-view schematic indicates typical individual bag dimensions on the order of 8–10 in., and the installed soft-bottom bag ring has an approximate longitudinal (vertical) extent of ~10 in. along the cage, intended to emulate a compliant base condition and to evaluate UFWI sensitivity to bottom boundary effects. For verification, all embedded defects were documented as-built, including measured dimensions prior to placement, recorded elevations and azimuths relative to a defined cage reference line (0° datum), and installation photographs, to enable quantitative comparison between UFWI images and known defect geometry.

4.3.3 **Drilling and casting of the drilled shaft**

The test shaft was constructed using the wet-hole method with polymer slurry, consistent with field practice of the site conditions (Figure 4.8). Drilling proceeded to the design depth of 40 ft, while maintaining adequate slurry head to stabilize the excavation, and slurry properties and level were managed to minimize wall sloughing and excessive sedimentation. Upon reaching final depth, the excavation was cleaned to reduce loose cuttings and to provide a consistent base condition prior to cage placement and concreting.

Figure 4.8 Soil drilling and slurry maintain. The completed reinforcement cage, including CSL tubes and pre-installed simulated defects, was lifted and lowered into the slurry-filled borehole using plastic spacers to maintain alignment and minimize disturbance of defect placements and tube geometry (

Figure **4.9**).

Concrete was placed by tremie to limit segregation and minimize contamination by slurry, and placement was conducted continuously to avoid cold joints; tremie embedment below the rising concrete surface was maintained to reduce entrainment of slurry and air (Figure 4.10). Shown in Figure 4.11 is the drilled shaft concrete placement log. The placed concrete volume was tracked for individual concrete trucks and against the theoretical volume for a 6-ft shaft for quality control. Figure 4.12 shows the concrete volume. The theoretical shaft diameter was 6 ft. However, the intentionally embedded defect materials occupied part of the shaft volume that would otherwise have been filled with concrete. Therefore, when the measured concrete volume is back-calculated as an equivalent circular concrete-filled diameter without accounting for the defect volume, the resulting equivalent diameter can appear slightly smaller than the nominal 6-ft design diameter. This comparison should therefore be interpreted as an equivalent concrete-volume estimate rather than a direct measurement of the drilled shaft diameter. (e.g. measured concrete height/length is higher due to defects, leading to smaller diameter). During casting, the concrete head was maintained above the slurry interface to promote slurry displacement and reduce inclusions.

In addition, concrete samples were collected from all five trucks (corresponding to five concrete mixes), with four specimens prepared from each truck. Laboratory testing was conducted by the SMO team to determine compressive strength. The average 28-day compressive strengths, based on four specimens per mix, were 5,140 psi, 5,200 psi, 4,940 psi, 5,340 psi, and 6,190 psi for Mixes 1 through 5, respectively, indicating that the concrete quality was satisfactory.

Figure 4.9 Rebar cage placement in borehole. Plastic spacers were used to maintain alignment and cover thickness of 6 inches.

Figure 4.10 Tremie concrete casting.

DRILLED SHAFT CONCRETE PLACEMENT LOG CONSTRUCTION 9/20

Project Name	CSL Shaft Imaging - Hawthorne FDOT	Pier No.	1	Structure No./ID	1	Page	Of
Project No.		Shaft No.		Station		Offset	
Inspected By	F. Albelo	TIN #		Date		Approved By	Date
Contractor		Notes:					

Placement Method: Tremie (X) Pump ( )

SHAFT	Shaft Dia.	6.00	(ft)	Tremie ID (in)	12.00	Pump Line(s) 1	#	ID (in)	Length (ft)	Volume (VL)	Surface Form ID (in)	72.00
	REF Elev.	+100.00	(ft)	Tremie Length (ft)	38.00	2					Length (ft)	2.00
	Top Elev.	+98.50	(ft)	Rebar Cage Top Elev. (ft):		Notes:	Total Volume in Lines (VL) (cy) =				"Beauty Ring"	
	Bottom Elev.	+58.42	(ft)	@ Start		3' Hopper not included in Tremie Length						
Max. Temp. During Pour		64	(°F)	@ Finish	98.17	4" Cover target for beauty ring to cage. Approximation, no benchmarks on casing removal.						

Plant No. 26-518; Mix No. 02-2448-01

	Truck No.	Batch Time	Start Time (ED or Not Placed)	Finish Time	Tremie Depth (ft)	Depth to Concr (ft)	Concr. Elev. (ft)	Volume Delivered (cy)	Left in Pump Hopper (LPH) (cy) Before Truck Placement ($LPH_{1before}$)	After (LPH_{1after})	Volume Wastage (VW) (cy) Testing	Left in Truck	Left on Ground (Spillage)	Prime Lines	Volume in Lines (VL) (cy)	Vol. Placed (VP) (cy)	Accum. Vol. Placed (cy)	Notes
1	4169	12:45 PM	1:52 PM	2:06 PM	41.00	32.60	67.40	9.00			0.20		0.10			8.70	8.70	S=7.5 10 Gal Water Added, S=8
2	4686	12:57 PM	2:09 PM	2:20 PM	40.50	23.70	76.30	9.00			0.10					8.90	17.60	S= 7.75
3	4699	1:03 PM	2:26 PM	2:35 PM	39.00	15.00	85.00	9.00			0.10					8.90	26.50	S=9
4	4054	1:38 PM	2:54 PM	3:20 PM	37.00	7.00	93.00	9.00			0.20					8.80	35.30	S=7.25 10 Gal Water Added. S=8.75
5	4584	2:21 PM	3:31 PM	4:15 PM	11.00	0.50	99.50	9.00			0.10		0.10			8.80	44.10	S=7.75 Removing 2 Tremie segments
6	4686	4:19 PM	5:22 PM	5:26 PM	0.00	0.00	100.00	3.00			-	3.00	-			0.00	44.10	Volume used for Beauty Ring Approx 1 cy.
7																		
8																		
9																		
10																		
	Pg. 1 Totals (XX_1) (Truck loads 1-10)	48.00 -	= VD_1					48.00			0.70	3.00	0.20		0.00	44.10	← VL_1	
	Placement TOTALS (XX_T) (sum Pg. 1)	VD_{1Total}	VD_{1RNP}				VD	48.00	LPH_{Tafter}	$LPH_{Tbefore}$ VW 3.90		VW_T 3.90		VL_T	0.00	44.10	VP_T	

VD_{TOTAL} (Pg 1-3) 48.00 - 0.00 = 48.00 [VD_{RNP} = $VD_{Rejected\ or\ Not\ Placed}$]

VD - VW [incl. LPH (After Placement) - LHP (Before Placement)] - VL =

Rebar Cage Centered? Y (X) N ( )

CASING:	ID (in)	Top EL (ft)	Bot. EL (ft)	Installation Time Start	Installation Time Finish	Removal Time Start	Removal Time Finish
Casing 1	84.00	100.00	96.00	-	-	4:27 PM	4:30 PM
Casing 2							

Slump Loss – max elapsed time (mix design)	5.00
Time Conc. Placement Finished & Bolts	5:26 PM
Concr. Placement Time (per 455-17.2) (hrs)	4.68
*Vol. Theor. (VT) (cy) 44.41	Overpour (OP) (cy) -0.31

VT - includes Ext. Steel input; OP = VP - VT

Figure 4.11 Drilled shaft concrete placement log.

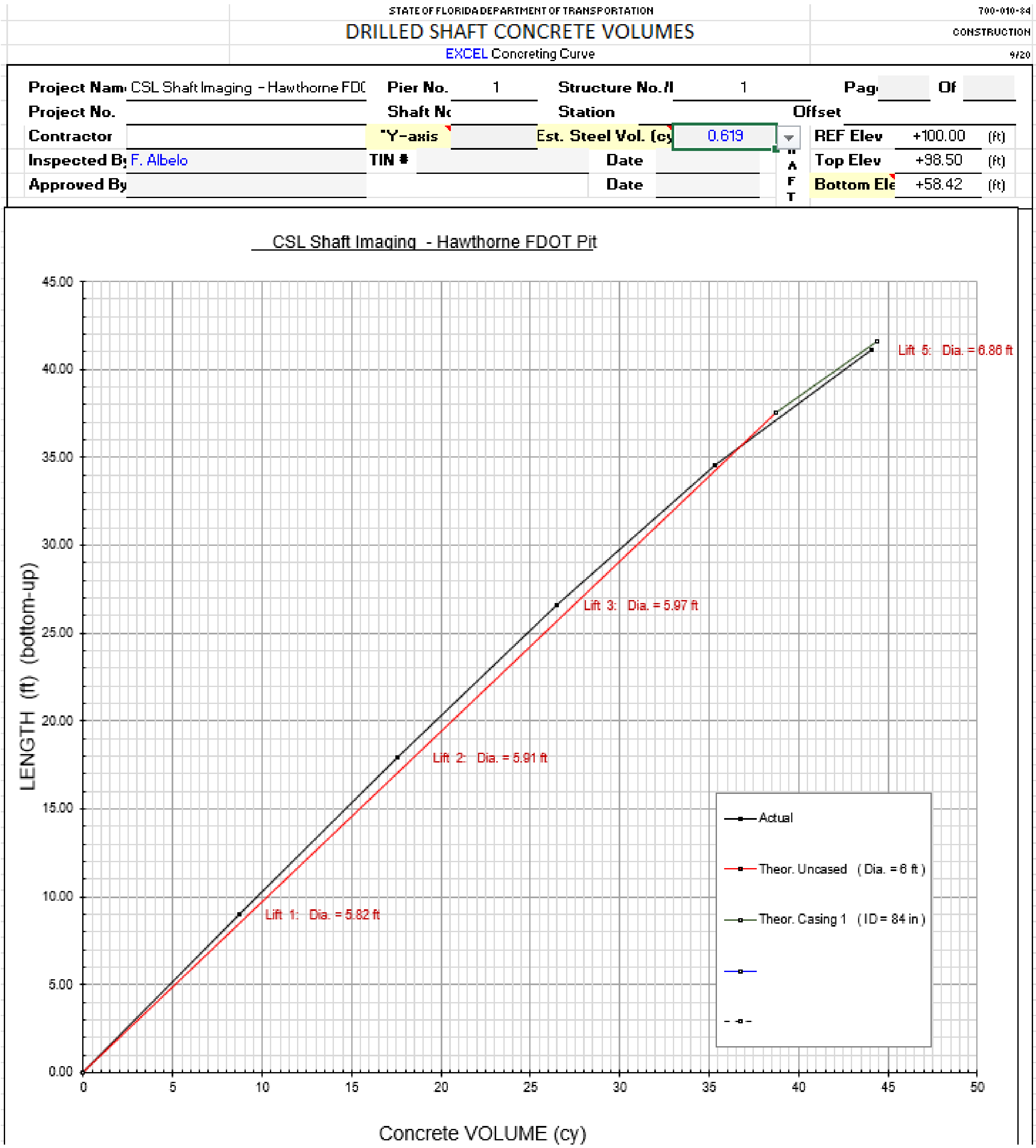

Figure 4.12 Drilled shaft concrete volume. The theoretical volume corresponds to a nominal 6-ft-diameter shaft. Because the intentionally embedded defect materials displaced part of the concrete volume, the equivalent concrete-filled diameter back-calculated from the measured concrete volume may appear slightly smaller than 6 ft when the defect volume is not explicitly accounted for.

4.4 **Data acquisition**

Ultrasonic data acquisition was performed on the constructed test shaft using the six pre-installed CSL tubes. The CSL measurements used for UFWI were collected on the third day after shaft construction/concrete placement. The field-testing setup, shown in Figure 4.13, follows ASTM standards for CSL testing. The measurements were designed to provide a high-quality field dataset for evaluating the UFWI method under realistic drilled shaft conditions.

Figure 4.13 Field CSL testing setup at the Hawthorne FDOT pit showing the instrumented test shaft and on-site acquisition equipment.

With six access tubes, a total of 15 nonredundant tube pairs were measured using the standard CSL pairwise data collection. During testing, the transmitter and receiver were lowered together at the same elevation in a selected tube pair, and the full waveform was recorded for that pair at each depth level. The 15 measured pairs correspond to all tube-pair combinations among the six access tubes. Reciprocal measurements were not repeated based on the acoustic reciprocity principle, under which the response recorded with the source in tube i and the receiver in tube j is theoretically equivalent to the response obtained when the source and receiver are interchanged, provided that the source signature, tube coupling, and measurement conditions remain unchanged. Repeating this standard pairwise procedure for all tube pairs and depths produced the full-waveform CSL dataset used for UFWI.

CSL data was acquired at uniform depth intervals along the shaft length. During each measurement, the transmitter and receiver were maintained at the same elevation so that the recorded wavefield primarily represents horizontal propagation between tube pairs at a given depth. Measurements were collected at 2 cm intervals, yielding 576 depth levels over an effective testing length of approximately 11.5 m.

During acquisition, basic field quality checks were performed by monitoring the recorded waveforms for proper triggering, reasonable signal amplitude, clear first arrivals, acceptable noise level, and consistency with adjacent depth measurements. Measurements with abnormal signals, such as very weak amplitude, excessive noise, unclear first arrivals, or apparent coupling problems, could be repeated in the field. These checks are part of good CSL data-collection practice and are not unique to UFWI. However, UFWI requires raw digitized waveform records, rather than only processed CSL outputs, because the inversion uses waveform shape, phase, and amplitude information after preprocessing and quality control. Therefore, previous CSL datasets collected using standard pairwise procedures can also be used for UFWI if the raw waveforms, tube geometry, and depth information are available and the data quality is sufficient.

The recorded signals include direct arrivals propagating through the concrete between tube pairs, as well as later arrivals influenced by scattering, attenuation, and geometric effects associated with shaft heterogeneity and embedded defects. Compared with conventional CSL analysis, which primarily relies on first-arrival times and signal energy metrics, the full waveforms contain substantially richer information for inversion-based imaging. This is particularly important for imaging shaft boundary, and characterizing defects whose effects extend beyond simple travel-time delays, such as localized low-velocity inclusions, segregation zones, necking-related anomalies, and soft-bottom conditions.

To ensure reliable inversion, basic data quality was first checked during CSL acquisition by monitoring the raw waveforms for proper triggering, reasonable amplitude, clear first arrivals, acceptable noise level, and consistency with adjacent depth measurements. Measurements showing abnormal responses could be repeated in the field. However, the UFWI-specific data screening and preprocessing, including trace inspection, frequency filtering, low-energy channel removal, and time windowing, were performed after data acquisition and before inversion. The processed dataset then served as the primary input for evaluating the capability of UFWI to reconstruct the shaft condition and identify the intentionally embedded defects. These procedures are described in the following section. The processed dataset serves as the primary field input for evaluating the capability of UFWI to reconstruct the internal condition of the shaft and to identify the intentionally embedded defects under realistic construction conditions.

4.5 **Data preprocessing**

The raw ultrasonic measurements acquired from the CSL tubes were processed prior to inversion to improve signal consistency, reduce the influence of high-frequency noise, and exclude poor-quality data channels that were not suitable for UFWI. The preprocessing sequence included frequency filtering, energy-based channel screening, and time windowing of the waveforms.

Specifically, the original waveforms were band-pass filtered at 5-35 kHz, so that the processed signals retained the more stable lower-frequency content with the dominant frequency centered near approximately 25 kHz (**Figure 4.14**). The raw spectra showed strong received energy at higher frequencies, including a dominant component around approximately 55 kHz. This higher-frequency energy is not noise; it represents the emitted ultrasonic signal after propagation through the CSL tubes, concrete, reinforcement zone, and receiver system. However, these higher-frequency components were not used directly for UFWI because they are more sensitive to local coupling variations, small-scale concrete heterogeneity, reinforcement scattering, and modeling error. In addition, higher frequencies require a smaller numerical grid size to maintain adequate points per wavelength, which significantly increases computational memory and runtime. Higher-frequency waveform inversion is also more susceptible to cycle skipping and convergence difficulty when the initial model does not closely reproduce the measured waveforms. Therefore, the filtering band was selected as a compromise among spatial resolution, computational feasibility, and inversion stability. By retaining the lower-frequency waveform content and removing most energy above approximately 35 kHz, the processed data preserved the primary waveform characteristics needed for UFWI while improving robustness and consistency across tube pairs.

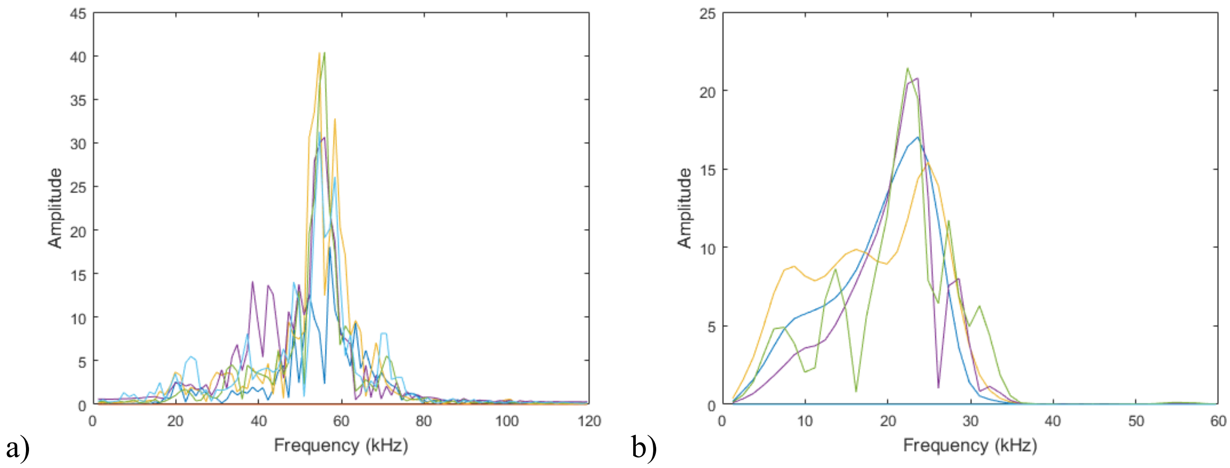

Figure 4.14 Amplitude spectra of representative ultrasonic data before (a) and after (b) filtering, showing the effective bandwidth used for inversion.

Following frequency filtering, an energy-based quality-control procedure was applied to identify and remove poor channels. For each source-receiver combination, the average signal amplitude was computed and normalized by the maximum value within the corresponding dataset. A relative energy measure in decibels was then calculated as

$$\mathrm{Energy}_{\mathrm{dB}}(i,j,\cdot) = 20\log\left(\frac{A(i,j,\cdot)}{\max\left(A(i,j,\cdot)\right)}\right), \tag{4-1}$$

where $A(i,j,\cdot)$ denotes the average amplitude associated with the measurement channel for source tube i and receiver tube j. This normalization provided a consistent way to compare signal strength for each channel and to identify measurements with abnormally weak amplitudes. Data were classified as poor quality and excluded from further analysis when the relative energy fell below a threshold of -12 dB. The relative-energy screening results used to identify poor-quality channels are shown in Figure 4.15. In practice, this criterion removed traces with substantially reduced signal amplitude, which are commonly associated with weak coupling, poor transmission, excessive attenuation, or other acquisition-related issues. Excluding such low-energy data helped reduce the influence of unreliable waveforms on the inversion and improved the overall stability of the reconstructed images.

After channel screening, a time-windowing procedure was applied to each remaining trace. The waveform before the first arrival was muted to suppress pre-arrival noise and unrelated low-amplitude fluctuations. The waveform after approximately twice the first-arrival time was also muted. This windowing strategy was adopted because the inversion in this study targeted only the compressional-wave velocity Vp, using an acoustic forward modelling. At later times, the recorded waveforms may contain contributions from mode-converted or shear-wave related energy that are not represented by the adopted acoustic inversion physics. Including those late arrivals could therefore introduce model-data mismatch and degrade inversion stability. By retaining direct arrival and early waveform coda, the processed data remained more consistent with the governing assumptions of the UFWI formulation and more sensitive to the Vp variations of interest.

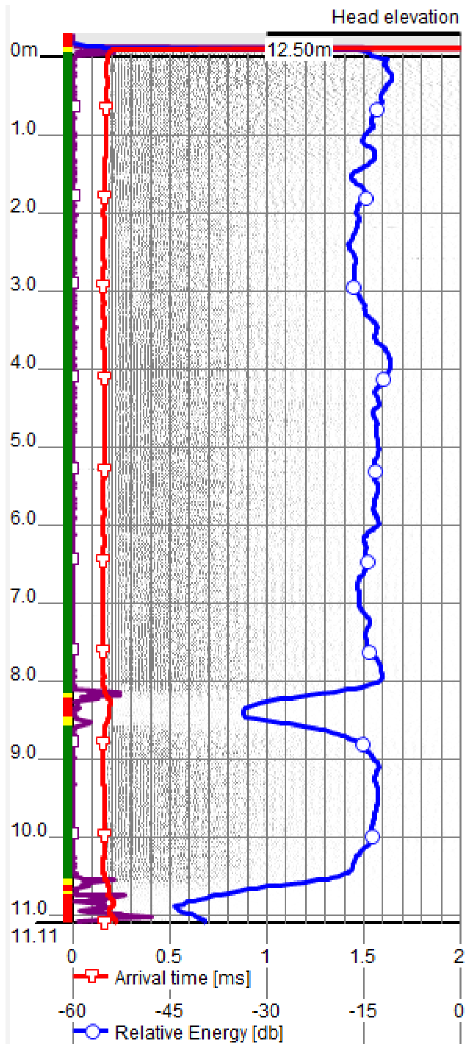

Figure 4.15 Relative energy of the measured channels used for data quality control. Traces with $\text{Energy}_{\text{dB}} < -12\text{dB}$ were excluded from inversion.

After frequency filtering, poor-channel screening, and time windowing, the remaining waveforms constituted the final input dataset for UFWI. The poor-channel screening was implemented with a data-sufficiency safeguard. Specifically, low-energy traces were removed only when enough measurements remained to provide adequate tube-pair coverage at the corresponding depth. If the −12 dB screening threshold would remove all measurements at a given depth slice, the original waveforms for that slice were retained rather than discarded. This approach prevents the inversion from being performed with an empty dataset and preserves the available acquisition geometry. As a result, the preprocessing reduced the influence of unreliable traces where possible, while maintaining sufficient data coverage for field-scale UFWI and interpretation of the intentionally embedded defect conditions. Figure 4.16 compares representative ultrasonic data before and after preprocessing, including the raw waveforms and the corresponding processed waveforms. These processed data preserved the primary arrival information and early waveform content required for inversion while minimizing the adverse effects of noise, unreliable channels, and late-time complexities. The resulting dataset was therefore considered appropriate for field-scale inversion and subsequent interpretation of the intentionally embedded defect conditions.

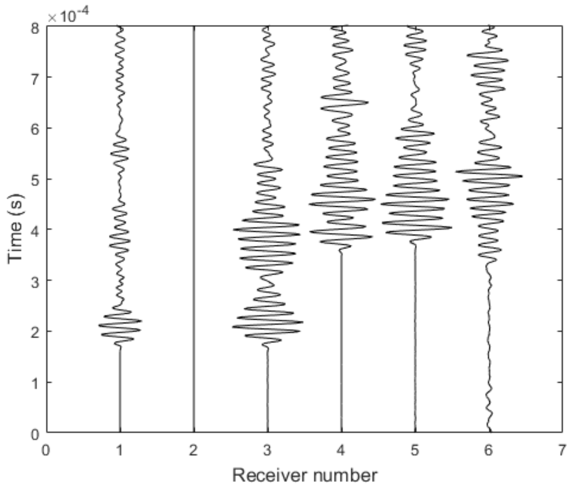

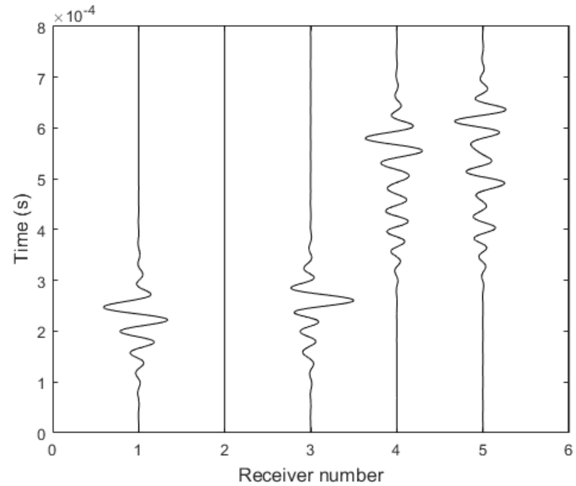

Figure 4.16 Representative ultrasonic shot gathers before and after preprocessing**:** (a) raw data; (b) processed data used for UFWI.

4.6 **Inversion results**

The processed CSL data was inverted using the UFWI workflow developed in Chapter 2 to reconstruct cross-sectional velocity images at depths along the shaft length. Interpretation focused on whether the recovered anomalies matched the documented as-built defect type, depth, and azimuthal position, rather than on exact replication of the physical defect boundaries. In the inverted images, lower-velocity zones generally indicate reduced concrete quality, soil intrusion, slurry inclusion, or soft-bottom effects, whereas relatively higher-velocity or more heterogeneous zones may be associated with aggregate-rich or segregated concrete.

A cross section without intentionally embedded defects was first analyzed to evaluate the baseline performance of the UFWI workflow under relatively sound concrete conditions. This section also demonstrates the main processing and inversion steps used for the following defect slices, including raw data inspection, frequency-domain analysis, preprocessing, initial model construction, waveform matching, convergence evaluation, and final velocity interpretation.

4.6.1 Shaft section without defects

Figure 4.17 shows an example of the raw CSL data acquired at the non-defective elevation. The time-domain waveforms exhibit clear first arrivals and relatively strong ultrasonic oscillations for most receiver channels, indicating good signal transmission through the concrete. The corresponding frequency spectra show that the raw data contain strong high-frequency energy, mainly concentrated around approximately 20–80 kHz. Although these high-frequency components provide fine resolution, they are also more sensitive to noise, tube coupling variations, scattering from reinforcement, and small-scale concrete heterogeneity. Therefore, direct inversion of the raw data may increase instability and produce small-scale artifacts.

Figure 4.18 presents the same data after the preprocessing described in section 4.5. Compared with the raw waveforms, the preprocessed traces are smoother and dominated by lower-frequency components. The spectra indicate that the retained energy is mainly concentrated around approximately 10–30 kHz. This frequency reduction improves the stability of the waveform inversion by emphasizing the major transmitted P-wave energy and reducing the influence of high-frequency noise and late scattered arrivals. The preprocessing step therefore provides a more reliable input dataset for reconstructing the large-scale velocity structure of the shaft cross section.

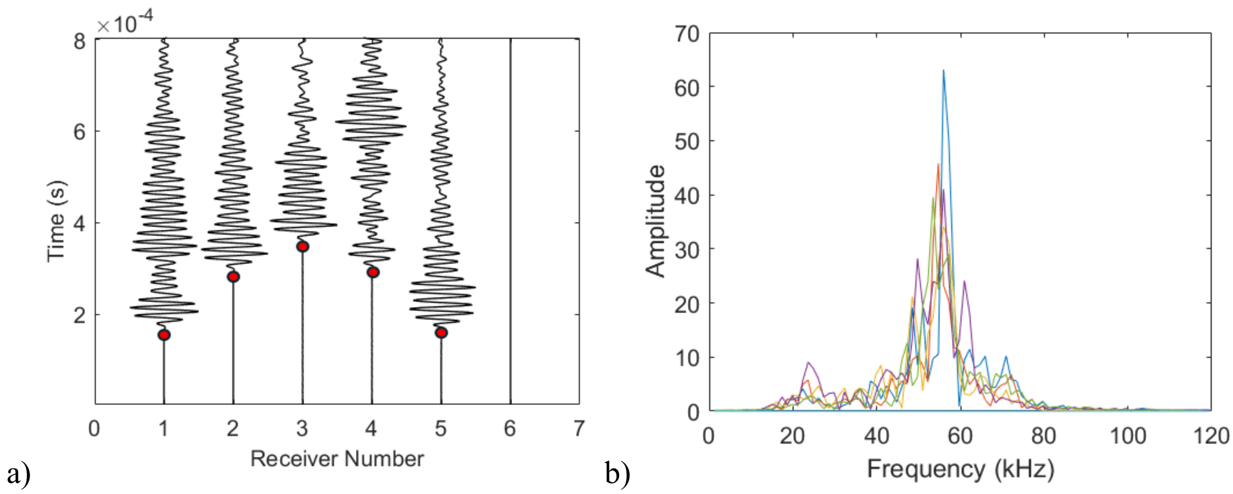

Figure 4.17 Example of raw data**:** (a) waveform and (b) its corresponding spectrum

The initial model is established from first-arrival picks tf(z) on the raw CSL data. With the known tube-to-tube separation L, straight-ray velocities are estimated by v(z)=L/tf(z) to obtain the initial homogeneous model for inversion. Figure 4.19 shows the initial velocity model used for the inversion. This simple initial model assumes uniform sound concrete and does not contain any prior defect information or shaft boundary. This is the main novelty of the developed UFWI method, that does not require any information about the shaft (boundary or concrete volume). The shaft boundary is imaged from the inverted results.

The inversion used waveform data with frequency content primarily in the 10–30 kHz range (Figure 4.18b). The inversion procedure was terminated under any of the following criteria: (1) reaching a maximum of 400 iterations, (2) failing to determine an optimal step length (no better model), or (3) attaining less than 0.1% improvement in the least-squares misfit over 20 consecutive iterations. The computational time was 25 minutes for each depth on a desktop computer (3.70 GHz, 8 cores, 64 GB RAM).

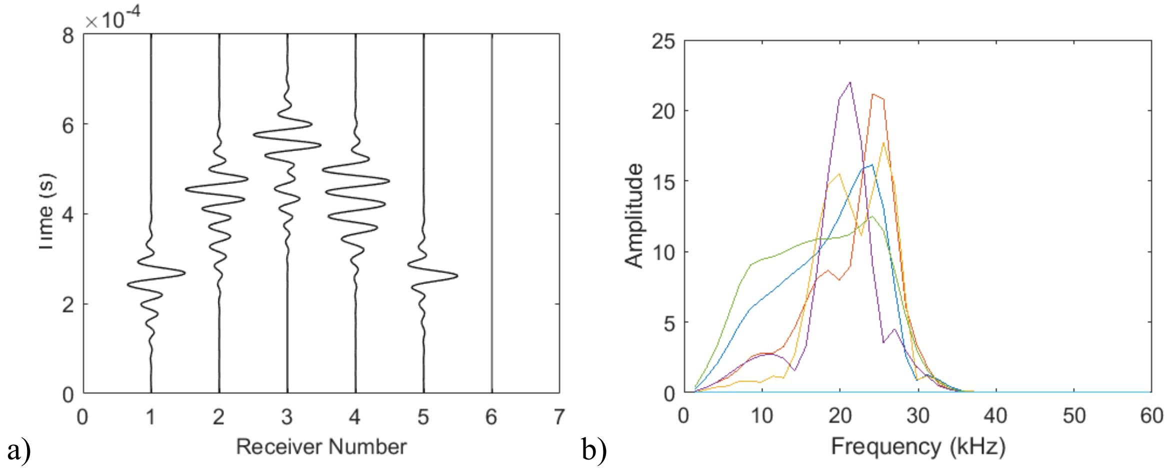

Figure 4.18 Example of preprocessed data**:** (a) waveform and (b) its corresponding spectrum

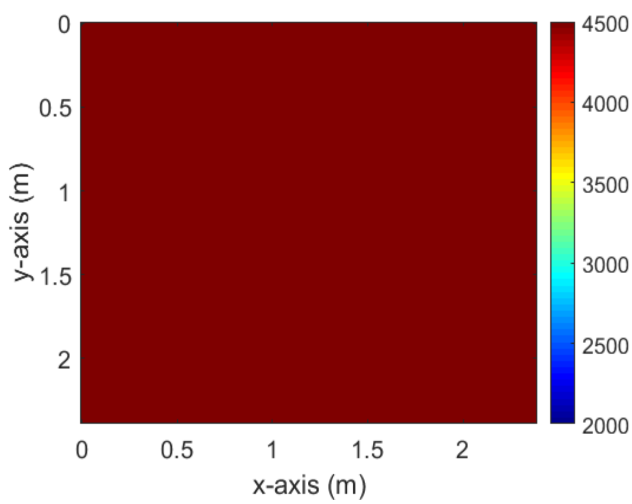

Figure 4.19 Initial model used at the beginning of analysis, without requiring any information the shaft.

Figure 4.20 compares the observed data with the estimated data calculated from the initial and final models. For the initial model, the estimated traces reproduce the approximate arrival times, but noticeable differences remain in phase, waveform shape, and amplitude. These mismatches occur because the estimated data are computed from the initial homogeneous model, which does not include the shaft boundary or the surrounding soil. In contrast, after inversion, the estimated waveforms from the final model (iteration 400) show improved agreement with the measured data. The arrival times and major waveform phases are better aligned, demonstrating that the UFWI process successfully updated the velocity model and reduced the data misfit.

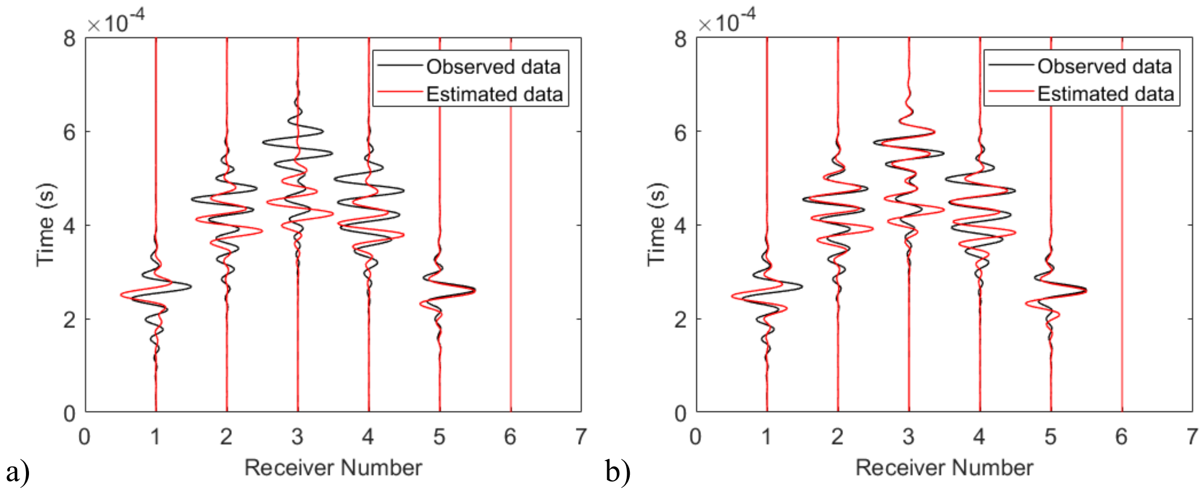

Figure 4.20 Comparison of observed data with estimated data associated with the initial model (a) and final model (b).

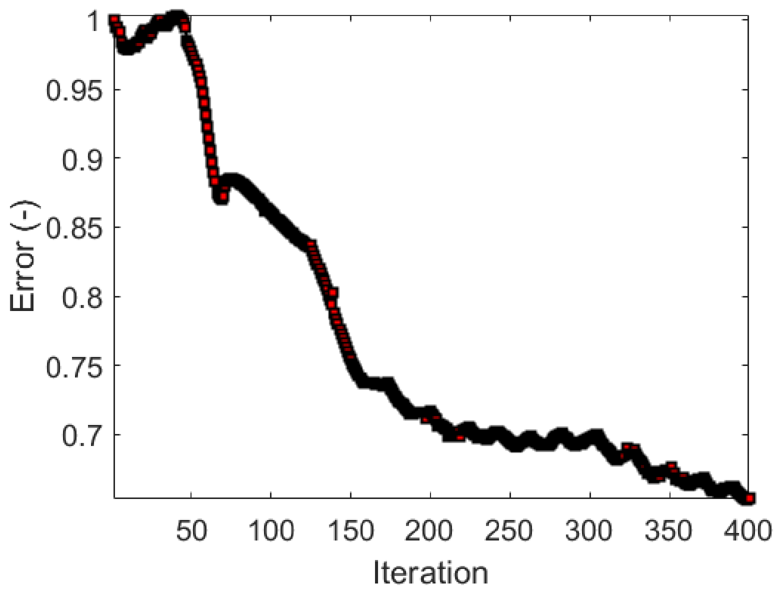

Figure 4.21 Error functions for all 400 iterations.

The convergence behavior is shown in Figure 4.21. The error function decreases progressively from the initial value and shows a major reduction during the early and middle stages of inversion. After approximately 200 iterations, the error reduction becomes more gradual, suggesting that the inversion has captured the dominant velocity structure and is mainly making smaller refinements. By 400 iterations, the error decreases to approximately 0.65, indicating stable convergence without obvious divergence or oscillatory instability. This convergence trend confirms that the preprocessing strategy, initial model, and inversion parameters are suitable for the field CSL data.

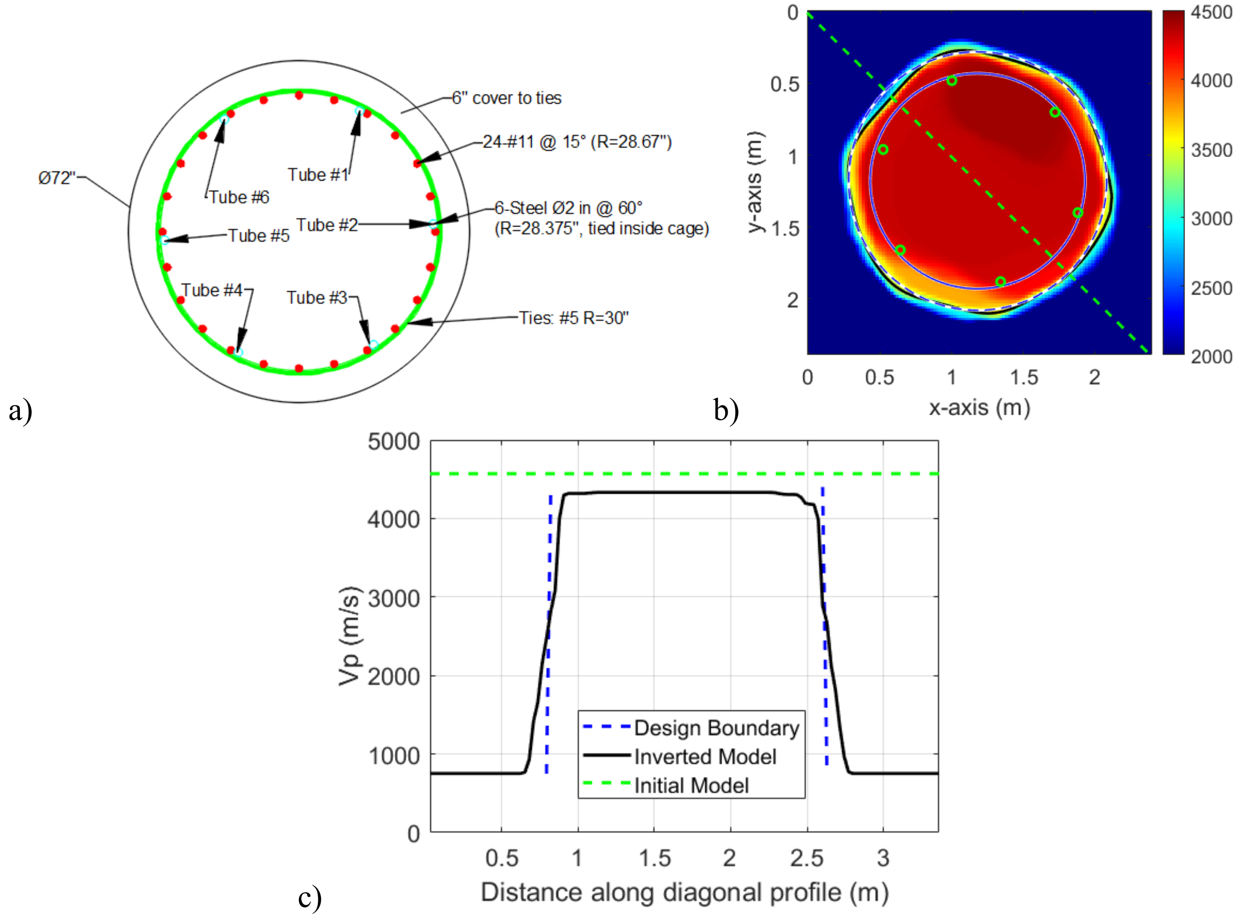

Figure 4.22 Comparison of (a) design schematic and (b) UFWI result. The black solid line and the dash line denote the inferred boundary and the design boundary. Blue line inside concrete is the rebar cage, c) velocity profile extracted along the green line in (b).

Figure 4.22 compares the design schematic with the final UFWI result for the non-defective section. Figure 4.22(a) shows the design schematic of a horizontal slice without defects, and Figure 4.22(b) shows the corresponding inverted Vp model. The inversion result clearly shows a sharp velocity reduction from the high-velocity concrete inside the shaft to the low-velocity surrounding soil outside the shaft boundary. The inferred boundary, indicated by the solid black line, closely aligns with the designed shaft boundary, indicated by the blue dashed line, demonstrating the capability of the UFWI method to recover the shaft geometry. The inferred boundary can be used to determine actual cover thickness of rebars/rebar cage (blue circle), which is crucial for protection of rebars from corrosion. For example, the cover thickness is only about 10 cm (4 inches) at the top left area of the cross section in Figure 4.22(b), while the remaining cover thickness is approximately 15 cm (6 inches ± 0.5 in).

Figure 4.22(c) presents the velocity profile extracted along the green line in Figure 4.22(b), comparing the initial, inverted, and design models. The inverted profile shows a sharp decrease in Vp from approximately 4,300 m/s inside the shaft to around 800 m/s outside the shaft. The clear velocity transition occurs near approximately 3,200 m/s, which was used as the threshold to identify the drilled shaft boundary in Figure 4.22(b). Inside the shaft, the inversion image shows a high-velocity zone, consistent with sound concrete. No low-velocity anomaly is observed within the shaft area, which agrees with the design condition that no intentional defect was placed at this elevation. Minor velocity variations are present inside the shaft, but these are expected for field concrete and may be related to aggregate distribution, reinforcement effects, tube coupling, and limited acquisition aperture. The outside region remains at a low velocity because it represents the surrounding soil, which has a much lower wave velocity than sound concrete. Overall, this non-defective slice serves as an important baseline for interpreting defect horizons. The workflow successfully converts raw high-frequency CSL data into a high-resolution 2D image of both shaft and surrounding soil. The shaft boundary is excellently characterized.

For further validation of the UFWI method, each defect in the following section is summarized using a three-column comparison that includes the field photograph, the design schematic, and the corresponding UFWI result. This format enables direct comparison between the known as-built configuration and the recovered anomaly pattern.

4.6.2**L1 concrete-segregation / aggregate-rich defect**

Figure 4.23 compares the as-built L1 defect configuration with the corresponding UFWI reconstruction at the same elevation (30 ft depth). As shown in Figure 4.23(a) and (b), the defect was simulated using gravel bags placed adjacent to the reinforcement cage between tube #6 and tube #1, near the upper perimeter of the shaft cross section. In the UFWI result in Figure 4.23(c), a low-velocity zone is observed in this same upper azimuthal sector, indicating that the inversion captured the presence and approximate location of the embedded anomaly. The planned gravel-bag defect had an outer circumferential extent of approximately 1.52 m (60 in.). In comparison, the recovered low-velocity zone is estimated to extend approximately 1.65–1.78 m (65–70 in.) along the shaft perimeter. Thus, the imaged anomaly is approximately 10 in longer. This apparent broadening may be related to limited concrete flow through the rebar cage at the location of the aggregate bags, possible enlargement of the actual affected zone during concrete placement, and smoothing effects associated with finite wavelength and regularization in the inversion.

In addition, the recovered L1 feature appears relatively subtle and spatially diffused, rather than as a sharply defined isolated anomaly. This behavior is reasonable because the gravel-bag defect represents an aggregate-rich /segregation-type condition, whose effective acoustic contrast with the surrounding concrete is expected to be smaller than that of a soil intrusion. As a result, the inversion response is expressed mainly as a localized disturbance in the velocity pattern rather than a strong, discrete low-velocity zone. The reconstructed feature also extends somewhat inward from the boundary, which is expected given the smoothing effect of regularization and the limited illumination associated with defects located close to the shaft perimeter.

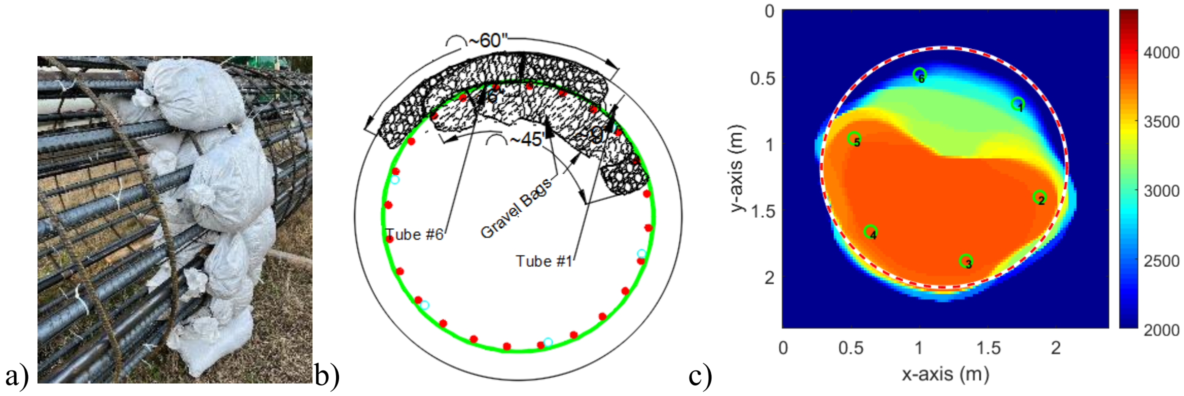

Figure 4.23 Comparison of the L1 concrete-segregation / aggregate-rich defect**:** (a) field photograph, (b) design schematic, and (c) UFWI result. The dash line denotes the designed shaft boundary.

Overall, Figure 4.23 shows that UFWI was able to detect the defect in the correct upper sector between Tubes #6 and #1, consistent with the true location of the concrete-segregation/aggregate-rich zone. Although the recovered image does not reproduce the exact gravel-bag geometry, it provides reasonable agreement with the known as-built condition and demonstrates sensitivity to this more subtle defect type under field conditions.

4.6.3 **L2 necking / soil-inclusion defect**

Figure 4.24 compares the as-built L2 defect configuration with the corresponding UFWI reconstruction at the same elevation (20 ft depth). As shown in Figure 4.24(a) and (b), the defect was simulated using sandbags installed both outside and inside the reinforcement cage near tubes #3 to #5, forming a sector-shaped anomaly along the lower-left portion of the shaft cross section. This configuration represents a combined necking / soil-intrusion condition located close to the shaft boundary.

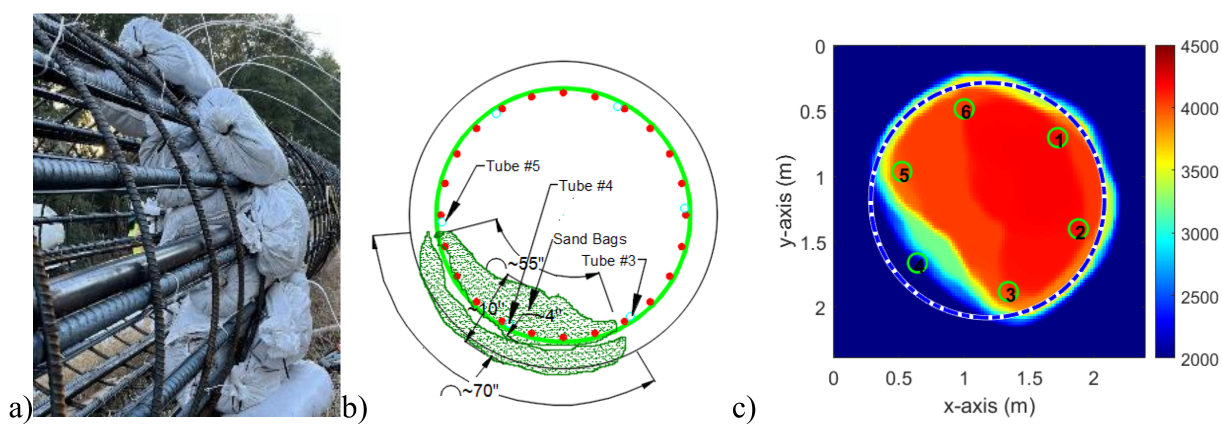

Figure 4.24 Comparison of the L2 necking / soil-inclusion defect**:** (a) field photograph, (b) design schematic, and (c) UFWI result. The dash line denotes the designed shaft boundary

In the UFWI result shown in Figure 4.24(c), a clear localized lower-velocity zone is observed in the same lower-left azimuthal sector, extending from tube #5 toward tube #3. This spatial correspondence indicates that the inversion successfully detected the presence, location, and approximate size of the defect. Again, the recovered anomaly is not confined to a sharply defined arc matching the exact sandbag geometry but instead appears as a broader low-velocity region distributed inward from the shaft perimeter. This smoothing is expected because the inversion recovers an equivalent velocity perturbation influenced by finite wavelength, regularization, and the limited angular coverage of the measurement geometry.

Overall, the result demonstrates that UFWI can detect and localize a necking /soil-inclusion defect both inside and outside the rebar cage under field conditions. The recovered image shows good agreement with the known defect azimuth and depth (20 ft from the tip). The UFWI result shows a low-velocity response at the same nominal depth range, indicating consistency between the reconstructed anomaly and the field-installed defect location.

4.6.4 **L3 slurry-inclusion defect**

Figure 4.25 compares the as-built slurry-inclusion defect with the corresponding UFWI reconstruction at the L3 elevation. As shown in **Figure 4.25**(a) and (b), two slurry buckets were installed inside the reinforcement cage adjacent to tube #6, near the upper perimeter of the shaft cross section. In the UFWI result in **Figure 4.25**(c), this defect is expressed as a localized lower-velocity zone in the same azimuthal sector, near the shaft boundary between tube #6 and tube #1. It is expected the slurry buckets blocks concrete flow through the rebar cage, resulting in low-velocity zone outside rebar cage. This spatial agreement indicates that UFWI successfully identified the presence and approximate location of the embedded slurry-related anomaly.

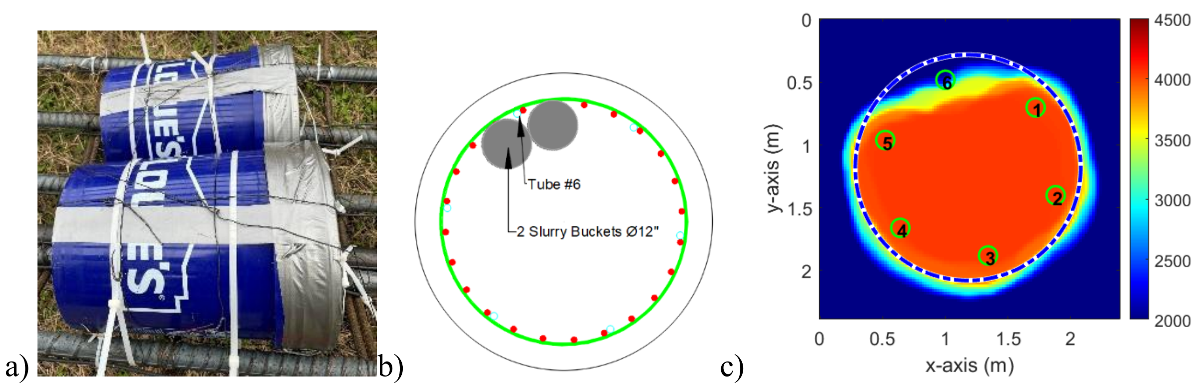

Figure 4.25 Comparison of the L3 slurry-inclusion defect**:** (a) field photograph, (b) design schematic, and (c) UFWI result.

The recovered anomaly, however, appears as a broader and smoother low-velocity region rather than two distinct circular inclusions matching the exact bucket geometry. This difference is expected because the inversion recovers an equivalent velocity perturbation constrained by limited-angle acquisition (limited tubes), and the finite wavelength of the ultrasonic data. In addition, the defect was located close to the shaft boundary, where image resolution is commonly affected by boundary scattering and reduced illumination. Even with these limitations, the inversion result remains consistent with the known as-built condition by showing a clear localized disturbance in the correct upper sector of the shaft cross section. Overall, the result demonstrates that the UFWI method can detect slurry-inclusion defects under field conditions, although the reconstructed shape is more diffuse than the true physical configuration.

4.6.5**Soft-bottom condition**

Figure 4.26 compares the as-built simulated soft-bottom configuration with the corresponding UFWI reconstruction near the shaft base. As shown in **Figure 4.26**(a) and (b), the defect was created using sandbags arranged around the perimeter of the cage to represent a compliant and disturbed bottom boundary rather than a localized inclusion at a single azimuth.

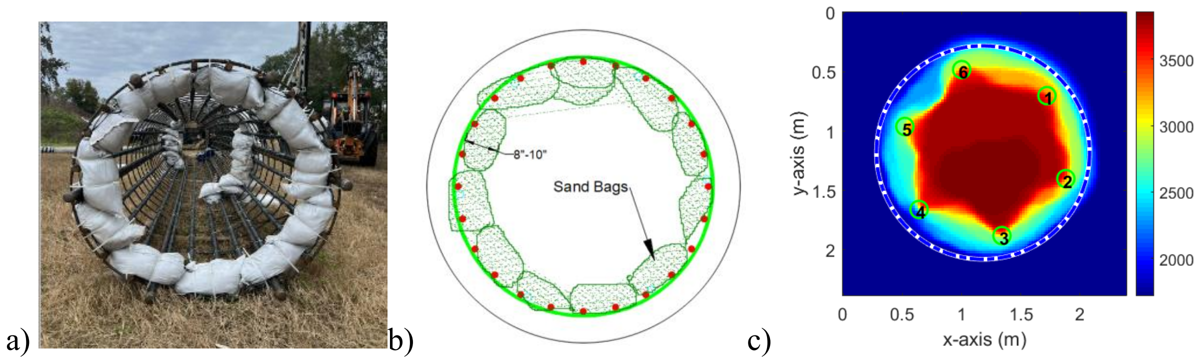

Figure 4.26 Comparison of the simulated soft-bottom condition**:** (a)field photograph, (b) design schematic, and (c) UFWI result.

In the UFWI result shown in Figure 4.26(c), low-velocity regions are observed around the shaft perimeter. It is expected that the sandbags blocked concrete flow through the rebar cage, and cutting soils stuck around the borehole perimeter, which cannot float when pumping concrete due to sandbags, resulting in low-velocity zone outside rebar cage as well. This pattern is consistent with the simulated soft-bottom condition and indicates that the inversion is sensitive to the altered material condition near the base of the shaft. Overall, the result demonstrates that UFWI can detect the presence of a soft-bottom-related boundary anomaly under field conditions.

4.6.6 **3D comparison of as-built defects and UFWI reconstruction**

Figure 4.27 provides an overall comparison between the documented defect configuration, the actual instrumented cage in the field, and the three-dimensional UFWI-derived Vp model. Panel (a) shows the defect layout relative to the six CSL tubes, including the L1 gravel-bag defect, the L2 sandbag necking/soil-inclusion defect, the L3 slurry-bucket defect, and the soft-bottom condition near the shaft base. Panel (b) presents the field photograph of the reinforcement cage with the installed defect simulants, confirming that the targets were physically placed at distinct elevations prior to concreting. Panel (c) shows the full 3D Vp rendering from UFWI, in which the shaft is dominated by high velocities of concrete, while localized lower-velocity zones appear at four elevations of defects. Panel (d) isolates these lower-velocity anomalies using a threshold velocity of less than 3,200 m/s, thereby making their spatial relationship to the known defect horizons clearer.

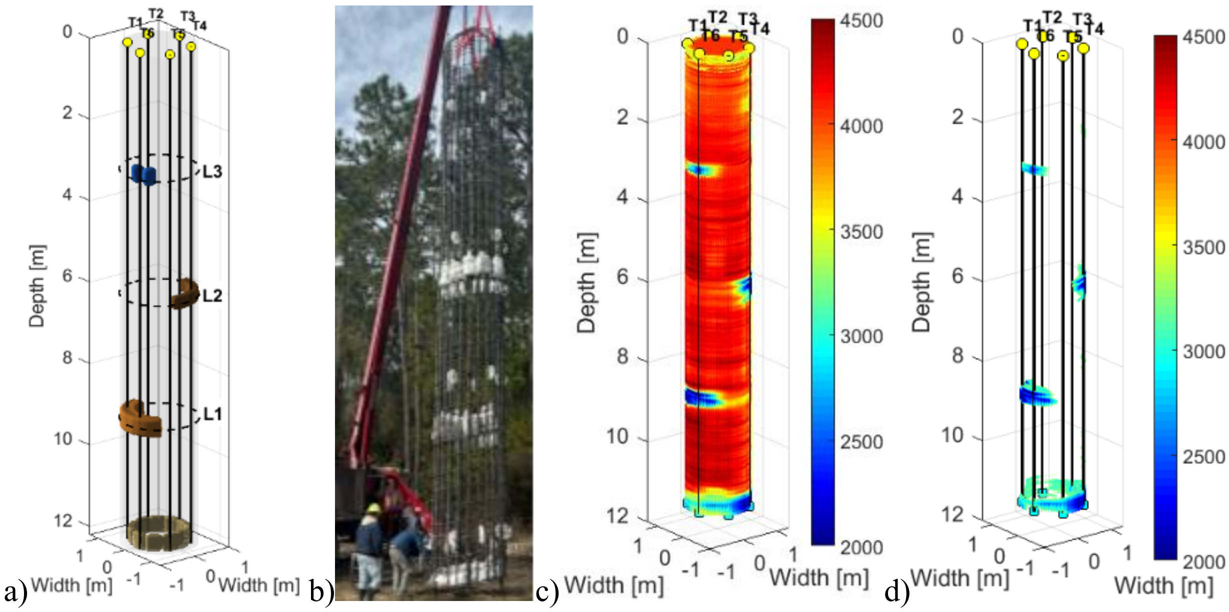

Figure 4.27 Three-dimensional comparison of the drilled shaft defect configuration and UFWI results**:** (a) designed defect layout, (b) field photograph of the instrumented reinforcement cage, (c) 3D Vp rendering of the full shaft, and (d) extracted low-velocity UFWI anomalies associated with the embedded defects and soft-bottom condition.

Overall, the figure shows good qualitative agreement between the documented defect elevations and the recovered UFWI anomalies. Distinct low-velocity features are visible at the L1, L2, and L3 horizons, and a distributed anomaly is present near the shaft base, consistent with the simulated soft-bottom condition. This correspondence indicates that UFWI successfully captured the positions and general sizes of the embedded defects within the full shaft.

However, the reconstructed anomalies are smoother and more spatially diffused than the true physical defect geometries shown in the as-built rendering. This difference is expected because UFWI recovers an equivalent continuous velocity model rather than exact object boundaries, and the result is influenced by finite wavelength, regularization (smoothing), limited-angle acquisition, and boundary-related scattering effects. Defects near the shaft perimeter tend to appear broadened or slightly smeared inward, and the soft-bottom response is expressed as a distributed low-velocity ring-like zone rather than discrete individual sandbag features.

Even with these limitations, Figure 4.27 demonstrates that UFWI provides a meaningful three-dimensional representation of the shaft condition. The inversion not only identifies the major defect levels but also preserves their relative vertical ordering and general spatial distribution. The results confirm that UFWI can detect and localize multiple embedded anomalies within a full-scale drilled shaft under realistic field conditions.

Figure 4.28 shows the boundary of the shaft, which is based on contour lines of 3,200 m/s of 2D slices at depths along the shaft length. It is noted that CSL data were analyzed at 2 cm depth intervals, the boundary contours are plotted at 10 cm depth intervals to improve visibility and avoid overcrowding of the displayed contours. The figure clearly shows boundary irregularities associated with the soil-inclusion defect at approximately 6 m depth, the aggregate-rich defect at approximately 9 m depth, and the soft-bottom condition near the shaft base. This information of the as-built boundary is crucial to determining the cover thickness of rebars. The cover thickness at the defects (6 m, 9 m, and bottom) is not sufficient and will adversely affect the long-term durability of the shaft due to corrosion.

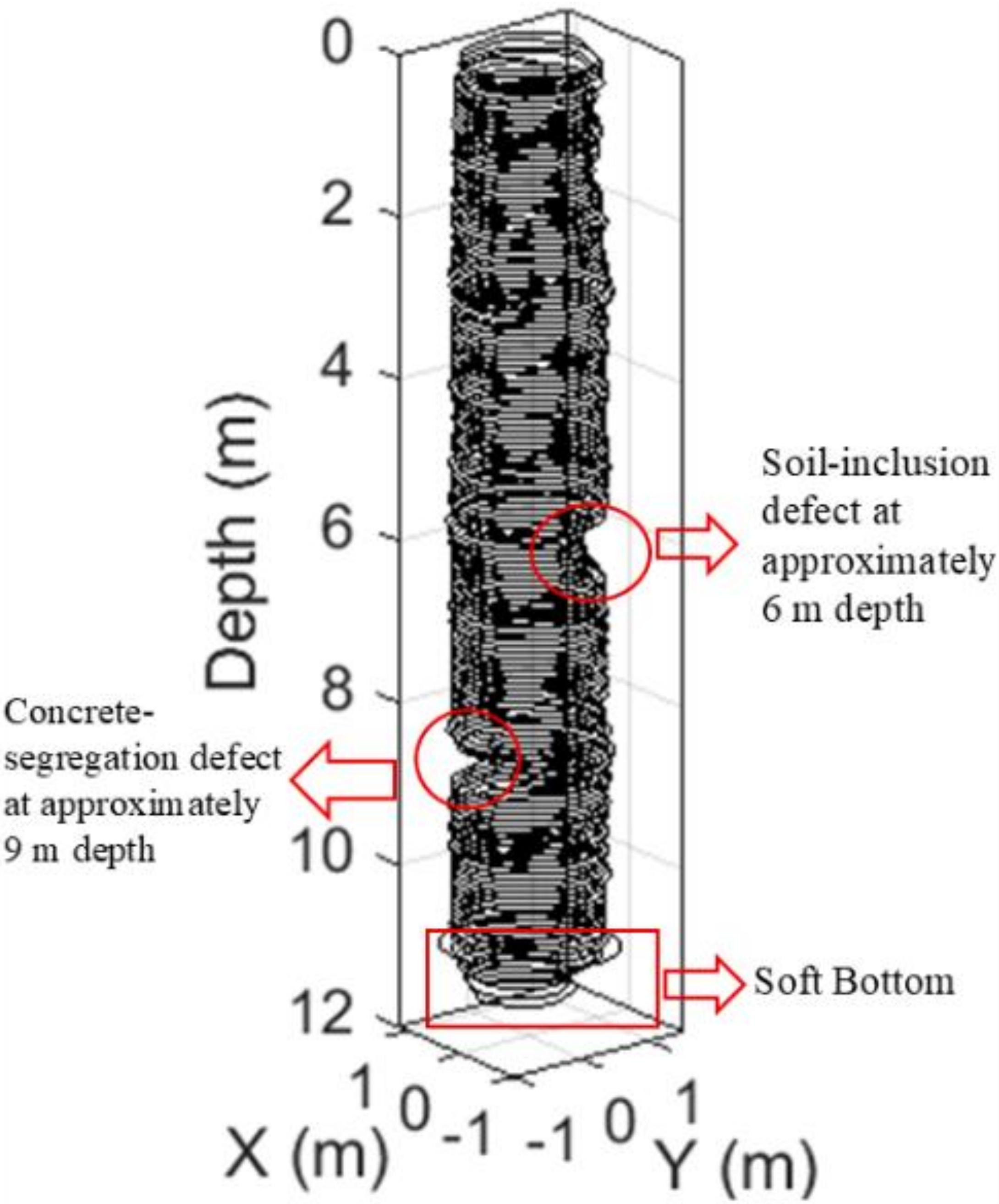

Figure 4.28 Inverted shaft boundary based on contour lines of 3,200 m/s of 2D slices at depths along the shaft length. For visual clarity, the contours shown in this figure are plotted at 10 cm depth intervals. It clearly shows the defects at 6 m (soil inclusion), 9 m (aggregate-rich), and soft bottom.

4.6.7Comparison of UFWI results with standard CSL velocity curves

To further evaluate the advantages of the developed UFWI method, the UFWI results were compared with the standard CSL results as velocity-depth curves. Standard CSL interpretation is commonly based on tube-pair measurements, including first-arrival time, apparent wave velocity, or signal energy. The Vp velocity is computed as the distance of a tube pair divided by the arrival time (determined from first-arrival signals).

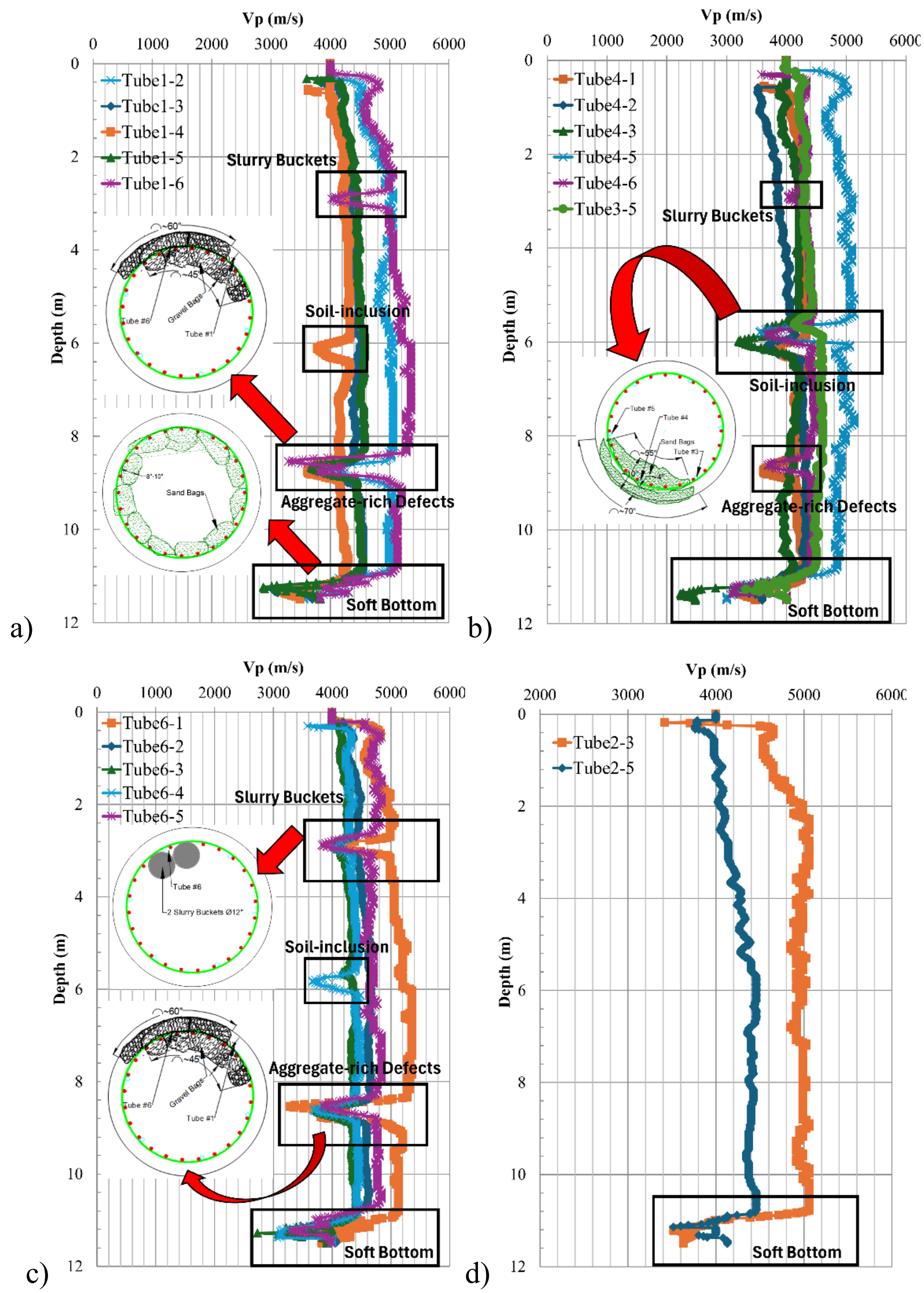

Figure 4.29 The standard CSL results as velocity-depth curves: (a) source at Tube #1; (b) source at Tube #4 and Tube Pair 3-5; (c) source at Tube #6; (d) Tube Pair 2-3, 2-5.

As shown in Figure 4.29, the standard CSL velocity curves identify several anomalous depth intervals that are consistent with the intentionally embedded defects. In Figure 4.29(a), several tube pairs associated with Tube #1 show abnormal velocity responses near the depths of the slurry-bucket defect, the soil-inclusion defect, the aggregate-rich defect, and the soft-bottom condition. In Figure 4.29(b), tube pairs associated with tube #4 and tube pair 3-5 show a pronounced velocity reduction near the soil-inclusion defect depth, which is expected because the L2 necking/soil-inclusion defect was installed near tubes #3 to #5. In Figure 4.29(c), tube pairs associated with tube #6 show clear responses near the slurry-bucket and aggregate-rich defect depths, which are consistent with the as-built locations of these defects near Tube #6. In contrast, Figure 4.29(d) shows tube pairs 2-3 and 2-5, which do not directly cross the major upper defect zones. These curves remain relatively stable through most of the shaft length and mainly show an abnormal response near the soft-bottom region. This comparison confirms that standard CSL velocity curves can detect the defects when the affected zone intersects or strongly influences a measured tube-pair path.

However, the standard CSL curves provide only one-dimensional apparent velocity information along individual tube pairs. A reduction in apparent velocity indicates that a possible anomaly exists somewhere along the wave path between two access tubes, but it does not directly determine the defect geometry. Therefore, standard CSL cannot define the defect size, cross-sectional shape, boundary, or severity. The magnitude of the velocity reduction alone cannot be directly converted into defect volume or defect thickness because the measured value is affected by path averaging, tube spacing, wave scattering, signal attenuation, source-receiver coupling, and the position of the defect relative to the tube-pair path. No information on the shaft boundary and defects outside rebar is obtained by standard CSL.

Another limitation of standard CSL is that the azimuthal location of a defect is not uniquely determined. When an anomaly appears in one tube-pair curve, the defect may be located anywhere along or near that tube-pair path. When multiple tube pairs show abnormal responses at similar depths, the approximate affected region can be inferred qualitatively, but the actual azimuthal position and lateral extent still require interpretation. For example, the soil-inclusion defect produces strong responses in tube pairs involving Tubes #3 to #5, while the slurry and aggregate-rich defects are more evident in tube pairs involving Tube #6 and Tube #1. These observations are consistent with the as-built defect locations, but the CSL curves alone do not provide a direct cross-sectional image showing where the defects are located relative to the shaft boundary and reinforcement cage.

Compared with standard CSL, UFWI provides substantially more spatial information. Instead of interpreting each tube-pair curve independently, UFWI uses the full waveform data from all available tube pairs to reconstruct a two-dimensional P-wave velocity distribution at each depth. The reconstructed velocity images show not only the presence of low-velocity anomalies but also their approximate azimuthal locations, lateral extents, and relationships to the shaft boundary and CSL tube layout. For the full-scale test shaft, UFWI identified the major defect horizons indicated by the standard CSL velocity curves and further localized the anomalies in the correct cross-sectional sectors: the L1 aggregate-rich defect near Tubes #6 and #1, the L2 necking/soil-inclusion defect near Tubes #3 to #5, the L3 slurry-inclusion defect near Tube #6, and the soft-bottom anomaly near the shaft base.

In summary, standard CSL is effective as a screening tool for identifying suspicious depth intervals and tube pairs affected by possible defects (internal defects only). However, it does not provide information on size or precise azimuthal location of defects. The main limitation of the standard CSL is that it provides no information on shaft boundary and defects outside rebar. The UFWI extends the value of CSL testing by converting the measured waveform data into cross-sectional velocity images, allowing direct visualization of the shaft boundary and defect distribution. Therefore, UFWI provides a significant improvement over conventional CSL interpretation for drilled shaft integrity assessment, especially when the objective is to evaluate defect geometry, boundary condition, and potential cover-thickness variation.

4.7 Thermal profiling of constructed drilled shaft

Thermal profiling (TP) was also performed on the drilled shaft to provide an independent assessment of concrete quality and to compare the thermal response with the known embedded anomalies. The TP data were collected continuously for 7 days right after the drilled shaft was constructed, when the concrete was still undergoing active cement hydration and the internal temperature field was well developed. TP evaluates shaft integrity by measuring the heat generated during cement hydration. In general, zones with reduced concrete volume, soil intrusion, slurry contamination, poor concrete quality, or foreign inclusions tend to produce lower temperatures than the expected background trend, whereas zones with greater concrete volume or locally higher cement content may produce higher temperatures. Therefore, deviations of the measured temperature profile from the expected temperature trend can be used to identify potential anomalies along the shaft depth.

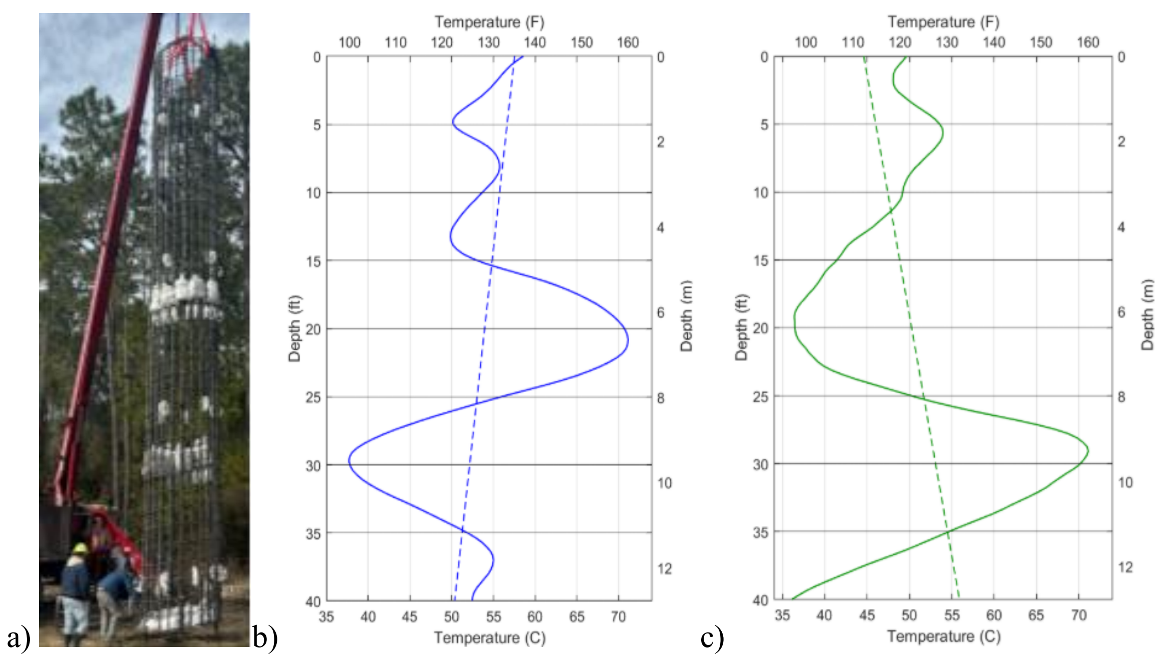

Figure 4.30 Thermal profiles (TP) from 6-ft diameter shaft with known anomalies: (a) field photograph of cage; (b) TP data near tube 6 (gravel bags at 30 ft depth, slurry at 10 ft depth); (c) TP data near tube 4 (soil bags at 20 ft depth). There is no indication of temperature drop at slurry buckets.

Figure 4.30(a) shows the reinforcement cage before concrete placement. Four anomaly materials were attached to the cage at different depths and circumferential locations, including gravel bags, soil bags, slurry buckets, and soft-bottom material. These known anomaly locations provide ground truth for evaluating the TP response.

Figure 4.30(b) presents the TP profile measured near tube 6, where gravel bags were placed at 30 ft depth and slurry buckets were placed at 10 ft depth. The blue solid curve represents the measured temperature profile at the highest temperature (day 2), and the blue dashed line represents the general background temperature trend with depth. A clear negative temperature anomaly is observed near 30 ft, where the measured temperature drops significantly below the background trend. This low-temperature response is consistent with the known gravel-bag inclusion at this depth. The gravel material locally reduces the amount of hydrating concrete around the thermal sensor and changes the local thermal properties, producing a cooler zone in the TP. This result indicates that TP successfully detected the gravel-related anomaly near tube 6. However, there is no indication of temperature drop at the slurry buckets at tube 6.

Figure 4.30(c) shows the TP profile measured near tube 4, where soil bags were placed around a depth of approximately 20 ft. A pronounced low-temperature anomaly is observed between approximately 15 and 23 ft, with the largest temperature reduction occurring near 20 ft. This cooling zone corresponds well with the known soil-bag location. The response is also broader than a single-point disturbance, suggesting that the soil inclusion affected a vertical interval around the designed anomaly elevation. Compared with the background temperature trend, the temperature reduction near 20 ft is substantial, indicating a clear local loss of sound concrete.

The soft-bottom condition can also be observed in the lower portion of the TP profiles. Near the shaft toe, the measured temperature decreases relative to the expected background trend, especially in the profile near tube 4. This lower-temperature response may be associated with loose soil, sediment, or poor-quality material remaining at the base of the excavation before concrete placement. Because the soft-bottom material replaces or contaminates sound concrete near the shaft base, it can reduce the local heat generated during cement hydration and produce a cooler thermal response. However, interpretation of soft-bottom defects using TP is more complicated than interpretation of mid-depth inclusions. The shaft toe is a boundary region, and the measured temperature can be influenced by end effects, heat transfer into the surrounding ground, limited sensor coverage below the defect, and the absence of measurements beneath the shaft base. Therefore, TP can indicate a possible abnormal thermal response near the bottom, but it is difficult to determine the exact thickness, lateral extent, or geometry of the soft-bottom zone from TP data alone.

Although the TP results can capture the defect zones associated with the L1 and L2 anomalies, several limitations are evident. First, the TP profiles did not clearly identify the defect located at the L3 level, where slurry buckets were embedded. This may be related to the circumferential distance between the thermal sensor and the defect, the reduced thermal contrast of the slurry-related anomaly, or the limited sensitivity of the one-dimensional temperature profile to localized defects away from the measurement tube. Second, the vertical resolution of the TP results is relatively low. The actual embedded defects were approximately 1 to 2 ft in size, but the corresponding TP anomalies appear as much broader temperature deviations over several feet. This broadening indicates that TP is more effective for identifying the approximate depth range of a thermal anomaly than for resolving the true defect thickness or geometry.

Overall, the TP results show reasonable agreement with several known anomaly locations. The profile near tube 6 identifies the gravel-bag anomaly around 30 ft, while the profile near tube 4 identifies the soil-bag anomaly around 20 ft. The lower-temperature response near the shaft toe also suggests that TP may provide useful evidence of the soft-bottom condition. However, the inability to clearly detect the L3 slurry-bucket defect and the broadened temperature responses demonstrate that TP has limited resolution for small, localized, or circumferentially distant defects. Future TP testing could benefit from a smaller recording interval, denser spatial sampling, and higher-resolution fiber-optic temperature sensing to improve defect localization and vertical resolution. In this study, TP serves as a useful complementary method to UFWI by independently confirming some known anomaly depths and identifying possible bottom-quality issues, but it does not directly provide a high-resolution cross-sectional image of defect geometry. Therefore, TP is best used together with imaging-based methods such as UFWI for more complete drilled-shaft integrity assessment.

Chapter 5 - SUMMARY

5.1 General

This study developed, optimized, and field-validated a two-dimensional UFWI framework for drilled shaft imaging using CSL waveform data. The work was motivated by the limitations of conventional CSL interpretation, which provides useful one-dimensional tube-pair information but does not directly produce high-resolution cross-sectional images of shaft geometry, boundary conditions, or construction defects. The proposed approach uses the full recorded ultrasonic waveform, including arrival time, phase, amplitude, and early scattered-wave information, to reconstruct the P-wave velocity distribution of the shaft at each testing depth.

The project was completed through three major tasks. First, a 2D ultrasonic FWI algorithm was developed and evaluated using controlled numerical models of drilled shafts with no defect, internal defects, and external boundary defects. Second, parametric studies were conducted to optimize CSL testing configurations for different shaft diameters and defect types. Third, the method was applied to a full-scale field test shaft constructed at the FDOT Hawthorne test pit with intentionally embedded anomalies, including concrete segregation/aggregate-rich material, necking/soil intrusion, slurry inclusion, and a simulated soft-bottom condition.

Overall, the results demonstrate that the 2D UFWI can accurately reconstruct the shaft boundary and identify low-velocity anomaly zones without requiring prior knowledge of the shaft boundary (design or constructed), concrete volume, or defect geometry. By inverting closely spaced depth slices and stacking the resulting velocity images, the method also provides a three-dimensional representation of drilled shaft condition. Thermal profiling provided useful complementary information on anomaly depths but showed lower spatial resolution and less ability to characterize cross-sectional defect geometry than the FWI-based images.

5.2 Development and testing of 2D UFWI algorithm

The computational algorithm developed in this study models CSL measurements as acoustic wave propagation because the recorded ultrasonic signals are dominated by pressure waves transmitted through water-filled access tubes and concrete. Forward modeling was implemented using a finite-difference solution of the acoustic wave equation with absorbing boundary treatment to reduce artificial reflections from the computational domain. The inversion was formulated as an iterative least-squares waveform-matching problem, and the adjoint-state method was used to calculate the gradient efficiently without explicitly forming the full sensitivity matrix.

To improve stability and image quality, the objective function combined waveform misfit with regularization terms. Tikhonov regularization was used to stabilize the inversion and suppress unrealistic oscillations, while a tube-pair velocity constraint incorporated first-arrival velocity information from conventional CSL interpretation. Approximate Hessian-based scaling was used to balance model sensitivity and reduce acquisition-geometry artifacts. Adaptive total variation denoising using the split Bregman method was also applied to reduce small-scale numerical artifacts while preserving sharp velocity contrasts associated with shaft boundaries and defect zones.

Synthetic validation demonstrated that the algorithm could recover the cross-sectional geometry of drilled shafts and detect representative defects. For the defect-free shaft, the inverted velocity image accurately reconstructed the shaft boundary from an initially homogeneous model. For the internal-defect model, the method recovered the low-velocity inclusion within the shaft and substantially reduced the normalized waveform misfit. For the external-defect model, the algorithm identified the boundary-related anomaly and reconstructed the distorted shaft perimeter. These results confirmed that the developed 2D UFWI algorithm can use standard CSL waveform data to image both internal defects and external boundary defects with accuracy.

5.3 Optimization of test configurations for 2D UFWI

The test-configuration investigation evaluated how the number of CSL access tubes affects the reliability of 2D UFWI for drilled shafts with different diameters. Synthetic models were created for 4-ft, 6-ft, and 8-ft diameter shafts with both internal and external defects. For each shaft diameter and defect type, inversion results were compared for tube configurations ranging from four to eight access tubes. The comparison focused on whether the inversion could recover the shaft boundary, detect the defect, and reasonably preserve the defect location and geometry.

The results show that angular coverage is the controlling factor for reliable FWI-based imaging. Configurations with seven or eight tubes generally provided the most accurate boundary and defect reconstructions. Six-tube configurations were effective for 6-ft shafts and remained acceptable for larger shafts, although some defect smoothing and loss of detail were observed. Five-tube configurations generally represented the minimum practical condition for detecting both internal and external defects, but the recovered defect size and shape were less reliable than those obtained with denser tube layouts. Four-tube configurations were not sufficient for reliable imaging; the inversion commonly produced overly smoothed boundaries and failed to resolve localized defects, especially for external necking-type anomalies.

Based on these parametric studies, at least five access tubes are recommended for 2D ultrasonic FWI of drilled shafts. For shafts with diameters of 6 ft or larger, one access tube per foot of shaft diameter is recommended when practical, consistent with conventional CSL practice and beneficial for inversion coverage. Additional tubes improve angular illumination, reduce artifacts, and provide more reliable characterization of defect geometry, particularly for boundary defects located near or outside the reinforcement cage.

5.4 Verification of 2D UFWI algorithm on defective shaft

The field validation was conducted using a full-scale drilled shaft constructed at the FDOT Hawthorne test pit. The shaft had a nominal diameter of 6 ft and a length of 40 ft, with six CSL access tubes installed around the reinforcement cage. Intentional anomalies were installed at different depths and azimuths to provide known reference conditions for method evaluation. These included an aggregate-rich/concrete-segregation zone near Tubes #6 and #1, a necking/soil-inclusion defect near Tubes #3 to #5, slurry buckets near Tube #6, and sandbags near the base to simulate a soft-bottom condition.

Field CSL measurements were acquired on the third day after concrete placement at 2-cm depth intervals, producing 576 depth levels over an effective testing length of approximately 11.5 m. Before inversion, the data were preprocessed using band-pass filtering, relative-energy screening, and time windowing. The retained frequency content was mainly in the 10-30 kHz range, which provided a practical balance between spatial resolution, numerical stability, and computational cost. Poor-quality low-energy traces were excluded when sufficient tube-pair coverage remained, while slices that would otherwise lose all measurements were retained to avoid empty inversion datasets.

The field inversion results show that the 2D ultrasonic FWI workflow successfully reconstructed the drilled shaft boundary and identified the major embedded anomaly horizons. At non-defective elevations, the method produced a clear velocity contrast between sound concrete and surrounding soil, allowing the shaft boundary and cover-thickness variations to be evaluated. At the L1 level, the aggregate-rich/segregation defect was detected as a subtle, broadened velocity disturbance in the correct sector between Tubes #6 and #1. At the L2 level, the necking/soil-inclusion defect was recovered as a clear low-velocity zone near the designed lower-left boundary sector. At the L3 level, the slurry-related anomaly was detected near Tube #6, although the recovered feature was smoother and broader than the physical bucket geometry. Near the shaft base, distributed low-velocity regions were recovered around the perimeter, consistent with the simulated soft-bottom condition.

The stacked three-dimensional FWI results provided a useful volumetric representation of the shaft condition. The recovered low-velocity anomaly zones were located at depths consistent with the documented as-built defect levels, and the boundary contours showed irregularities associated with the known defect regions and bottom condition. The recovered anomalies were smoother and more spatially diffused than the installed physical objects because the inversion produces an equivalent continuous velocity model and is influenced by finite wavelength, limited-angle acquisition, regularization, and boundary scattering. Nevertheless, the field results demonstrate that 2D ultrasonic FWI can detect, localize, and visualize representative drilled shaft defects under realistic construction and data-acquisition conditions.

Thermal profiling results provided complementary evidence for several anomaly locations. The temperature profiles identified the gravel-bag anomaly near 30 ft and the soil-bag anomaly near 20 ft, and they also suggested an abnormal response near the shaft toe. However, the slurry-bucket defect was not detected by thermal profiling, and the thermal anomalies were broader than the true embedded defect dimensions. These results indicate that thermal profiling is useful for identifying approximate anomaly depths but is less effective than ultrasonic FWI for resolving cross-sectional defect geometry. The combined findings support the use of 2D ultrasonic FWI as a promising high-resolution nondestructive imaging tool for drilled shaft integrity assessment, especially when used together with complementary methods such as CSL metrics and thermal profiling.

5.5 Conclusion and future work

The outcomes of this research demonstrate that UFWI represents a game-changing advancement in drilled shaft nondestructive evaluation. Unlike conventional methods that rely primarily on travel-time or energy-based indicators, UFWI utilizes the complete recorded wavefield to generate quantitative, high-resolution images of the shaft interior. This capability provides new opportunities for detecting and characterizing defects, evaluating shaft geometry, assessing concrete quality, and improving confidence in foundation construction quality. The ability to produce volumetric images of drilled shafts has the potential to fundamentally transform integrity assessment practices and support more informed engineering decisions regarding foundation acceptance, remediation, and long-term performance.

Future work will focus on transitioning technology from a research tool to a practical implementation platform for industry use. Efforts will include development of an automated software package that integrates data quality control, preprocessing, waveform inversion, three-dimensional visualization, and defect interpretation into a streamlined workflow suitable for routine engineering practice. Additional research will focus on improving computational efficiency, incorporating advanced inversion strategies and machine-learning-assisted interpretation, and validating the methodology on a broader range of shaft sizes, defect types, and field conditions. These developments will facilitate deployment of UFWI for production drilled shafts and support its adoption as a next-generation technology for drilled shaft quality assurance and integrity assessment.

REFERENCES

Aki, K., & Richards, P. G. (2002). Quantitative Seismology (2nd ed.). University Science Books.

By, P., Popovics, J. S., Roesler, J. R., Bittner, J., Amirkhanian, A. N., Brand, A. S., Gupta, P., & Flowers, K. (2017). Ultrasonic Imaging for Concrete Infrastructure Condition Assessment and Quality Assurance. In CIVIL ENGINEERING STUDIES Illinois Center for Transportation Series.

Camp Iii, W. M., Holley, D. W., & Canivan, G. J. (2007). Crosshole sonic logging of South Carolina drilled shafts: A five year summary. Geo-Denver 2007: Contemporary Issues In Deep Foundations, 1–11. https://doi.org/10.1061/40902(221)2

Hong, W.-T., Seung, ;, Shin, Y., Park, M.-C., Lee, J.-S., Asce, M., & Song, M. J. (2019). Load Transfer Curve Analyses of Drilled Shafts Using Crosshole Sonic Logging Test. Journal of Geotechnical and Geoenvironmental Engineering, 145(7), 1–14. https://doi.org/https://doi.org/10.1061/(ASCE)GT.1943-5606.0002068

Iskander, M., Roy, D., Kelley, S., & Ealy, C. (2003). Drilled shaft defects: detection, and effects on capacity in varved clay. Journal of Geotechnical and Geoenvironmental Engineering, 129(12), 1128–1137. https://doi.org/10.1061/ASCE1090-02412003129:121128

Komatitsch, D., & Martin, R. (2007). An unsplit convolutional perfectly matched layer improved at grazing incidence for the seismic wave equation. Geophysics, 72(5), SM155–SM167. https://doi.org/10.1190/1.2757586

Kordjazi, A., Coe, J. T., & Afanasiev, M. (2021). Nondestructive Evaluation of Drilled Shaft Construction Anomalies Using Full Waveform Tomography of Simulated Crosshole Measurements. Journal of Nondestructive Evaluation, 40(3), 1–13. https://doi.org/10.1007/s10921-020-00728-8

Mullins, G. (2010). Thermal integrity profiling of drilled shafts. DFI JOURNAL, 4(2), 54–64.

Mullins, G., & Winters, D. (2011). Infrared thermal integrity testing quality assurance test method to detect drilled shaft defects. https://staging-dot.cdc.gov/view/dot/21514/dot_21514_DS1.pdf

Nocedal, J., & Wright, S. J. (2000). Numerical Optimization Second Edition (2nd ed.). Springer.

Petek, K., Felice, C. W., & Holtz, R. D. (2012). Capacity analysis of drilled shafts with defects. In O'Neill Michael & Townsend Frank (Eds.), Deep Foundations 2002: An International Perspective on Theory, Design, Construction, and Performance (pp. 1120–1135). 2002 American Society of Civil Engineers. https://doi.org/10.1061/9780784406014

Plessix, R. E. (2006). A review of the adjoint-state method for computing the gradient of a functional with geophysical applications. In Geophysical Journal International (Vol. 167, Number 2, pp. 495–503). https://doi.org/10.1111/j.1365-246X.2006.02978.x

Salgado, R. (2022). The Engineering of Foundations, Slopes and Retaining Structures; Second Edition (second). CRC Press. https://doi.org/https://doi.org/10.1201/b22079

Tarantola, A. (2005). Inverse Problem Theory. Society for Industrial and Applied Mathematics (SIAM).

Yang, B., & Tran, K. (2026). Drilled shaft imaging with 3D ultrasonic full waveform inversion of cross-hole sonic logging (CSL) data. Nondestructive Testing and Evaluation, 1–30. https://doi.org/10.1080/10589759.2026.2613150

Yang, B., Tran, K. T., Herrera, R., & Shishlova, K. (2025). Drilled shafts imaging with 2D ultrasonic waveform tomography. Journal of Nondestructive Evaluation, 44(3). https://doi.org/10.1007/s10921-025-01238-1

Yang, S., Qiao, W., & Che, X. (2019). Numerical simulation of acoustic fields in formation generated by linear phased array acoustic transmitters during logging while drilling. Journal of Petroleum Science and Engineering, 182, 1–10. https://doi.org/10.1016/j.petrol.2019.106184

Appendix A: DISCRETE LAPLACIAN IN 2D AND MATRIX-FREE IMPLEMENTATION

For a scalar function $v(x, y)$ defined on a domain in $\mathbb{R}^2$, the Laplacian is given by

$$\nabla^2 v(x,y) = \frac{\partial^2 v}{\partial x^2}(x,y) + \frac{\partial^2 v}{\partial y^2}(x,y) \tag{A - 1}$$

Consider a uniform grid with spacing h in x and y direction, let the grid points be indexed by integers (i, j) so that

$$x_i = x_0 + (i-1)h; \quad y_j = y_0 + (j-1)h. \tag{A - 2}$$

A second-order central finite difference approximation is used for the second derivatives. The discrete Laplacian becomes

$$(\nabla^2 v)_{i,j} \approx \frac{1}{h^2}\left[v_{i+1,j} + v_{i-1,j} + v_{i,j+1} + v_{i,j-1} - 4v_{i,j}\right], \tag{A - 3}$$

i.e., $c_{i,j} = -4$ and neighbors around point (i, j): $c_{\text{adja}(i,j)} = +1$, where $c_{i,j}$ is the coefficient for Laplacian Matrix at (i, j) and $c_{\text{adja}(i,j)}$ is the coefficient of the element adjacent to (i, j).

The finite differences must be modified at the boundaries because not all neighbors exist. To define a matrix-free Laplacian operator, the local center coefficient $C_{i,j}$ is defined as

$$C_{i,j} = \begin{cases} -4 & \text{if } (i,j) \text{ is an interior point,} \\ -3 & \text{if } (i,j) \text{ lies on the boundaries (missing one neighbor)} \\ -2 & \text{if } (i,j) \text{ is a corner point (missing three neighbors)} \end{cases} \tag{A - 4}$$

Then the discrete Laplacian at grid point (i, j) can be written as

$$Lv_{i,j} = C_{i,j}v_{i,j} + \sum_{(i',j')\in N(i,j)} v_{i',j'}, \tag{A - 5}$$

where the adjacent set $N(i, j)$ consists of the points $\{(i-1, j), (i+1, j), (i, j-1), (i, j+1)\}$. The index of each point (i, j) should be positive, otherwise, the corresponding point is excluded.

Equation (A - 5) represents a 2D element-wise Laplacian operator, distinct from the traditional Laplacian matrix, significantly reducing memory requirements.

When implementing Tikhonov regularization, the squared Laplacian operator is needed. Taking the element-wise square of the Laplacian matrix, equation (A - 5) can be easily extended to squared Laplacian as

$$L_{2D}^{2} v_{i,j} = \left(C_{i,j}\right)^{2} v_{i,j} + \sum_{(i',j')\in N(i,j)} v_{i',j'}. \qquad \text{(A - 6)}$$

Appendix B: GRADIENT OF THE PAIR-VELOCITY REGULARIZATION

At a fixed depth slice, let $v(p)$ denote the velocity at grid point $p = (i, j) \in \Omega$; let (k, l) denote each tube pair, i.e. k and l are integers and $0 < k, l \leq N_s$. For each pair (k, l) with an observed velocity $v_{k,l}^{\text{obs}}$, a predicted pairwise apparent velocity is defined as a weighted average of the current model along a straight cord connecting the tube centers:

$$\bar{v}_{k,l} = \frac{\langle W_{i',j'}(p'), v_{k,l}(p') \rangle}{S_{i',j'}}, \quad \text{(B - 1)}$$

where $\langle \cdot,\cdot \rangle$ denotes the discrete inner product, $W_{i',j'}(p')$ is a prescribed footprint weight (e.g., a thick-ray mask with optional distance-decay and/or along-ray); $p' = (i', j')$ represents the grid-cell index within the thick-ray region Ω', and

$$S_{i',j'} = \sum_{p' \in \Omega'} W_{i',j'}(p'). \quad \text{(B - 2)}$$

The tube-pair velocity constraint term $E_{pair}(\mathbf{v})$ is then defined as a weighted least-squares misfit:

$$E_{pair}(\mathbf{v}) = \frac{1}{2} \sum_{k=1, k \leq l}^{N_s} \left(r_{k,l} \right)^2 \quad \text{(B - 3)}$$

where the pair residual $r_{k,l}$ is given by $r_{k,l} = \bar{v}_{k,l} - v_{k,l}^{\text{obs}}$.

Since $v_{k,l}^{\text{obs}}$ is independent of the model, differentiating $E_{pair}(\mathbf{v})$ with respect to a single grid value $v(p)$ gives us,

$$g_{\text{pair}}^{\text{2D}}(\mathbf{v}) = \sum_{k=1, k \leq l}^{N_s} r_{k,l} \frac{\partial \bar{v}_{k,l}}{\partial v(p)} \quad \text{(B - 4)}$$

Because weights $W_{k,l}(p)$ (and thus the corresponding summation $S_{k,l}$) are independent of the model, substituting (B - 4) into (B - 1) yields the discrete gradient at grid point p:

$$g_{\text{pair}}^{\text{2D}}(\mathbf{v}) = \sum_{k=1,k\leq l}^{N_s} r_{k,l} \frac{W_{i',j'}(p')}{S_{i',j'}} \qquad \text{(B - 5)}$$

Here, $g_{\text{pair}}^{\text{2D}}(\mathbf{v})$, the gradient contribution from the pair-velocity regularization term, which is incorporated into the total gradient in Eq. (2-9).

Appendix C: TOTAL VARIATION DENOISING USING THE SPLIT BREGMAN METHOD

To suppress small-scale numerical artifacts in the reconstructed velocity model while preserving sharp interfaces, an adaptive total variation denoising scheme was applied to the preliminary inverted model v. The denoised model $\bar{v}$ is obtained by solving

$$\Gamma(v) = \min_{\bar{v}} \frac{1}{2} \|\bar{v} - v\|_2^2 + \sum_{i,j} \lambda_{i,j} \left[(D_x \bar{v})_{i,j}^2 + (D_y \bar{v})_{i,j}^2 \right]^{1/2} \qquad \text{(C - 1)}$$

where the parameter $\lambda_{i,j}$ is spatially variable controlling the strength of TV denoising; D_x and D_y are finite-difference operators in the horizontal and vertical directions, respectively. They are defined as:

$$(D_x \bar{v})_{i,j} = \bar{v}_{i,j+1} - \bar{v}_{i,j}, \qquad \text{(C - 2)}$$

$$(D_y \bar{v})_{i,j} = \bar{v}_{i+1,j} - \bar{v}_{i,j}. \qquad \text{(C - 3)}$$

The adaptive $\lambda_{i,j}$ is constructed from the normalized magnitude of the preliminary inverted model:

$$\lambda_{i,j} = \lambda_{\min} + (\lambda_{\max} - \lambda_{\min}) a_{i,j}^{\vartheta} \qquad \text{(C - 4)}$$

where $a_{i,j} = \min\left[\max\left(\frac{v_{i,j} - P_{\text{low}}(v)}{P_{\text{high}}(v) - P_{\text{low}}(v)}, 0\right), 1\right]$, and P_{low} and P_{high} are percentile bounds. In this study, the 5th and 95th percentiles were used, respectively. The minimum and maximum TV weights were set to $\lambda_{\min} = 10$ and $\lambda_{\max} = 20$ respectively. The exponent ϑ controls the nonlinear mapping between the normalized velocity magnitude and the TV weight. In this study, $\vartheta = 2$ was used.

Using the split-Bregman method, an auxiliary variable

$$\mathbf{d} = (d_x, d_y) \approx \nabla \bar{v} \qquad \text{(C - 5)}$$

is introduced, where $d_x = D_x\bar{v}$, $d_y = D_y\bar{v}$. Equation $(\mathrm{C}-1)$ is then solved iteratively as

$$\min_{\bar{v},\mathbf{d}} \frac{1}{2}\|\bar{v} - v\|_2^2 + \sum_{i,j} \lambda_{i,j} \left\|\mathbf{d}_{i,j}\right\|_2 + \frac{\mu}{2}\|\mathbf{d} - \nabla\bar{v} - \mathbf{b}\|_2^2, \quad \text{(C - 6)}$$

where μ is the penalty parameter and $\mathbf{b}$ is the Bregman variable, which acts as a scaled dual variable to enforce the constraint $\mathbf{d} = \nabla\bar{v}$.

For fixed $\mathbf{d}$ and $\mathbf{b}$, the update for $\bar{v}$ is obtained from

$$(I + \mu\nabla^T\nabla)\bar{v} = v + \mu\nabla^T(\mathbf{d} - \mathbf{b}) \quad \text{(C - 7)}$$

The auxiliary variable is updated using adaptive vector shrinkage:

$$\mathbf{d}_{i,j} = \max\left(\left\|\mathbf{q}_{i,j}\right\|_2 - \frac{\lambda_{i,j}}{\mu}, 0\right)\frac{\mathbf{q}_{i,j}}{\left\|\mathbf{q}_{i,j}\right\|_2} \quad \text{(C - 8)}$$

where $\mathbf{q}_{i,j} = \nabla\bar{v}_{i,j} + \mathbf{b}_{i,j}$.

Finally, the Bregman variable is updated as

$$\mathbf{b} \leftarrow \mathbf{b} + \nabla\bar{v} - \mathbf{d}. \quad \text{(C - 9)}$$

The iteration is stopped when

$$\frac{\|\bar{v}^{k+1} - \bar{v}^k\|_2}{\|\bar{v}^k\|_2} < 10^{-5}, \quad \text{(C - 10)}$$

or when the maximum number of iterations is reached. In this study, the maximum number of iterations was set to 400.

This adaptive TV procedure reduces oscillatory artifacts and isolates high-frequency noise in the preliminary inverted model while preserving sharp velocity discontinuities associated with shaft boundaries and internal defects.